Universidade de Aveiro Departamento de Engenharia Mecânica
2017

Inês Carlos Ramos Almeida Bola

Desenvolvimento e análise numérica termomecânica de um queimador atmosférico

Development and numerical thermomechanical analysis of an atmospheric burner

Universidade de Aveiro Departamento de Engenharia Mecânica
2017

Inês Carlos Ramos Almeida Bola

Desenvolvimento e análise numérica termomecânica de um queimador atmosférico

Development and numerical thermomechanical analysis of an atmospheric burner

Dissertação apresentada à Universidade de Aveiro para cumprimento dos requisitos necessários à obtenção do grau de Mestrado em Engenharia Mecânica, realizada sob orientação científica de António Gil D'Orey Andrade Campos, Professor Auxiliar do Departamento de Engenharia Mecânica da Universidade de Aveiro e de Jorge Manuel Moutinho Neves Moreira de Pinho, Engenheiro de Desenvolvimento da Bosch Termotecnologia, S.A.

O júri / The jury

Presidente / President	**Doutor Vítor António Ferreira da Costa** Professor Catedrático da Universidade de Aveiro
Vogais / Committee	**Doutor Victor Fernando Santos Neto** Professor Auxiliar Convidado da Universidade de Aveiro
	Doutor Jorge Manuel Moutinho Neves Moreira de Pinho Engenheiro de Desenvolvimento da Bosch Termotecnologia, S.A. (co-orientador)

Agradecimentos / Acknowledgements

Ao professor Gil, por todo o apoio e por toda a paciência demonstrada ao longo deste percurso. Um muito obrigada pela oportunidade e por toda a aprendizagem.
Ao Jorge Pinho, ao Nuno Oliveira e ao Pedro Guerreiro por me darem a oportunidade de participar ativamente na grande empresa que é a Bosch Termotecnologia e por todo o interesse demonstrado no trabalho.
À minha família e amigos pelo apoio incondicional.

Palavras-chave Esquentador atmosférico; Modelo numérico; Análise termomecânica; Fluência; Fadiga; Previsão do tempo de vida

Resumo Atualmente, a simulação numérica de processos tecnológicos tem cada vez mais importância e é cada vez mais utilizada permitindo não só reproduzir as condições de funcionamento de determinado processo como também possibilita a previsão de possíveis falhas nos materiais. Assim, surgiu o presente trabalho para dar resposta à necessidade de conseguir caracterizar comportamentos mecânicos como a fluência e a fadiga, presentes na superfície de alumínio de um queimador atmosférico, e o impacto que podem ter. Para tal, através do software de simulação numérica ANSYS, realizou-se uma análise termomecânica da respetiva superfície de queima. Em primeiro lugar, selecionou-se o modelo numérico de Norton e procedeu-se à identificação dos respetivos parâmetros com base em duas análises distintas: uma análise analítica, com base apenas em curvas experimentais e relações analíticas; e uma análise numérica, com recurso ao módulo de otimização do ANSYS, em que os parâmetros foram iterativamente definidos. Posteriormente, as condições fronteiras do problema foram definidas e foi realizado um estudo de convergência da malha a usar nas simulações. Deste modo, foram obtidos os perfis de temperatura, tensão e deformação ao longo da superfície de queima. Por fim, considerando os fenómenos de fadiga e de fluência, o tempo de vida da superfície do queimador foi estimado com base em métodos de previsão.

Keywords Tankless gas water heater; Numerical model; Thermomechanical analysis; Creep damage; Fatigue damage; Lifetime prediction

Abstract Nowadays, the numerical simulation of technological processes is increasingly important and used, allowing to reproduce the operation conditions of a given process and to predict possible failures in materials. Thereby, the present work emerged, to answer the need to characterize mechanical behaviors such as creep and fatigue that are present on the aluminum surface of an atmospheric burner and to understand the impact they can have. For this purpose, the FEA program ANSYS was used to perform a thermomechanical analysis of the respective surface. Firstly, the Norton's numerical model was selected, and the respective parameters were identified based on two different analyses: an analytical analysis, based only on experimental curves and analytical relationships; and a numerical analysis using the ANSYS optimization module, in which the parameters were iteratively defined. Then, the boundary conditions of the problem were defined, and a mesh sensitivity study was carried out. Therefore, the temperature, stress and strain profiles were obtained along the surface. Considering the fatigue and creep phenomena, the lifetime of the burner surface was estimated based on prediction methods.

Contents

List of Tables

List of Figures

Chapter 1

Introduction and State-of-the-Art Review

1.1 Introduction

Nowadays, water heating systems are present in every house making this market very appealing and competitive. The requirement for larger efficiency and sustainability of the equipment with lower costs is growing within the companies. Therefore, manufacturers are continuously searching for new production processes and materials.

The numerical modeling is a way for the analysis and efficiency increase of the systems since it allows the material's and mechanical parts' behavior simulation avoiding potential problems. It also allows to easily design iteratively the material properties and geometry that in practice would take a long time to be designed.

The present work focuses on the atmospheric gas tankless water heaters burner's surface and intends to analyze its thermomechanical transient behavior. As water heaters are continuously exposed to thermal cyclic loads, the main goal consists on predicting the lifetime of the component by first develop a numerical model capable of simulating and reproducing complex phenomena such as creep and thermal fatigue. Then, with these results, a parametric analysis of creep-fatigue interaction is made, getting the predicted life of the burner surface.

1.1.1 Reading guide

The document starts with the state-of-the-art review, where the theoretical foundations necessary for the work understanding are presented.

Then, in chapter 2, the numerical creep model is defined through a curve fitting procedure based on experimental creep data tests for aluminium 1100. This process consists of a first analytical approach. With these results, an optimization process is realized in ANSYS Workbench.

In chapter 3, a thermal and thermomechanical analysis on the burner surface is presented. A temperature profile of the surface is obtained, which is then used as thermal load on the thermomechanical analysis to calculate the stress and deformation along the surface.

In chapter 4, the results from the previous chapter are applied in the methods of creep and fatigue life prediction and the burner's surface lifetime is estimated.

Lastly, in chapter 5, an analysis of the results is made in the chapter of the discussion and the conclusions of the work are presented.

1.2 Tankless water heaters

Tankless water heater[1] is an equipment for instantaneous production of hot water, i.e. water is heated in a heat exchanger exposed to the flames resulting from the burning of a fossil fuel. The fuels used in this type of system can be propane, butane or natural gas, among other less common fuels. There are also electric water heaters, in which electrical resistances are used for the instantaneous heating of the water. Gas heaters are the most commonly used hot water equipment in Portugal.

Within this type of system, there are variants that are essentially distinguished by the extraction conditions of the fuel gases. The most common and cheapest type is the atmospheric or natural extraction water heater. For this case, the gas outlet ducts meet the standards. When it doesn't happen, ventilated water heaters should be used, where the existence of a fan ensures the correct exhausting of the gases. There are also air-tight water heaters, also suitable for locations with poor exhaust conditions and/or poor air intake conditions, where air must be drawn directly from the outside. These equipments have a sealed combustion chamber, not requiring the room air. These also incorporate a fan that forces the exhaust combustion gases, and the admission of new air is made from the exterior of the building through independent ducts. There are also condensing water heaters incorporating a condensation unit for the water vapor resulting from the combustion products, allowing the heat released in these gases to be used to preheat the incoming water. In this way, one can take advantage of energy that would be wasted, significantly increasing the overall efficiency of the system.

When the user opens the hot tap water, the water passage into the heater is detected automatically, activating the gas valve which, in turn, allows the passage of gas to the burner. Once in the burner, the gas is mixed with the atmospheric air and is burned in the combustion chamber, releasing energy that is transmitted to the water circulating in the heat exchanger. The water, thus heated, is directed through the piping to the open tap.

The main components of this system are the injectors, which make the admission of the fuel; the mixing tubes, responsible for mixing fuel and atmospheric air, providing a more homogeneous mixture; the ignition system, responsible for starting the combustion; the burner, where the flame lies; the combustion chamber where the combustion takes place; the heat exchanger, composed of finned tubes inside which circulates the water to be heated; and the chimney where the exhaust gases are evacuated. On a condensing heater, there is a condensation unit located before the chimney. Figure 1.1 shows an atmospheric water heater with its components identified.

[1] The Portuguese name for tankless water heaters is Esquentadores.

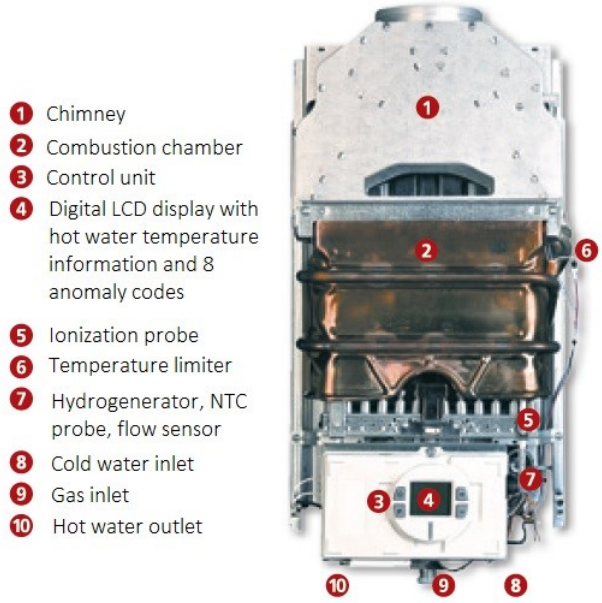

Figure 1.1: Example of an atmospheric gas water heater and its components. Adapted from [5].

The burner is one of the most important components of a water heater, since it's the component that mixes the fuel with air and conditions the gas/air mix flow for combustion. Its geometry and materials should be optimized so that the combustion is as homogeneous as possible, reducing gas consumption and polluting gas emissions.

The burner under consideration in this work is the BlueOcean OF Low NOx (figure A.1 and A.2 in Appendix A), developed by Bosch Termotecnologia, S.A. Optimized for low NOx emissions, this burner is water-cooled and full pre-mix, achieving high efficiency.

The gas manifold, made of two plates pressed against each other, is an airtight volume and is responsible for leading the gas to the injectors and ensure that sufficient air enters the burner. The gas manifold is connected to the mixing tubes by the bottom plate. The mixing tubes allows the mixing between the fuel gas and the room air, which is crucial to ensure a good combustion. Then, this mix goes thought the plenum chamber where it's velocity is homogenized. The burner surface is placed on top of the plenum chamber and consists of some blades held together by a pipe, where water circulates for cooling the blades surface (figure A.3). Consequently, the water is heated and then enters the heat exchanger's circuit, allowing for energy savings.

The burner operation mechanism consists of: (1) the gas enters the burner from the injectors at a defined flow rate, which then drags a certain amount of room air resulting in a first mix of these two fluids. (2) Then, the mix enters the mixing tubes where it becomes much more homogenous. (3) Then this is discharged into the plenum chamber, where it slows down achieving a homogenous velocity. (4) The final mix flows through the perforations of the burner surface, creating the combustion flames. (5) Finally, the

hot products of combustion rise through the heat exchanger where the domestic water is heated.

1.3 Existing phenomena in the atmospheric burner's surface

Since the atmospheric burner is constantly being switched on and off, its temperature is continually changing. Therefore, the burner undergoes cyclic thermal loads which can lead to structural and thermal problems. Its operation can go from a few minutes to several hours, being time a very important variable for the analysis of the burner's behaviour. Thus, phenomena such as creep and mechanical fatigue can occur.

1.3.1 Creep

Creep is a time and temperature dependent phenomenon that occurs at elevated temperatures usually exceeding 0,4 the melting temperature in case of metals [7]. It's the tendency of the metal to move slowly and deform plastically (permanently) under the influence of mechanical stresses. It can occur as a result of long-term exposure to high levels of stress that can still be below the yield strength of the material. A typical creep curve (strain-time) for metals under a constant load and temperature exhibits three characteristic stages, as represented in figure 1.2a [6].

Creep tests are carried out on a specimen loaded (in tension or compression), usually at constant load, inside a furnace which is maintained at a constant temperature (figure 1.2b). The extension of the specimen is measured as a function of time [14]. Another test, commonly used is the stress-rupture (or creep-rupture) test. This consists of an accelerated creep test that leads to rupture. It is usually carried out at a constant load, for the sake of simplicity. The important parameter obtained from the test is the time to rupture, whereas in the regular creep test, the minimum creep rate is the experimental parameter sought [6].

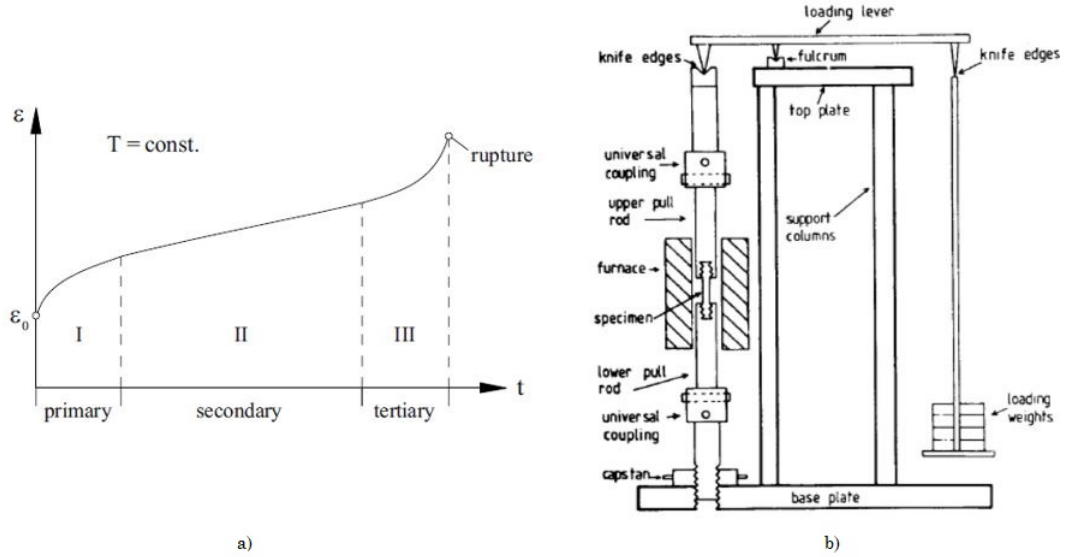

Figure 1.2: a) Typical strain-time creep curve; b) Creep test apparatus.

In primary or transient creep, following the instantaneous elastic strain η_0, the material deforms rapidly but at a decreasing rate. The duration of this stage is typically short in relation to the total creep curve [15]. In secondary- or steady-state-creep stage, the creep strain rate remains approximately constant over a long period of time and in tertiary creep, the strain rate accelerates quickly until the failure of the material.

The creep process is accompanied by many different slow microstructural rearrangements including dislocation movement, ageing of microstructure and grain-boundary cavitation [16].

The creep mechanism can be divided in two major groups: boundary mechanisms, in which grain boundaries and grain size play a major role, and lattice mechanisms, which occur independently of grain boundaries [6].

The origins of the inelastic deformation at the temperature range $0.5 < \mathrm{T/T_m} < 0.7$ are transport processes associated with motion and interaction of dislocations and diffusion of vacancies. Here one can consider two classes of physical models: dislocation and diffusion creep [16].

Diffusion Creep

Depending on the material, diffusion creep tends to occur for $\sigma/G \leq 10^{-4}$, where G is the shear modulus [6]. At higher temperatures ($\mathrm{T/T_m} > 0.7$) diffusion mechanisms control the creep rate. The deformation occurs at much lower stresses and results from diffusion of vacancies. The mechanism of grain boundary diffusion (Coble [17] creep) assumes diffusive transport of vacancies through and around the surfaces of grains. The deviatoric part of the stress tensor changes the chemical potential of atoms at the grain boundaries. Because of different orientations of grain boundaries, a potential gradient occurs. This gradient is the driving force for the grain boundary diffusion. The diffusion through the matrix (bulk diffusion) is the dominant creep mechanism (Nabarro-Herring [18] creep) for temperatures close to the melting point. These models (Coble and Nabarro-Herring) predict the diffusion controlled creep rate to be a linear function of the stress [16]. Nabarro and Herring proposed the mechanism shown schematically in figure 1.3a. It involves the flux of vacancies inside the grain. The vacancies move in such a way as to produce an increase in length of the grain along the direction of applied (tensile) stress. Hence, the vacancies move from the top and bottom region in the figure 1.3a to the lateral regions of the grain. The boundaries perpendicular (or close to perpendicular) to the loading direction are distended and are sources of vacancies. The boundaries close to parallel to the loading direction act as sinks. Nabarro and Herring developed a mathematical expression connecting the vacancy flux to the strain rate given by [6]:

$$\dot{\varepsilon}_{\mathrm{NH}} = A_{\mathrm{NH}} \frac{D_l G b}{kT} \left(\frac{b}{d}\right)^2 \left(\frac{\sigma}{G}\right), \tag{1.1}$$

where A_{NH} is typically equal to $10-15$, σ is the applied stress, D_{l} is the lattice diffusion coefficient, and d is the grain diameter.

Coble proposed the second mechanism explaining diffusion creep. It is based on diffusion in the grain boundaries instead of in the bulk. This diffusion results in sliding of the grain boundaries. Hence, if a fiducial scratch is made on the surface of the specimen prior to creep testing, the scratch will show a series of discontinuities (at the grain boundaries) after testing if Coble creep is observed. Figure 1.3b shows, in a schematic manner,

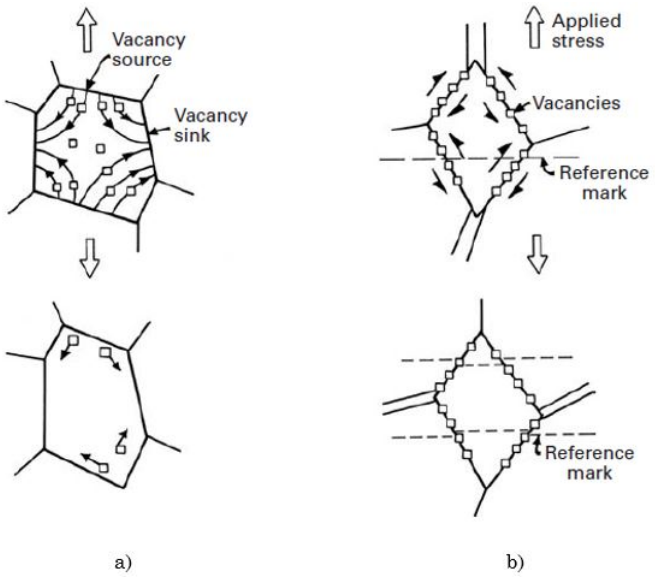

Figure 1.3: Flow vacancies according to a) Nabarro-Herring and b) Coble mechanisms, resulting in an increase in the length of the specimen [6].

how the flow of vacancies along a boundary generates shear. Notice that there is also additional accommodational diffusion necessary. Coble creep leads to the relationship:

$$\dot{\varepsilon}_C = A_C D_{\mathrm{GB}} \frac{Gb}{kT} \left(\frac{\delta}{b}\right) \left(\frac{b}{d}\right)^3 \left(\frac{\sigma}{G}\right), \tag{1.2}$$

where A_C is typically equal to $30 - 50$, δ is the effective width of the grain boundary for diffusion, and D_{GB} is the grain-boundary diffusion coefficient [6].

Harper and Dorn [19] observed another type of diffusional creep in aluminium. This occurred at high temperatures and low stresses, and the creep rates were over 1 000 times greater than those predicted by Nabarro-Herring. The two researchers concluded that creep occurred exclusively by dislocation climb. Harper-Dorn creep is governed by an equation of the form:

$$\dot{\varepsilon}_C = A_{\mathrm{HD}} D_l \frac{Gb}{kT} (\frac{\sigma}{G}), \tag{1.3}$$

where the parameter A_{HD} is typically equal to 10^{-11} [6].

Dislocation Creep

In the stress range $10^{-4} < \sigma/G < 10^{-2}$, creep tends to occur by dislocation glide aided by vacancy diffusion and this is called dislocation creep [6].

Various creep rate equations within the dislocation creep range are based on the Bailey-Orowan recovery hypothesis. The common result is the power-law creep [16]:

$$\dot{\varepsilon}_{eq}^{cr} \propto \left(\frac{\sigma_{eq}}{G}\right)^n \exp\left(-\frac{Q}{RT}\right). \tag{1.4}$$

The exponent n varies from 3 to 10 for metallic materials. At higher stresses above $10^{-3}G$ the power law breaks down and a transition from the climb-plus-glide to the glide mechanism is assumed where the following empirical equation can be applied

$$\dot{\varepsilon}_{eq}^{cr} \propto \left[\sinh\left(\alpha\frac{\sigma_{eq}}{G}\right)\right]^n \exp\left(-\frac{Q}{RT}\right), \tag{1.5}$$

where α is a material constant. If $\alpha\sigma_{eq}/G < 1$ then equation 1.5 reduces to 1.4.

Grain-Boundary Sliding

In addition to the dislocation and the diffusion creep, the grain boundary sliding is the important mechanism for poly-crystalline materials, but usually does not play an important role during primary or secondary creep. This mechanism occurs because the grain boundaries are weaker than the ordered crystalline structure of the grains. Furthermore, the formation of voids and micro-cracks on grain boundaries contributes to the sliding. The whole deformation rate depends on the grain size and the grain aspect ratio (ratio of the grain dimensions parallel and perpendicular to the tensile stress direction). Samples with a larger grain size usually exhibit a lower strain rate [16].

Deformation-Mechanism Maps

The various creep mechanisms have been summarized into charts called deformation mechanism maps. A map is a two-dimensional representation where values of the homologous temperature $T = T_m$ are plotted along the horizontal axis and values of the normalized stress σ/G are plotted along the vertical axis. Regions of predominance of the individual creep mechanisms are indicated in the chart in terms of the ranges of values of stress and temperature for which each individual mechanism dominates the creep process. The maps are useful since these allow at a glance obtaining a semi-qualitative picture of the prevailing creep conditions under given stress and temperature [6]. For a given combination of the stress and the temperature, the map provides the dominant creep mechanism and the strain rate. A typical deformation map is shown in figure 1.4.

Weertman-Ashby plots assume, for simplicity, that there are independent and distinguishable mechanisms by which a polycrystal can be deformed, but still retain its crystallinity [6]:

- Above the theoretical shear strength, plastic flow of the material can take place without dislocations, by simple glide of one atomic plane over another;
- Movement of dislocations by glide;
- Dislocation creep, including glide and climb, both being controlled by diffusion;
- Nabarro-Herring creep;
- Coble creep.

From the deformation-mechanism map, one can, in addition to determining the dominant mechanism for a certain combination of stress and temperature, find the resulting strain rate (creep rate). For this, the appropriate constitutive equations should be applied and the constant strain-rate contours plotted [6] as illustrated in figure 1.5.

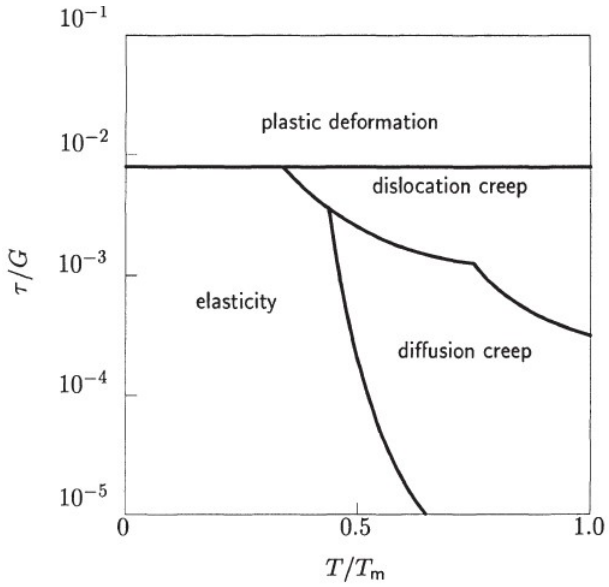

Figure 1.4: Typical deformation map: normalised stress vs. homologous temperature [7].

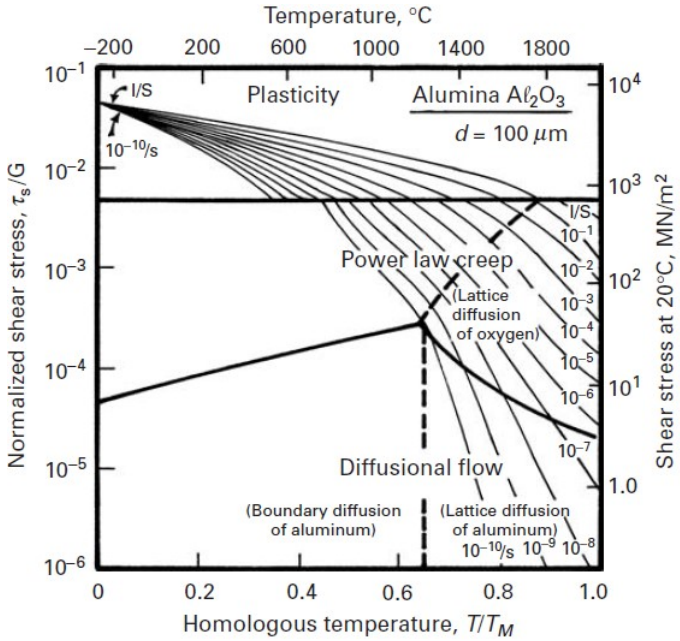

Figure 1.5: Weertman-Ashby map for Al_2O_3 with a grain size of 100 µm [6].

Difficulties in modelling creep

The analysis is more difficult as the time range increases at least for three reasons: as the time increases there are additional physical effects like diffusion, corrosion, and aging which are not usually taken into account in the mechanical constitutive equations; there is a time scale of some months or years above which there is almost no possibility to perform tests and ensure good identification of the material parameters; last but not least, the probability of the occurrence of unpredicted events increases with time.

Furthermore, the two extrema of the plastic strain rates where viscous effects even at room temperature should be taken into account:

- $\dot{\varepsilon}_P > 1 \sim 10^4$ s^{-1} is the range of rates occurring in shocks, crash, or loadings by accident. It is usually called dynamic plasticity because it happens at room temperature but it is formally labelled as visco-plasticity as the strain rate modifies the material response, especially if the reference identification has been performed at usual strain rates of about 10^{-4}s^{-1}. For example, the usual engineering yield stress may increase 10-50% at high strain rates of about 10^4s^{-1}.
- $\dot{\varepsilon}_P < 10^{-10}$ s^{-1} at the other extreme is the range which may exist in steels at room temperature loaded at small stresses, below the engineering yield stress. The resulting slow creep or relaxation may change the stress concentrations, induce leakage in pressurized vessels, or decrease the tension in the cables of pre-stressed concrete by relaxation of the steel cables associated with the creep of the concrete [20].

Uniaxial Creep Models

After the virtually instantaneous strain observed on loading (ε_0) represented in figure 1.2a, the time-dependent or creep strain (ε_{cr}) accumulates with time (t), so that the total strain (ε_c) at any instant is written as:

$$\varepsilon_c = \varepsilon_0 + \varepsilon_{cr}. \tag{1.6}$$

The ε_0 value is a function of stress (σ) and temperature (T),

$$\varepsilon_0 = f_1(\sigma, T), \tag{1.7}$$

whereas ε_{cr} varies not only with stress and temperature but also with time, as

$$\varepsilon_{cr} = f_2(\sigma, T, t). \tag{1.8}$$

No general agreement has been reached on the form of the equation that should be adopted to describe the accumulation of creep strain with time. Consequently, the creep curve shape is commonly discussed in terms of the changes in creep rate ($\dot{\varepsilon} = d\varepsilon/dt$) throughout a test. Thus, in differential form, the equation 1.8 becomes [21]:

$$\dot{\varepsilon}_{cr} = f_3(\sigma, T, \varepsilon). \tag{1.9}$$

Assuming the creep strain as a function of time with fixed stress and temperature, the following equations are proposed [7]:

$\varepsilon_{cr} = \beta t^{1/3} + kt$	Andrade, 1910,
$\varepsilon_{cr} = Ft^n$	Bailey, 1929,
$\varepsilon_{cr} = G\left(1 - e^{-qt}\right) + Ht$	McVetty, 1934,
$\varepsilon_{cr} = \varepsilon_1 + A\log t \ + Bt$	Leaderman, 1943,
$\varepsilon_{cr} = \varepsilon_1 + \varepsilon t^n \ \ (n < 1)$	Findley, 1944,
$\varepsilon_{cr} = \varepsilon_1 + A\log t$	Philips, 1956,
$\varepsilon_{cr} = \sum_i a_i t^{n_i}$	Graham and Walles, 1955.

For the creep strain rate-stress relation the following proposal exist:

$\dot{\varepsilon}_{cr} = K\sigma^m \quad (3 < m < 7)$	Norton, 1929, Bailey, 1929,
$\dot{\varepsilon}_{cr} = B(e^{\frac{\sigma}{\sigma^*}} - 1)$	Soderberg, 1936,
$\dot{\varepsilon}_{cr} = A\text{sinh}\,\frac{\sigma}{\sigma^*}$	Nadai, 1938, McVetty, 1943,
$\dot{\varepsilon}_{cr} = D_1\sigma^{m_1} + D_2\sigma^{m_2}$	Johnson et al. 1963,
$\dot{\varepsilon}_{cr} = A\big(\text{sinh}\,\frac{\sigma}{\sigma^*}\ \big)^m$	Garofalo, 1965,
$\dot{\varepsilon}_{cr} = \frac{d}{dt}\big(\frac{\sigma}{\sigma^*}\big)^{n_0} + \big(\frac{\sigma}{\sigma^*}\big)^n$	Odqvist, 1966.

The description of temperature dependencies is more complicated mainly due to influence of temperature on the material parameters and structural changes (the increase of the temperature yields different creep mechanisms) [7]. The junction of stress and temperature dependencies, different creep mechanisms can exist. Temperature-dependent creep equations can be expressed by

$\dot{\varepsilon}_{cr} \approx \exp\left(-\frac{Q-\gamma\sigma}{RT}\right)$	Kauzman, 1941,
$\varepsilon_{cr} = f\left[t\exp\left(-\frac{Q}{RT}\right)\ \right] f_1(\sigma)$	Dorn and Tietz, 1949,
$\dot{\varepsilon}_{cr} \approx \frac{\sigma}{T}\exp\left(-\frac{Q}{RT}\right)$	Lifshiz, 1963,
$\varepsilon_{cr} = f\left[t\exp\left(-\frac{Q}{RT}\right)\ \right]^n f_1(\sigma)$	Penny and Marriott, 1971,

where Q,R,n,γ denotes the activation energy, the ideal gas constant and material parameters, respectively [7].

For creep problems at constant stress the above expressions can be used as given. However, in practice one is often interested in solving creep problems in structural parts subjected to time varying stresses [15]. In those cases, the creep theories which include primary and secondary creep can be formulated by different approaches. The main approaches are [7]:

- The total strain theory,
- The time hardening theory,
- The strain hardening theory.

The total strain theory assumes the existence of a relationship between the total strain, the stress and time at fixed temperatures [7]. The time hardening theory, which is also called the flow theory, implies that creep rate is a function only of stress and current time, or

$$\dot{\varepsilon}_{cr} = f(\sigma, t). \tag{1.10}$$

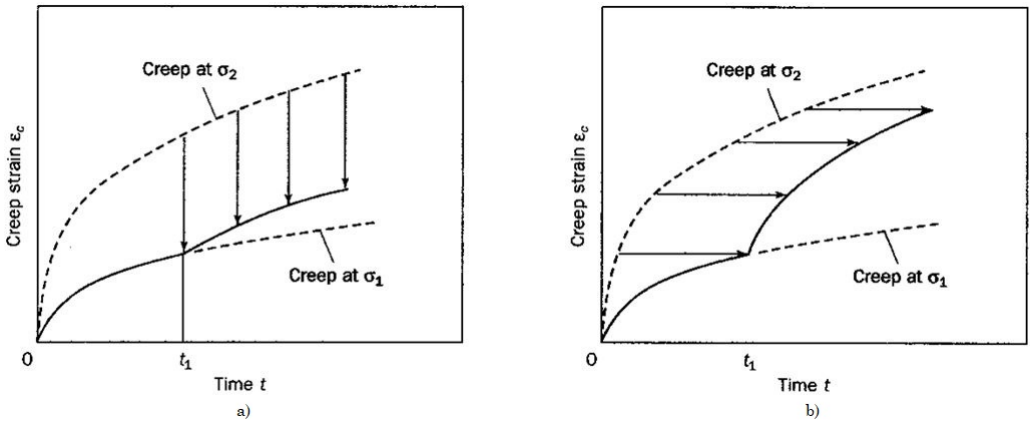

Figure 1.6: a) Time hardening; b) Strain hardening.

The creep curve after the change of stress from σ_1 to σ_2 has the same shape as the constant stress curve from the time change, i.e. the curve, σ_2, is moved vertically as shown in figure 1.6a. The strain hardening theory assumes that strain rate depends only on the stress and the current plastic strain, or

$$\dot{\varepsilon}_{cr} = g(\sigma, \varepsilon_{cr}). \tag{1.11}$$

But in this case σ_2, from the time of change, is moved horizontally, as shown in figure 1.6b [22].

The prediction of total creep strain after stress change are rather accurate in the case of the strain-hardening method both for step-up load change and step-down load change [22].

1.3.2 Fatigue

High temperature operation leads to thermal expansion which can be constrained in some regions. Therefore, mechanical stresses occur during start-stop-operation and the cyclic plastic deformation leads to the thermo-mechanical fatigue of the material [23]. Thermal fatigue involves cyclic loading under thermal stresses. Such thermal stresses occur when a temperature change occurs, which leads to differential expansion in two components that are joined together [6].

1.4 Creep-Fatigue interaction

There are many applications where materials are required to operate for long periods in harsh engineering environments of high stresses and temperatures. Examples of this can be found on the power generation industry and the gas turbine sector where components are experiencing higher temperature environments as designers seek to increase thermal efficiency [24]. This leads to a dependence on creep-fatigue life prediction methods to estimate the components design life.

The behaviour of creep, fatigue and creep-fatigue interaction are becoming more and more critical in life assessment, design and maintenance of components that are exposed to high temperature and cyclic loads. Thus, there's a need to use life prediction

methods in which both failure mechanisms and their interaction may be considered. In these approaches, fatigue damage per cycle and creep damage per cycle are separately calculated to predict creep-fatigue endurance.

A cumulative damage fraction (including creep and fatigue damages) of a critical value indicates the failure of materials based on a certain failure criterion. Generally, the failure of materials is assumed to occur when the summation of accumulated fatigue and creep damage reaches a critical value that is set to be unity [25].

There are many theories for creep-fatigue life prediction that can be found in the bibliography [26].

A widespread rule for creep-fatigue life analysis is the generalized linear damage summation (LDS) rule [7], [6], [14], [15], [16].

$$D_{total} = D_c + D_f, \tag{1.12}$$

where D_f is the fatigue damage without the creep action, D_c is the creep damage and D_{total} is the total damage, that is, the sum of fatigue damage and creep damage [27]. The LDS usually combines Miner's rule for fatigue damage and Robinson's Life Fraction rule for creep damage [28]. The total damage is the linear sum of the fatigue damage independent on time and the creep damage dependent on time [29], becoming:

$$D_{total} = \sum \frac{t_i}{t_f} + \sum \frac{n}{N_f} \tag{1.13}$$

where for the creep damage, t_i is the time spent under condition i,t_{f_i} is the time to failure under condition i and for the fatigue damage fraction, n represents the number of operating cycles and N_f de number of cycles to failure, under certain conditions. This method is usually represented in a diagram of creep versus fatigue damage fraction by a straight line connecting the coordinates (1,0) and (0,1). The shaded part in figure 1.7 can be considered as the safe design region.

Knowing the operating conditions, the values of t_i and n can be directly obtained. But for the calculation of time to failure t_{f_i} and the number of cycles to failure N_f, extrapolation or interpolation methods based on experimental data from creep rupture tests and fatigue tests should be considered. These approaches will be discussed hereinafter.

1.4.1 Creep life prediction

To estimate the creep life of a component, creep tests until rupture, at a stress level, could be used. But component life assessment based on data collected from creep curve and experimental creep laws do not always provide accurate life estimation. Although experiments can provide accurate life estimation, data are often insufficient to cover different loads and temperatures and extrapolation or interpolation to the stresses and temperatures of interest need to be performed [30]. Alternatively, there are methods based on time and temperature. Each of these approaches is a technique where short-term creep-rupture data can be extrapolated to longer-term scenarios using a time-temperature parameter. This concept assumes that all creep-rupture data for a given material can be combined to produce a single master curve where stress is plotted against a parameter that combines the effect of time and temperature [24]. Many parametric techniques have been proposed in the literature. The most widely used are the Larson-Miller parameter (LMP), Manson-Haferd parameter (MHP) and the Dorn-Sherby parameter (DSP). The

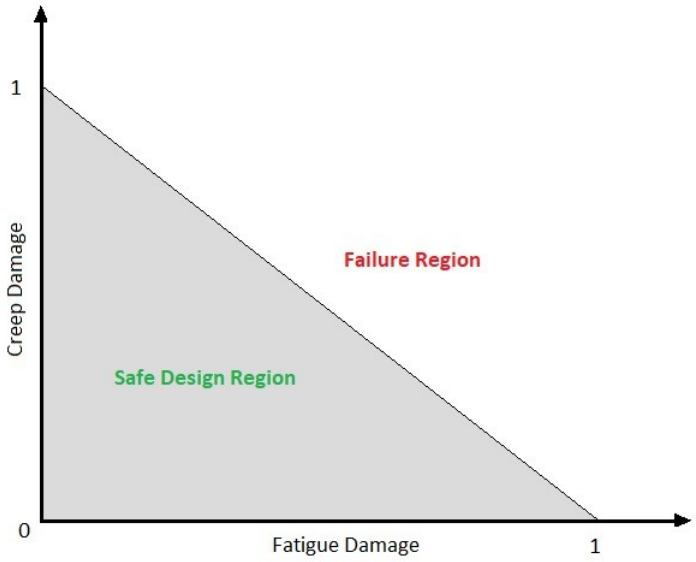

Figure 1.7: Failure criteria assumed in creep-fatigue life prediction. Adapted from [8] and [9].

benefit of these empirical models is that the creep rupture times, that are impractical to measure in the laboratory due to long testing times, can be estimated using short-term creep life data [31].

Parametric Methods

In 1963, Manson and Haferd [32] showed that all the three relationships mentioned before derive from:

$$P = \frac{(\log t)\sigma^Q - \log t_A}{(T - T_A)^R}, \tag{1.14}$$

where P is a parameter combining the effects of time, temperature, and stress; σ is the stress; T is the absolute temperature; and T_A, $\log t_A$, Q, and R are material constants.

Larson-Miller Parameter:

For the LMP, Larson and Miller [33] chosen the following values in equation 1.14:

$$\begin{gathered} \text{Q=0; R=-1.0;} \\ \text{T}_\text{A}\text{=-460°F or 0°F;} \\ t_\text{A}\text{= the constant C in the LMP.} \end{gathered}$$

Therefore, for the LMP the equation 1.14 reduces to:

$$\text{LMP} = \text{T}(\log t + \text{C}). \tag{1.15}$$

The constant C is the only unknown in this approach. It can be calculated through isostress data (same stress but different time-temperature exposure) plotted as reciprocal of T versus $\log t$. The straight lines observed should intersect at a point where 1/T=0 and $\log t$= the value of the unknown C [3].

Manson-Haferd Parameter:

For the MHP, Manson and Haferd [32], [34] chosen the following values for the constants in equation 1.14:

$$\text{Q=0; R=1.0.}$$

The general equation reduces to:

$$P = \frac{\log t - \log t_A}{T - T_A}. \tag{1.16}$$

In this case, there are two constants to be calculated, $\log t_A$ and T_A, which represents the coordinates of the convergence point of isostress data [3].

Dorn-Sherby Parameter:

Dorn and Sherby [35] developed their relationship as:

$$\text{DSP} = t \exp -\frac{A}{T}, \tag{1.17}$$

where t is time, A is a constant based on activation energy and T is the temperature (K).

Like the other approaches, the isostress data should be plotted but, in this case, the straight lines are parallel [3], where the slope corresponds to the A value.

Parameter Selection

The three relationships presented before, can be schematized in a plot of $\log t$ versus reciprocal T, for each case, as represented in figure 1.8.

For accurate life prediction, a critical decision lies on the selection of the most appropriate parameter for the assessment [7]. The LMP is the most widely used relationship, mainly for being a one-parameter model and its appliance can be seen in [36], [37].

1.4.2 Fatigue life prediction

Components of machines and structures are frequently subjected to cyclic loads, and the resulting cyclic stress can lead to microscopic physical damage to the materials involved. Even at stresses well below a given material's ultimate strength, this microscopic damage can accumulate with continued cycling until it develops into a crack or other macroscopic damage that leads to failure of the component. This process of damage and failure due to cyclic loading is called fatigue [10].

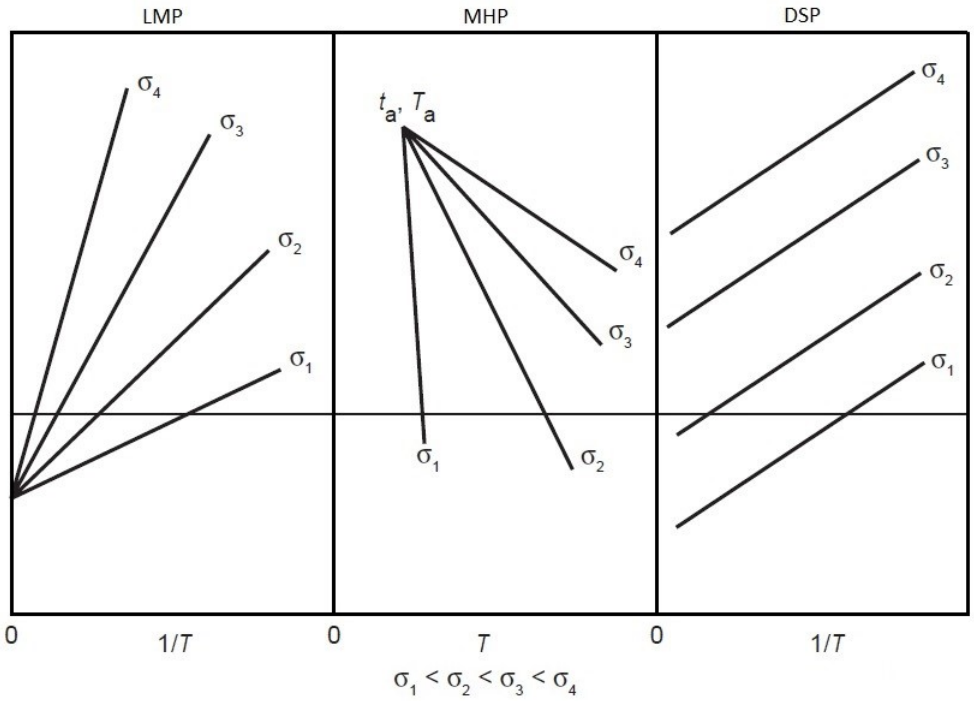

Figure 1.8: Representation of isostress data plotted for each parameter relationship. Adapted from [3].

August Wöhler, starting in the 1850s, began the development of design strategies for avoiding fatigue failure and also demonstrated that fatigue was affected not only by cyclic stresses but also by the accompanying steady (mean) stresses [10].

Fatigue failures is a major concern in engineering design, making the life prediction methods such an important subject to have in account in projects design.

At present, there are three major approaches to analysing and designing against fatigue failures: the stress-based approach, which is based on the analysis of the average stresses in the region of the component being analysed; the strain-based approach to fatigue considers the plastic deformation that may occur in localized regions where fatigue cracks begin and at stress raisers during cyclic loading; and the fracture mechanics approach which treats growing cracks using the methods of fracture mechanics [10].

The strain-based approach is applied in nuclear reactors and jet engines, specifically cyclic loading associated with their operating cycles, especially cyclic thermal stresses. For this reason, the strain approach is chosen for the present work.

Strain-based approach

A strain versus life curve is a plot of strain amplitude versus cycles to failure. Such a curve is employed in the strain-based approach for fatigue life estimations. This curve is obtained through a completely reversed cycling tests (equation 1.27 with R=-1) between constant strain limits. In this test, the specimen undergoes a set of cycles until it fails by fatigue, where the strain is kept between the desired maximum and minimum values, which in this case are symmetrical ($\varepsilon_{\min} = -\varepsilon_{\max}$). Thus, the results for several different

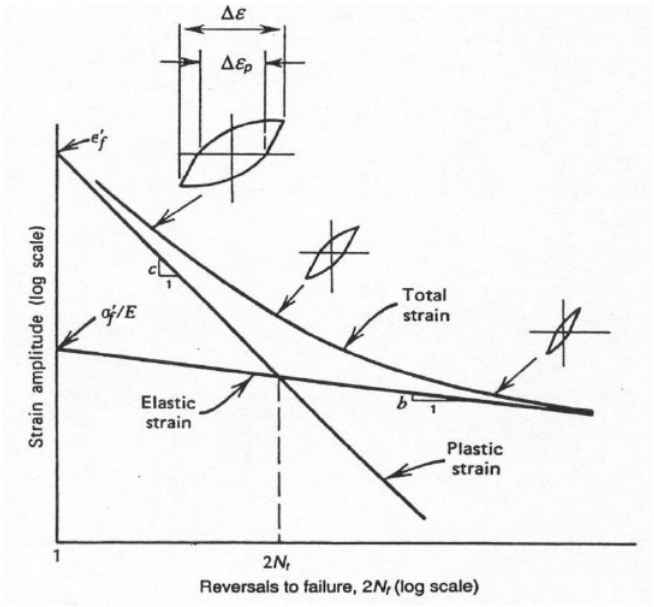

Figure 1.9: Elastic, plastic and total strain vs life curves [10].

strain amplitudes (ε_a) gives the desired curve which can in turn be used to estimate the number of cycles to failure, knowing the material's strain amplitude. A schematic diagram is given in figure 1.9. A log-log plot is usually used for strain-life curves [10].

The strain amplitude can be divided into elastic and plastic parts:

$$\varepsilon_a = \varepsilon_{ea} + \varepsilon_{pa}, \tag{1.18}$$

where the elastic strain amplitude is related to the stress amplitude by

$$\varepsilon_{ea} = \frac{\sigma_a}{E} = \frac{\sigma'_f}{E}(2N_f)^b, \tag{1.19}$$

and the plastic part is given by

$$\varepsilon_{pa} = \varepsilon'_f(2N_f)^c. \tag{1.20}$$

Combining these equations gives an equation relating the total strain amplitude ε_a and life [10],[10]:

$$\varepsilon_a = \frac{\sigma'_f}{E}(2N_f)^b + \varepsilon'_f(2N_f)^c, \tag{1.21}$$

where N_f is the number of cycles to failure, E is the elasticity modulus, σ'_f the fatigue strength coefficient, ε'_f fatigue ductility coefficient, and b and c fatigue strength and fatigue ductility exponents, respectively. To obtain N_f for a given value of ε_a, the mathematical form of this equation requires either a graphical or numerical solution. An

equation of this form is generally called the Coffin-Manson relationship, which name arises from the separate development of related equations in the late 1950s by both L.F.Coffin and S.S.Manson [38]. Note that the equation of the elastic strain part, provides the stress-life relationship [10]:

$$\sigma_a = \sigma'_f (2N_f)^b. \tag{1.22}$$

Strain-life data and values for the constants for the strain-life and cyclic stress-strain curves are available for a variety of engineering metals.

These parameters can be easily obtained from the experimental curves, taking the logarithmic form of the above equations:

$$\sigma_a = \sigma'_f (2N_f)^b \Leftrightarrow 2N_f = (\frac{\sigma_a}{\sigma'_f})^{\frac{1}{b}} \Leftrightarrow \log 2N_f = \frac{1}{b}\log \sigma_a - \frac{1}{b}\log \sigma'_f, \tag{1.23}$$

which has the form of $y = mx + d$, where

$$\begin{gathered} y = \log 2N_f; \\ x = \log \sigma_a; \\ m = \tfrac{1}{b}; \\ d = -\tfrac{1}{b}\log \sigma'_f. \end{gathered}$$

Performing a linear least-square fit, one can obtain the constants b and σ'_f. To obtain the remaining constants, proceed the same way for the equation:

$$\varepsilon_{pa} = \varepsilon'_f (2N_f)^c \Leftrightarrow 2N_f = (\frac{\varepsilon_{pa}}{\varepsilon'_f})^{\frac{1}{c}} \Leftrightarrow \log 2N_f = \frac{1}{c}\log \varepsilon_{pa} - \frac{1}{c}\log \varepsilon'_f, \tag{1.24}$$

which has the form of $y = mx + d$, where

$$\begin{gathered} y = \log 2N_f; \\ x = \log \varepsilon_{pa}; \\ m = \tfrac{1}{c}; \\ d = -\tfrac{1}{c}\log \varepsilon'_f. \end{gathered}$$

Mean Stress effects

Mean stress effects need to be evaluated in applying the strain-based approach. In particular, the strain-life curve for completely reversed loading needs to be modified if a mean stress is different than zero.

The most used relationships, shown by Dowling [39], are the Walker and the Smith, Watson and Topper (SWT) represented in

$$\varepsilon_a = \frac{\sigma'_f}{E}\left[2N_f\left(\frac{1-R}{2}\right)^{\frac{1-\gamma}{b}}\right]^b + \varepsilon'_f\left[2N_f\left(\frac{1-R}{2}\right)^{\frac{1-\gamma}{b}}\right]^c; \tag{1.25}$$

$$\varepsilon_a = \frac{\sigma'_f}{E}\left[2N_f\left(\frac{1-R}{2}\right)^{\frac{1-\gamma}{2b}}\right]^b + \varepsilon'_f\left[2N_f\left(\frac{1-R}{2}\right)^{\frac{1-\gamma}{2b}}\right]^c, \tag{1.26}$$

respectively, where R is the ratio between the minimum and the maximum stress:

$$R = \frac{\sigma_{min}}{\sigma_{max}}. \tag{1.27}$$

Additional effort and experiments are necessary for the determination of parameter γ. Some high-strength aluminium alloys have parameter $\gamma = 0.5$, which coincides with the SWT method, but higher values of γ apply to low-strength aluminium alloys [40]. Dowling et al. [41] found the value of γ to be approximately 0.65 for low strength aluminium alloys. Therefore, the number of cycles to failure (N_f) can be easily obtained from equation 1.25, for a given strain amplitude.

Chapter 2

Numerical model and parameter identification procedure

The numerical model is the first thing to define in every finite element analysis, because it will determine the materials behaviour. Since time and temperature are very important variables in the present problem, the model must be thermoviscoplastic with creep. The selected model for this work is the Norton's model, represented by the equation

$$\dot{\varepsilon}_{\mathrm{cr}} = C_1 \sigma^{C_2} \exp\left(-\frac{C_3}{T}\right), \tag{2.1}$$

for being the most widely used and because it's implemented in the FEA Program ANSYS. The material dependent constants C_1, C_2 and C_3 need to be defined. The procedure started by gathering creep curves of aluminium 1100-O, since no data was found for alloy 1050-H24.

Using the experimental data, the creep model constants are found through two different ways. The first one consists on an analytical approach, where the constants are obtained by a direct fitting of the logarithmic form of the model equation. The second approach, called the numerical approach, consists on solving an optimization problem, where the objective function quantifies the comparison of the experimental data with the simulation values.

2.1 Experimental Data

The experimental data was retrieved in [42], where stress-strain curves were taken from creep tests performed at different strain rates and different temperatures. Figures 2.1 and 2.2 represent some of these curves (with points).

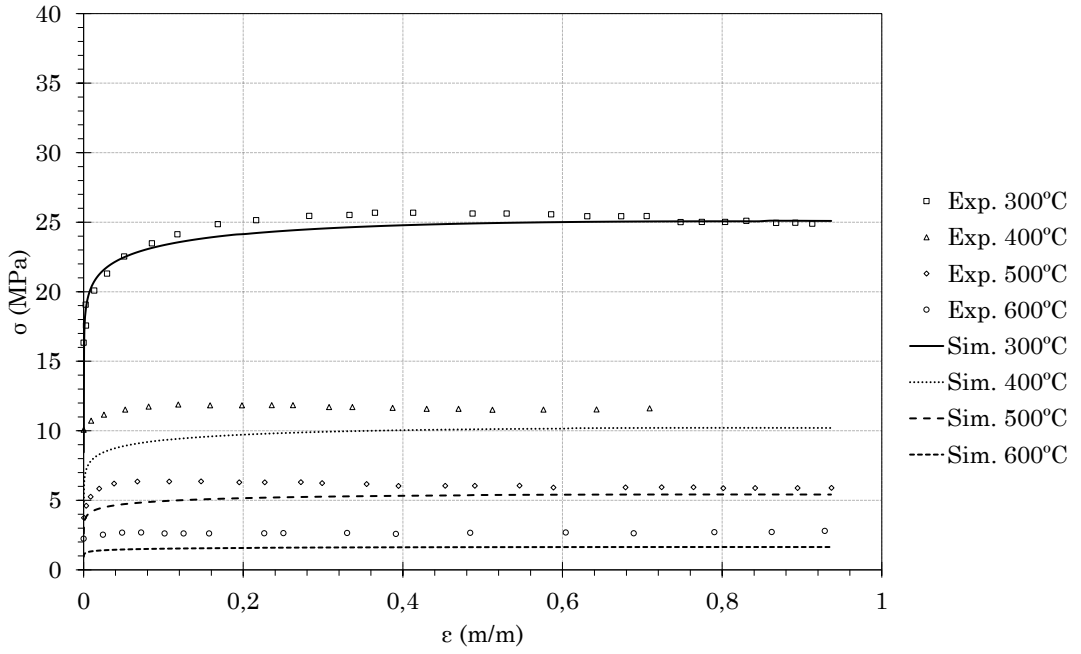

Figure 2.1: Comparison between experimental and simulated results for $\dot{\varepsilon} = 0,001\text{s}^{-1}$.

2.2 Analytical Approach

2.2.1 Calculation of C_2

Taking the logarithmic form of the Norton creep model and rewriting it with the stress in evidence, the equation becomes

$$\ln \dot{\varepsilon} = \ln C_1 + C_2 \ln \sigma - \frac{C_3}{T} \Leftrightarrow \ln \sigma = \frac{1}{C_2} \ln \dot{\varepsilon} - \frac{1}{C_2} \ln C_1 + \frac{1}{C_2} \frac{C_3}{T}. \tag{2.2}$$

Making the derivative of $\ln \sigma$ as function of $\ln \dot{\varepsilon}$, the following expression allows the calculation of C_2, which represents the slope of the logarithmic form of strain rate versus the logarithmic form of stress plot (see figure 2.3).

$$\frac{\partial \ln \sigma}{\partial \ln \dot{\varepsilon}} = \frac{\partial}{\partial \ln \dot{\varepsilon}} \left(\frac{1}{C_2} \ln \dot{\varepsilon} - \frac{1}{C_2} \ln C_1 + \frac{1}{C_2} \frac{C_3}{T} \right) = \frac{1}{C_2} \Rightarrow C_2 = \frac{\partial \ln \dot{\varepsilon}}{\partial \ln \sigma}. \tag{2.3}$$

In this work, 4 points at different strain rates are used, for each 4 temperatures. For each group of 4 point a linear regression was used to obtain the slope. Thus, the final value of $C_2 = 6,76$ is calculated through the average of the 4 values.

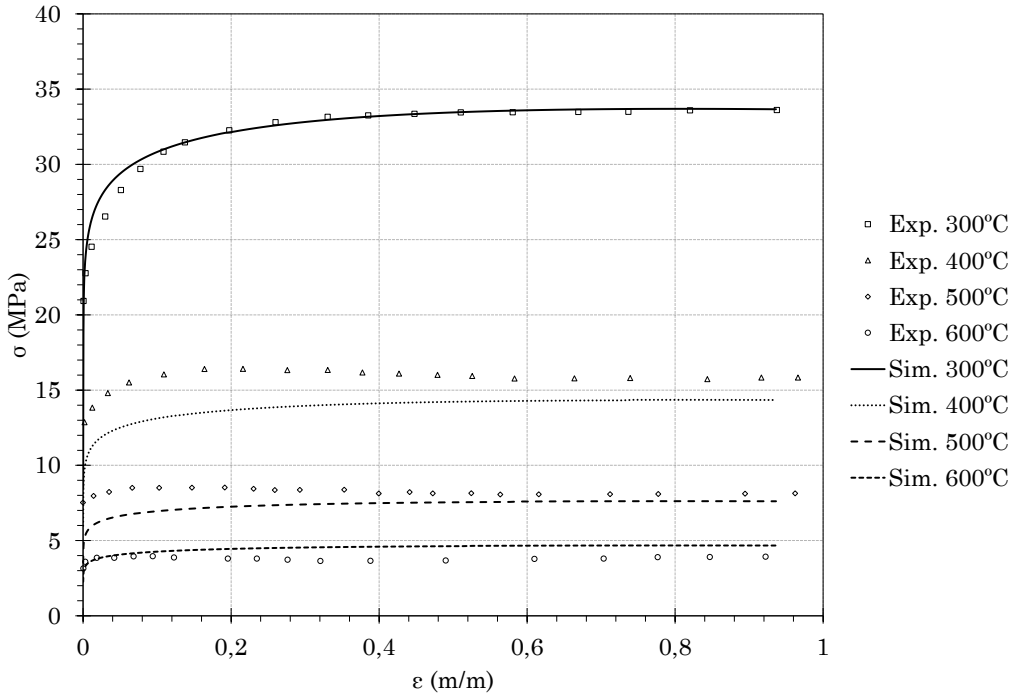

Figure 2.2: Comparison between experimental and simulated results for $\dot{\varepsilon} = 0,01\text{s}^{-1}$.

2.2.2 Calculation of C_3

For the calculation of C_3, the logarithmic of stress is derived in function of reciprocal temperature, obtaining

$$\frac{\partial \ln \sigma}{\partial (1/T)} = \frac{\partial}{\partial \ln (1/T)} \left(\frac{1}{C_2} \ln \dot{\varepsilon} - \frac{1}{C_2} \ln C_1 + \frac{1}{C_2} \frac{C_3}{T} \right) = \frac{C_3}{C_2} \Rightarrow C_3 = C_2 \frac{\partial \ln \sigma}{\partial (1/T)}. \quad (2.4)$$

In this case, the slope corresponds to the quotient between constant C_3 and C_2. As C_2 is already defined, C_3 can be calculated. Figure 2.4 presents 4 curves for different strain rates, where each point of each curve corresponds to different temperatures. The constant C_3 is calculated through the average of the 4 groups, multiplied by the value of C_2. The value found is C_3=22300,5.

2.2.3 Calculation of C_1

The constant C_1 is calculated using the previous calculations. From equation 2.1, C_1 can be written as

$$\begin{aligned} C_2 \ln \sigma = \ln \dot{\varepsilon} - \ln C_1 + \frac{C_3}{T} \Leftrightarrow \ln C_1 = \ln \dot{\varepsilon} + \frac{C_3}{T} - C_2 \ln \sigma \Leftrightarrow \\ \Leftrightarrow C_1 = \exp \left(\ln \dot{\varepsilon} + \frac{C_3}{T} - C_2 \ln \sigma \right). \end{aligned} \quad (2.5)$$

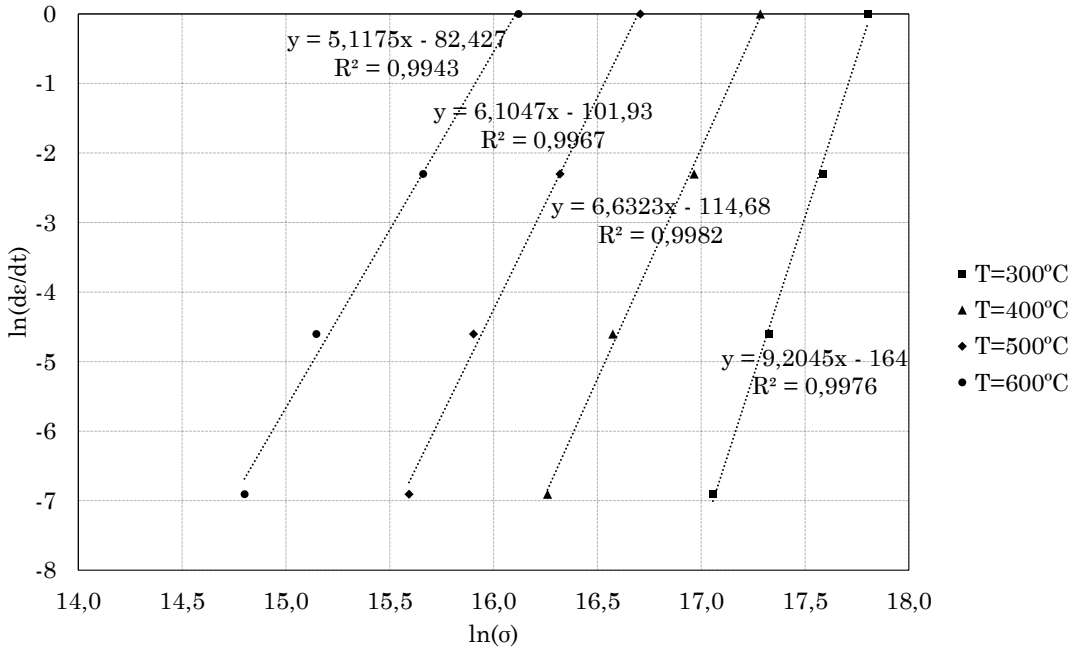

Figure 2.3: Calculation of C_2 using the fitting of $\ln \dot{\varepsilon}$ vs $\ln \sigma$ plot.

The value of C_1 is found using the same experimental data and an average fitting using 4 levels of strain rate and temperature. The value found is $C_1 = 1,28 \times 10^{-36}$.

2.2.4 Results

The final values of the Norton's creep model constants for the AA1100-O are presented in the table 2.1. A creep test was carried out with the FEA program ANSYS. Figures 2.1 and 2.2 compare the simulated results with the experimental data, where the dots correspond to the experimental data and the lines to the simulation results. The results presented in figures 2.3 and 2.4 correspond only to a strain of 0,58, where the best results were obtained.

The obtained constants were compared with the articles [43] and [44], where in the first: $C_1 = 4,13 \times 10^{-2}$, $C_2 = 5,2$, $C_3 = 19726,8$; and in the second: $C_1 = 2,147 \times 10^{-70,03}$, $C_2 = 10,171$, $C_3 = 50825,89$. The constant C_1 shows a huge variation from one article to another. Thus, it's difficult to ensure the viability of the obtained result despite being in between the two values. On the other hand, the values of the constants C_2 and C_3 are in agreement with the reference data, since they have the same order of magnitude.

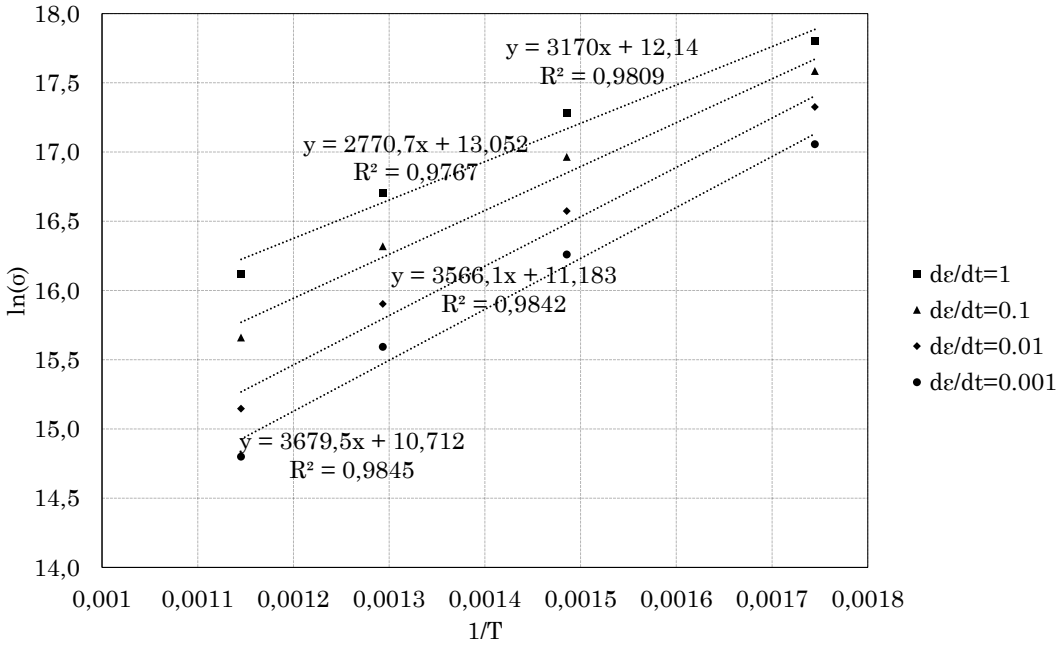

Figure 2.4: Calculation of C_3 using a $\ln\sigma$ vs $1/T$ plot.

Table 2.1: Final values obtained with the analytical and numerical approaches and the respective comparison for the Norton's creep model constants for the AA1100-O.

	Analytical	Numerical	Difference (%)
C_1	$1,28 \times 10^{-36}$	$1,2826 \times 10^{-36}$	0,20
C_2	6,76	6,9855	3,34
C_3	22300,5	24501	9,87

2.3 Numerical Approach

The numerical approach consists in solving an optimization process, where its intended to improve the results obtained through the analytical approach. Therefore, the ANSYS optimization module [12] was used in order to improve the fitting of the simulation results with the experimental data. Schematically, the process can be represented by figure 2.5, where the process begins with the estimation of the model parameters, obtained by the analytical approach. Then, the model runs for the desired conditions (temperature, for example), and the corresponding results are extracted from the simulation and are compared, for a given number of points, to the correspondent experimental data. This comparison is made through a residual sum squares, where the sum of the square difference between the numerical value of equivalent stress (σ_i^{Num}) and the experimental (σ_i^{Exp}), for the same level of strain, for each i point is calculated by:

$$F_{\mathrm{obj}} = \sum_{i=1}^{N} \left(\sigma_i^{\mathrm{Num}} - \sigma_i^{\mathrm{Exp}}\right)^2. \tag{2.6}$$

The ANSYS Optimization module [12] is a set of constrained, multi-objective optimization techniques in which the best possible designs can be obtained. Among the available optimization methods, the NLPQL (Nonlinear Programming by Quadratic Lagrangian) was used.

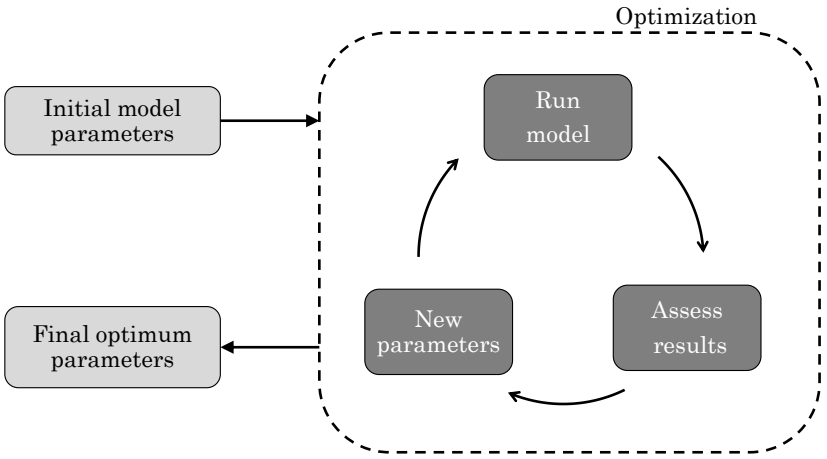

Figure 2.5: Scheme of the optimization process for material curve fitting.

The NLPQL approach is a gradient-based single-objective optimizer that is based on quasi-Newton methods [12]. This method was chosen since it's the only that needs the initial estimation of the parameters and where the parameters search universe could be defined, making the process more accurate and faster.

This iterative method automatically generates a set of different parameter values, in which, for every cycle, produces the deviation result and updates the parameter values.

The process ends when a stopping criterion is reached. Figure 2.6 shows the ANSYS Workbench project scheme for this process.

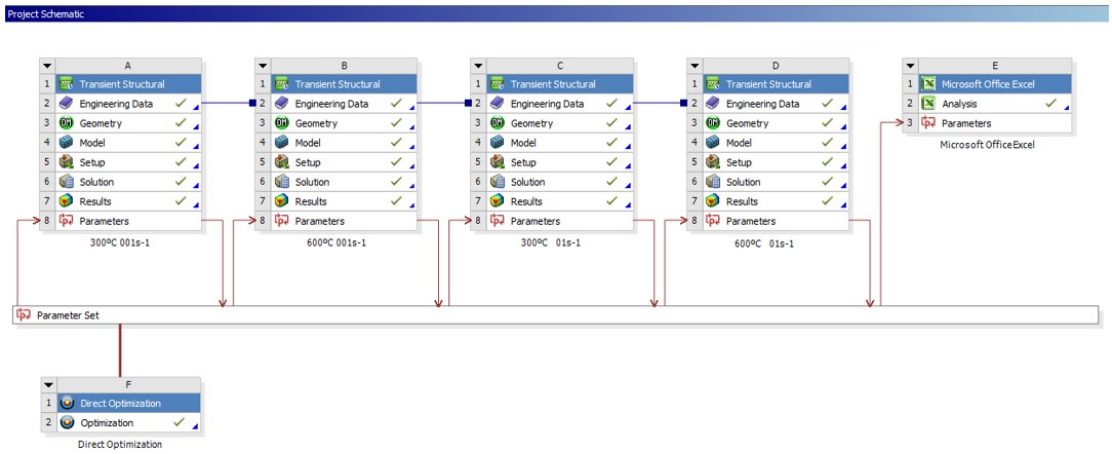

Figure 2.6: ANSYS Workbench project scheme for material curve fitting.

2.3.1 Results

The results obtained through the numerical approach are presented in table 2.1. Only 1 stress point was compared in each cycle, for a corresponding strain value of 0,92. Figures 2.7 and 2.8 illustrate the difference between the simulated results and the experimental data.

The constants obtained through the numerical approach, compared to the analytical approach have a difference of 0,2% for the C_1, 3,34% for the C_2 and 9,87% for C_3 (see table 2.1). However, they all have the same order of magnitude. The difference between the simulated and the experimental curves, with the constants obtained through both approaches, can be interpreted by a relative error, given by

$$\text{Error } [\%] = 100\left(1 - \frac{\mathrm{A_i}^{\mathrm{sim}}}{\mathrm{A_i}^{\mathrm{exp}}}\right), \tag{2.7}$$

where $\mathrm{A_i}^{\mathrm{sim}}$ and $\mathrm{A_i}^{\mathrm{exp}}$ are the areas below the simulated and experimental curves, respectively. The error values are shown in table 2.2, where on average, the values for the numerical approach are lower than those obtained analytically. However, for the curves with $\dot{\varepsilon} = 0,01\ \mathrm{s}^{-1}$, T=300°C and T=600°C, the numerical approach reveals worse results. Nevertheless, the constants obtained through the numerical approach give, in general, better results.

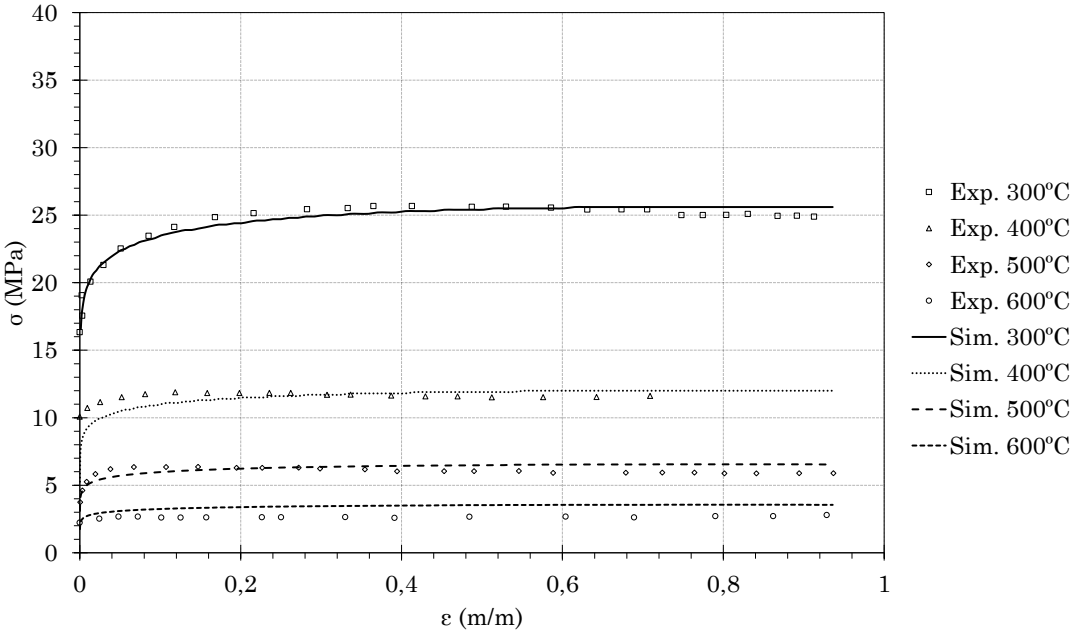

Figure 2.7: Comparison between experimental and simulated results for $\dot{\varepsilon} = 0,001\text{s}^{-1}$.

Table 2.2: Relative error between the simulated and the experimental curves.

	Error [%]			
	$\dot{\varepsilon} = 0,001\text{s}^{-1}$		$\dot{\varepsilon} = 0,01\text{s}^{-1}$	
	Analitycal	Numerical	Analitycal	Numerical
T=300 °C	7,03	0,55	0,34	7,25
T=400 °C	16,48	1,65	15,12	0,02
T=500 °C	13,37	4,62	12,72	5,45
T=600 °C	39,88	29,35	15,35	23,34
Average	19,19	9,04	10,88	9,01

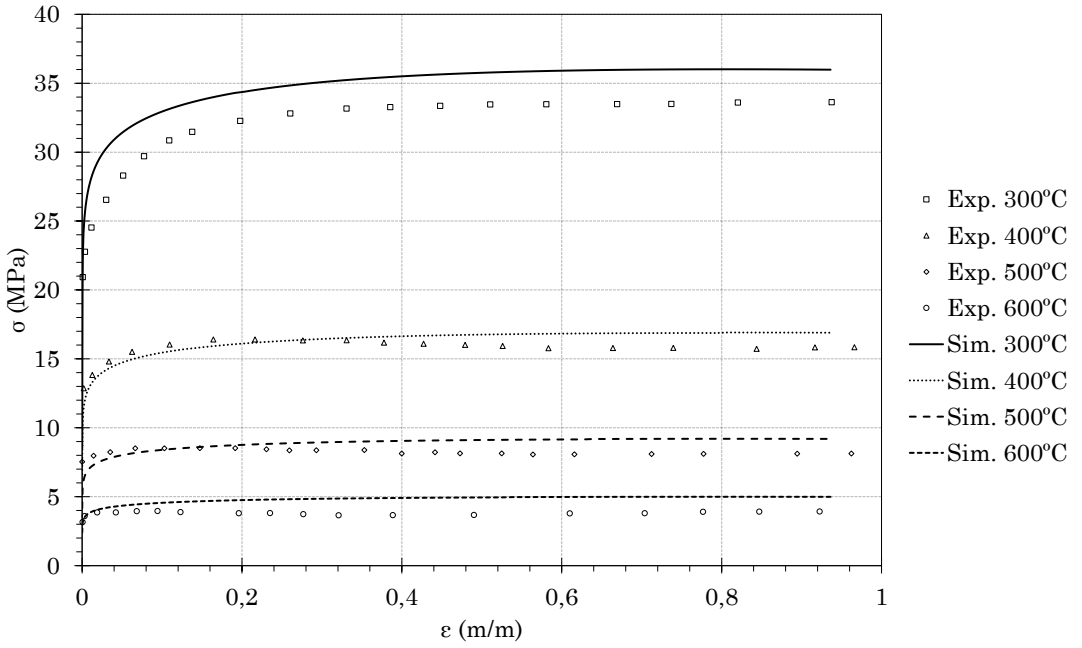

Figure 2.8: Comparison between experimental and simulated results for $\dot{\varepsilon} = 0,01\text{s}^{-1}$.

Chapter 3

Burner Simulation

3.1 Introduction

To understand the burner surface's behavior, the thermal and structural analysis should be performed. Considering that time is a very important variable in the current problem, both analysis must be transient. The coupled thermal and structural modules allow to obtain the temperature profile over time as well as the stress and deformation which are time and temperature dependent. Figure 3.1 shows this process, where the model (discretized in a finite element mesh) and the material properties remain the same.

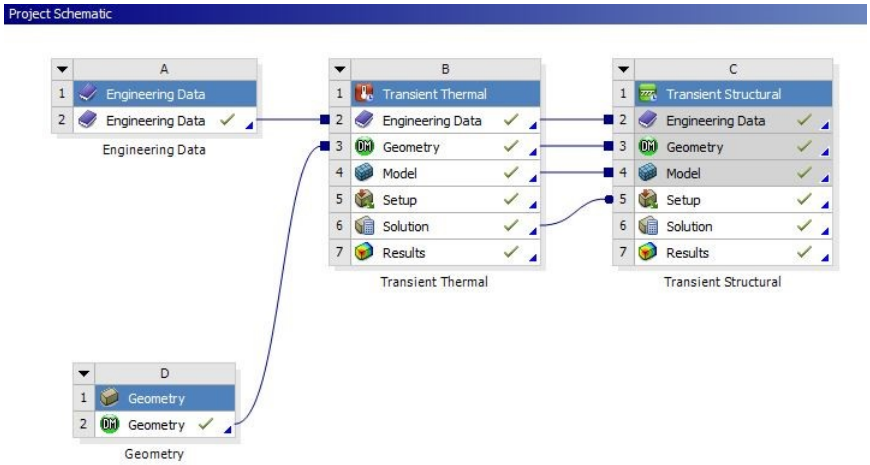

Figure 3.1: Scheme of the thermal and structural simulations at ANSYS Workbench.

There are some assumptions and simplifications that are made in the numerical analysis:

1. Just one plate of the surface is considered in the simulation, assuming that all of them are at the same temperature. However, this is an approximation because the plate near the water inlet is slightly colder that the middle plate. Experimentally, the difference between the water inflow and outflow is about 2,5°C. Thus, this assumption does not compromise the simulation results.

2. It is assumed that every plate is exposed to the same amount of radiation coming from the flames. Actually, the flame behaves non-homogeneously. However, considering the same heat transfer in all surface, the worst case scenario is considered.

3. The heat transfer losses are not considered in the analysis. The flame starts above the surface, the pressure arises, letting the atmospheric air to mix with the combustion gases. This can cause an air flow, which can be responsible for removing some amount of heat by convection. However, it is rather difficult to quantify and account for these heat losses.

3.2 Geometry

Since the boundary conditions and the geometry are symmetric, the model was reduced to a quarter of the original, allowing time savings and a mesh refinement in the simulation. Thus, symmetry was applied on the corresponding faces of planes Oxy and Oxz, as shown in figure 3.2.

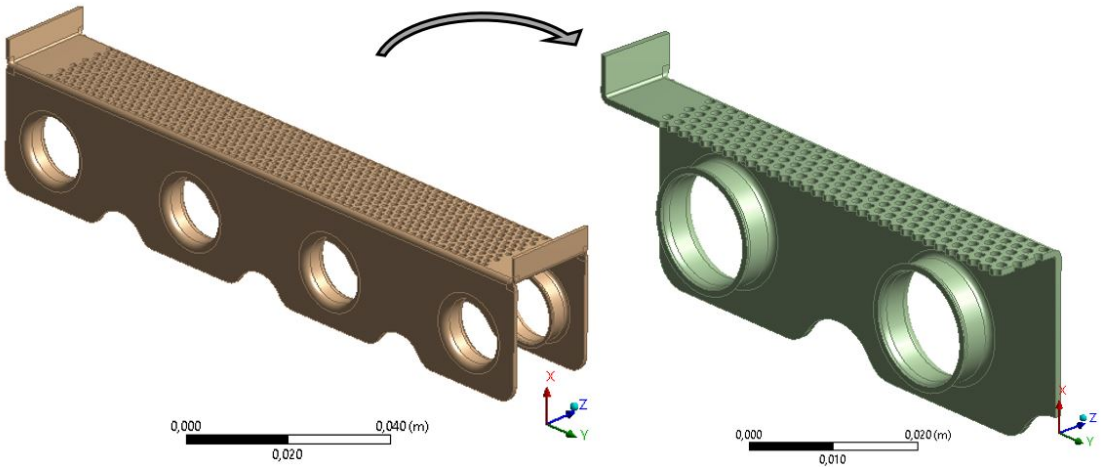

Figure 3.2: Geometric symmetry applied on the initial model.

3.3 Material Properties

The burner is constituted of an aluminum series AA1050-H24. These properties were mainly obtained through the Bosch database *Bosch Matis* and are shown in table 3.1. For the structural analysis, the creep behavior was found as presented in chapter 2. Table 3.2 lists the creep model constants for the Norton's creep model.

Table 3.1: Aluminum 1050-O material properties based on Bosch Matis database, except for the Young's modulus and the coefficient of Poisson.

Temperature (°C)	Young's Modulus (GPa) [45]	Poisson coefficient [45]	Thermal Expansion coefficient ($°C^{-1}$)
-50	70	-	$2,17 \times 10^{-5}$
20	70	0,3365	-
50	69	0,3382	-
100	68	0,3416	$2,35 \times 10^{-5}$
150	66	0,3451	-
200	63	0,3485	$2,44 \times 10^{-5}$
250	57	0,3519	-
300	50	0,3560	$2,54 \times 10^{-5}$
Density (kgm^{-3})	2700		
Specific Heat ($Jkg^{-1}K^{-1}$)	900		
Thermal conductivity ($Wm^{-1}K^{-1}$)	210-220		
Emissivity	0,05		
Yield Strength (MPa)	65-95		
Tmelting (°C)	645-658		

Table 3.2: Creep model constants used on structural simulations.

Creep model constants	
C_1	$1,2826 \times 10^{-36}$
C_2	6,9855
C_3	24501

3.4 Boundary Conditions

3.4.1 Thermal analysis

The most critical thermal loads reaching the surface are the radiation emitted by the flames and the heat transfer by the water cooling system. Nevertheless, there is also convection due to the gas flow on the interior faces of the surface that needs to be considered.

The water cooling system has an impact on the surface temperature due to:

- convection by the water flow inside the copper tube;
- conduction through the tube thickness;
- thermal contact resistance between the copper tube and aluminum surface joint.

Therefore, an equivalent heat transfer coefficient is calculated in order to quantify the impact of the water cooling system on the temperature profile of the burner's surface.

Equivalent heat transfer coefficient due to the water cooling system

The water volumic flow convection coefficient is calculated through the Nusselt number. The Reynolds number is obtained by the following expression [46]:

$$Re_D = \frac{4\dot{m}}{\pi D \mu}, \tag{3.1}$$

where $\dot{m}$ is the water flow rate, in kg/s; D is the copper tube internal diameter and μ the viscosity of water, in $\mathrm{kgm^{-1}s^{-1}}$ at $\sim$20°C. Since the flow is found to be turbulent, the Nusselt number can be calculated by the expression

$$Nu_D = \frac{(f/8)(Re_D - 1000)\,\mathrm{Pr}}{1 + 12,7(f/8)^{1/2}(\mathrm{Pr}^{2/3} - 1)} \tag{3.2}$$

which is valid for the conditions

$$3000 \leqslant Re_D \leqslant 5 \times 10^6,$$
$$0,5 \leqslant \mathrm{Pr} \leqslant 2000,$$
$$L/D \geqslant 10,$$

where f is the Darcy friction factor that can either be obtained from the Moody chart or for the following expression, for $Re_D \leqslant 2 \times 10^4$,

$$f = 0,316 Re_D^{-1/4}. \tag{3.3}$$

The convection coefficient through water flow can be obtained by the definition of Nusselt number, where k_w is the thermal conductivity of the water, at $\sim$ 20°C:

$$Nu_D = \frac{hD}{k} \Leftrightarrow h = \frac{Nu_D k_w}{D}. \tag{3.4}$$

Then, the heat conduction resistance though the copper tube is defined. Since the tube has a circular section, the resistance is calculated by the following equation where r_i and r_e are the internal and external diameter, respectively, and k_{Cu} the thermal conductivity of copper tube:

$$R_{\mathrm{conduction}} = \frac{r_i}{k_{Cu}} \ln\left(\frac{r_e}{r_i}\right). \tag{3.5}$$

The calculation of the heat transfer through the contact between copper tube and the aluminum surface is obtained knowing the contact pressure between the two solids. To find this value of pressure, two analyses were performed:

- **An analytical approach** which is an 1D approximation of the problem, to find its order of magnitude. The initial conditions are illustrated in figure 3.3 and its dimensions described in table 3.3.

  The maximum strain of copper tube can be calculated considering the engineering stress and strain, knowing that the maximum diameter is obtained by the expansion tool diameter:

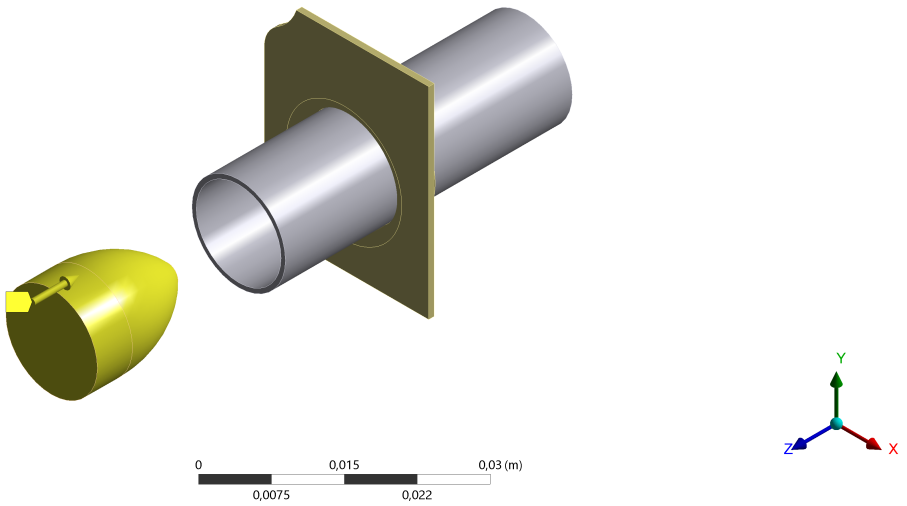

Figure 3.3: Representation of copper tube and aluminum surface expansion.

Table 3.3: Initial conditions for the analytical approach.

Initial copper tube exterior diameter	$D_{\mathrm{e_{Cu}}} = 13,6$ mm
Copper tube thickness	$t_{\mathrm{Cu}} = 0,6$ mm
Expansion tool diameter	$D_{\mathrm{f}} = 13,3$ mm
Initial Aluminum Joint diameter	$D_{\mathrm{i_{Al}}} = 13,6$ mm

$$\varepsilon_{c,max} = \frac{\Delta D_{Cu}}{\Delta D_{i_{Cu}}} = \frac{D_f - D_{i_{Cu}}}{D_{i_{Cu}}} = \frac{13,3-12,4}{12,4} = 0,072581$$

The maximum stress is obtained from the tensile test curve of Copper, figure 3.4, at 20°C and $0,0001\ s^{-1}$ of strain rate [47], where a value of 0,072 corresponds to a stress of 130 MPa approximately (see figure 3.4).

The final strain of copper tube is obtained considering its elastic recovery strain, which is calculated by the value of stress divided by the Elastic Modulus, equal to 127 GPa[1].

$$\varepsilon_{Cu,final} = \varepsilon_{Cu,max} - \frac{\sigma_{Cu,max}}{E_{Cu}} = 0,072581 - \frac{130}{127\times10^3} = 0,071557$$

With this value, it's possible to obtain the maximum and final value of copper tube diameter:

$$D_{Cu,max} = D_{e,Cu}\,(1+\varepsilon_{Cu,max}) = 13,6(1+0,072581) = 14,5871 \text{ mm},$$
$$D_{Cu,f} = D_{e,Cu}\,(1+\varepsilon_{Cu,final}) = 13,6(1+0,071557) = 14,5718 \text{ mm}.$$

The aluminum strain, using the aluminum initial joint diameter and the maximum copper tube diameter is calculated as

[1] Value found in Bosch Matis database.

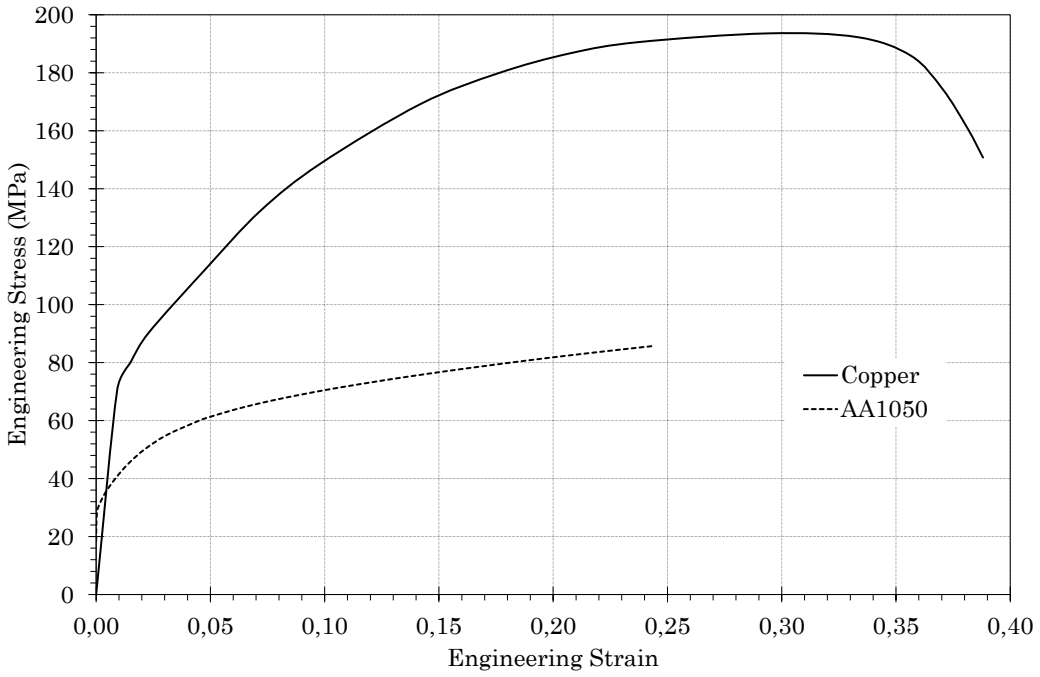

Figure 3.4: Copper and aluminum tensile test curves.

$$\varepsilon_{Al,max} = \frac{\Delta D_{Al}}{\Delta D_{i_{Al}}} = \frac{D_{Cu,max} - D_{i_{Al}}}{D_{i_{Al}}} = \frac{14{,}5871 - 13{,}6}{13{,}6} = 0{,}072581.$$

Proceeding the same way for Aluminum, from the tensile test represented in figure 3.4, the maximum stress is approximately 70 MPa, corresponding to a final stress of:

$$\sigma_{Al,final} = \sigma_{Al,max} - E_{Al}\frac{D_{e,Cu}\left(\varepsilon_{Cu,max} - \varepsilon_{Cu,final}\right)}{D_{i_{Al}}} = 70 - 70\times10^{-3}\,\frac{13{,}6(0{,}072581 - 0{,}071557)}{13{,}6}$$

$$\approx 70 \text{ MPa}.$$

- **A numerical approach** to support the results obtained in the above calculations. Hence, a geometry of the aluminum surface and a tool of stainless steel, modeled as a rigid body, were used to simulate the expansion process (see figure 3.5).

  Using the explicit dynamics module in FEA program ANSYS's analysis system [12], the relation between the tool and the copper tube is defined as frictionless as the contact between the copper tube and the aluminum surface.

  The aluminum surface was constraint in its laterals, allowing to see the joint deformation. To obtain the results for both aluminum and copper surfaces, a path was defined along the surface (see figure 3.6). The results are compared to the analytical ones, as presented in table 3.4. The contact pressure was obtained through the average node values between the two surfaces (see figure 3.7).

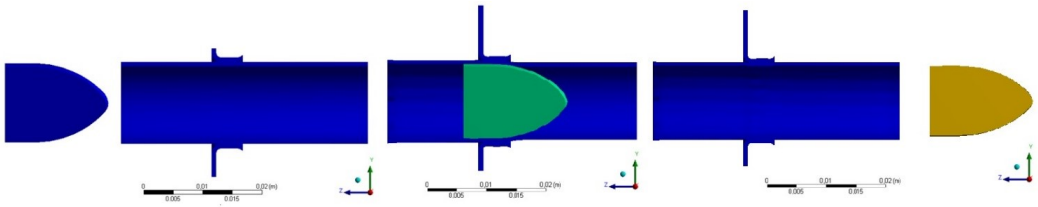

Figure 3.5: Sequence of the expansion process simulated in ANSYS program.

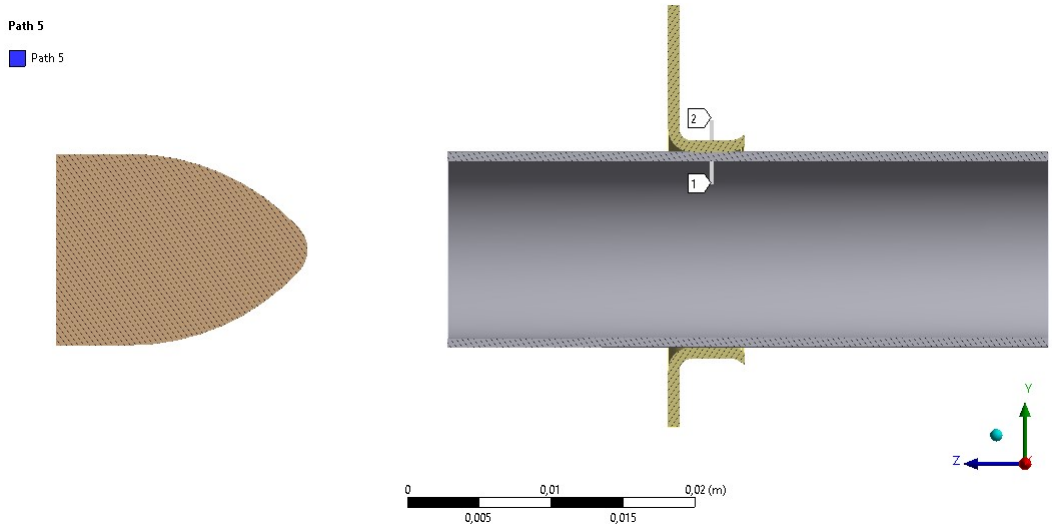

Figure 3.6: Representation of the path along the geometry where the results were found.

Table 3.4: Comparison between the analytical and the numerical solutions for the copper tube expansion process.

		Analytical Results	Numerical Results
Copper tube	Strain	0,07156	0,07768
	Deformation (m)	0,00049	0,00044
	Maximum Stress (MPa)	130	123,43
Aluminum surface	Strain	0,07158	0,07418
	Maximum Stress (MPa)	70	77,09
	Contact Pressure (MPa)	18,9	

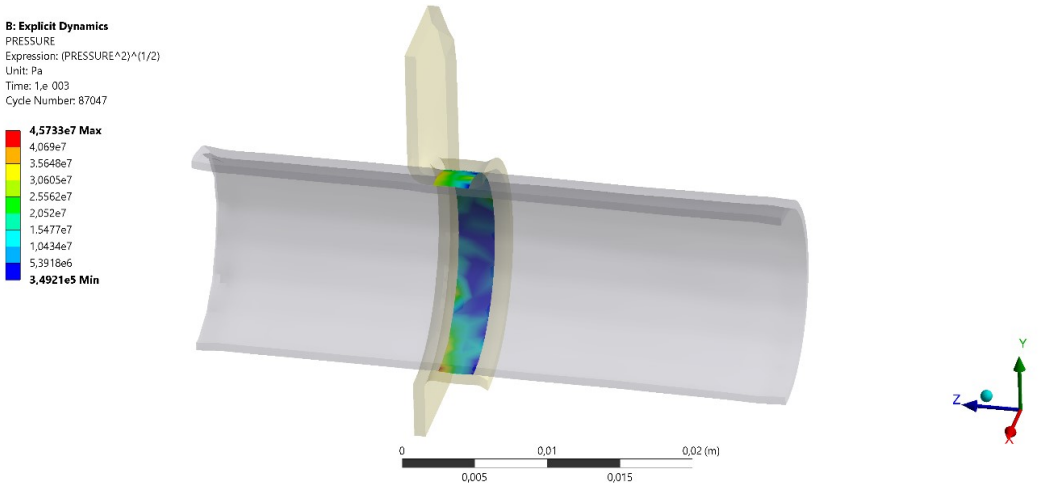

Figure 3.7: Contact pressure between the copper tube and the aluminum surface.

The copper tube is assembled by expansion, this coefficient is calculated based on the contact pressure between the copper and aluminum surfaces. To calculate the thermal contact resistance between the copper tube and the aluminum surface as function of contact pressure (P), a set of models were analyzed and are presented in table 3.5, where h_c is the thermal contact heat transfer coefficient. The model selected for the current problem was proposed by Song and Yovanovich [48] and is represented by:

$$\frac{P}{H_c} = \left(\frac{P}{\left[c_1 \left(1,62\frac{\sigma}{m}\right)\right]^{c_2}} \right)^{\frac{1}{1+0,071c_2}}, \tag{3.6}$$

$$h_c = 1,25\frac{k_s m_s}{\sigma_s}\left(\frac{P}{H_c}\right)^{0.95}, \tag{3.7}$$

where the parameters meaning and units are presented in table 3.6.

Table 3.5: Models for the calculation of the thermal contact heat transfer as function of contact pressure [1].

Author	Model
Tien, 1968	$h_c = 0.55 \frac{k_s m_s}{\sigma_s} \left(\frac{P}{H_c}\right)^{0.85}$
Cooper, Mikic and Yovanovich, 1969	$\frac{h_c \sigma}{k_s m} \propto \frac{P}{H_c}$ $h_c = 1.45 \frac{k_s m_s}{\sigma_s} \left(\frac{P}{H_c}\right)^{0.985}$
Thomas and Probert, 1972	$\log \frac{h_c A}{\sigma k_s} = C \log \frac{PA}{\sigma^2 H} + D$
Mikic, 1974	$h_c = 1.13 \frac{k_s m_s}{\sigma_s} \left(\frac{P}{H_c}\right)^{0.94}$
Yovanovich, 1982	$h_c = 1.25 \frac{k_s m_s}{\sigma_s} \left(\frac{P}{H_c}\right)^{0.95}$ $10^{-6} \leq \frac{P}{H_c} \leq 2.3 \times 10^{-2}$

Table 3.6: Parameters considered for the analysis and corresponding results.

Parameter	Description	Constants/ Results
P	Contact pressure	18,9 MPa
H_c	Microhardness	0,98 MPa
σ	Surface roughness	$\sigma/m = 21,1 \mu$m
m	Asperity slope [49]	
k_s	Effective thermal conductivity	284,12 W/mK
h_c	Thermal contact heat transfer coefficient	516,24 W/m^{2}K
c_1	Vickers correlation coefficient [49]	1,11 MPa
c_2	Vickers size index [49]	-0,00487

The equivalent heat transfer has the three components represented in figure 3.8, and can be calculated as

$$U = \frac{1}{R_{\text{total}}} = \frac{1}{\frac{1}{h_{\text{conv}}} + \frac{r_i}{k_{\text{Cu}}} \ln \frac{r_e}{r_i} + R_{\text{contact}}} \tag{3.8}$$

The results are listed in table 3.7, where U represents the equivalent heat transfer.

The water flow rate considered in the analysis is 5 l/min, however, this value may vary. Thus, a parameterization of equivalent heat transfer as function of the flow rate was made and is presented in figure 3.9. As expected from expression 3.1 and 3.8, the coefficient increases with a larger water flow rate.

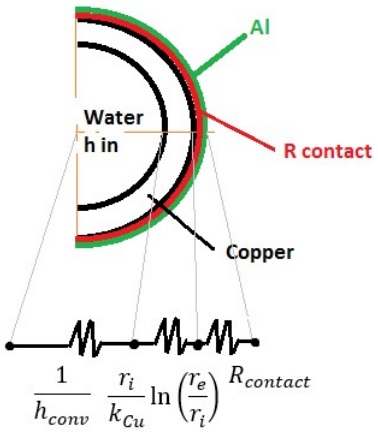

Figure 3.8: Representation of thermal heat transfer circuit.

Table 3.7: Calculation of thermal resistances and overall heat transfer coefficient.

R contact	$1,94 \times 10^{-3}$	m^2K/W
R convection	$2,42 \times 10^{-4}$	
R conduction	$1,43 \times 10^{-6}$	
R total	$2,18 \times 10^{-3}$	
U	458,62	W/m^2K

Radiation

Radiation is the major source of energy that reaches the burner surface. Emissivity is the ratio of the radiation emitted by the surface to the radiation emitted by a blackbody at the same temperature [46]. Emissivity, $0 < \varepsilon < 1$, depends mainly on the material and its surface properties. A polished metal surface has a low emissivity, while a roughened and oxidized metal surface has a high emissivity. The emissivity also depends on the temperature, however, in this work, it is considered constant over the temperature range and its value is assumed to be equal to 0,05, in agreement with ASM International [4], for Aluminum AA1050 series.

The radiation temperature is based on the adiabatic flame temperature of the gas combustion. Since this is a theoretical value, calculated in terms of the combustion

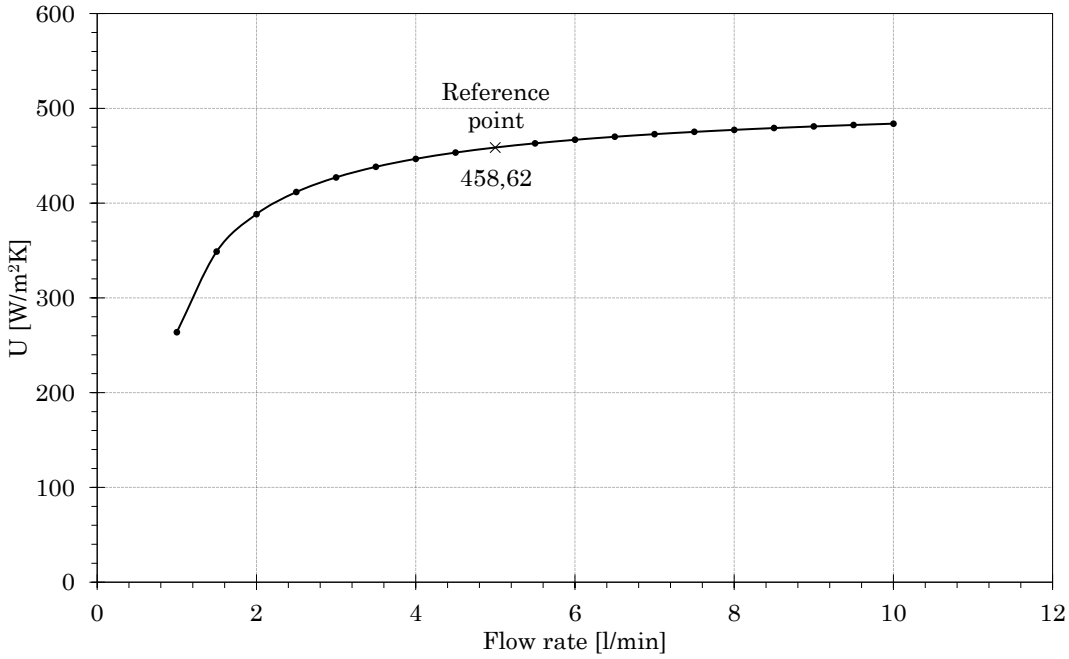

Figure 3.9: Equivalent heat transfer coefficient and convection heat transfer coefficient as function of water flow rate.

stoichiometry, and is very difficult to be measured, it has a low level of accuracy. For the first analysis, an approximation based on bibliography data was made. Figure 3.10 shows the maximum flame's temperature which for methane corresponds to 1200°C ∼ 2000°C between an equivalent ratio of 0,5 to 1. Thus, considering that radiation is caused by a temperature lower than the flame temperature, the assumed value is 1500°C.

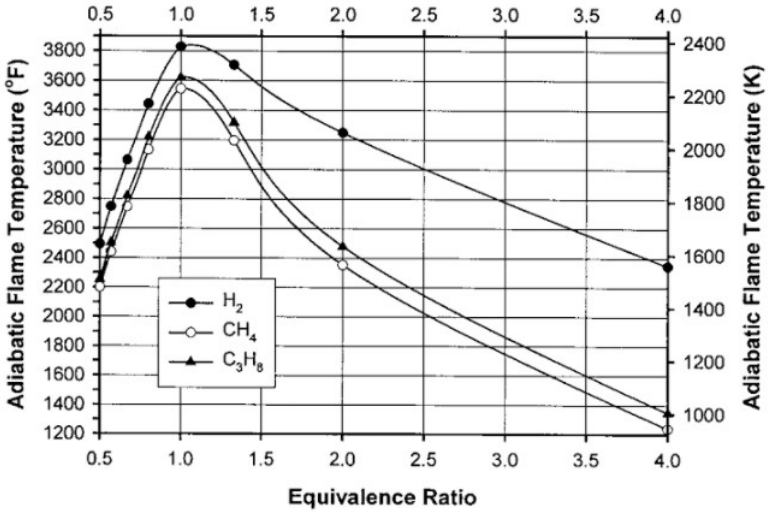

Figure 3.10: Adiabatic equilibrium flame temperature vs. equivalent ratio for air/H_2, air/CH_4 and air/C_3H_8 flames [11].

Convection through the gas flow-calibration of the model

Another boundary condition to consider is the convection through the gas flow on the interior surfaces of the burner. As it is a value difficult to estimate, it was found through an optimization process, where it was intended to obtain the surface temperatures as similar as possible to experimental values measured.

The experimental measurement results are represented in table 3.8 and figure A.4 shows the points where the measurements took place. These values were obtained in stationary regime, after temperature stabilization, through thermocouples placed by contact in-between the burner surfaces. Thus, these measurements can have an error associated with thermal contact resistance.

Table 3.8: Comparison between experimental and numerical temperatures measurements.

	Front Plenum 9	Bottom 1st 10	Tube 2nd bottom 11	Middle 1-2 tube 13	Middle 2-3 tube 14
Experimental (°C)	59,904	22,785	24,271	48,836	42,629
Numerical (°C)	59,903	43,032	42,872	49,907	49,967
Difference (°C)	0,001	20,247	18,601	1,071	7,338
Difference (%)	0	89	77	2	17

The process was accomplished through ANSYS Workbench Optimization module and

it's very similar to the fitting process described in section 2.3. Firstly, in the solution output, 3 lines along the surface were created to cover the experimental points: one passing through the points 10 and 11 (figure 3.11-B); other covering the points 13 and 14 (figure 3.11-A) and the last passing through the point 9 (figure 3.12). In this way, a temperature profile along the length is obtained along with the experimental points.

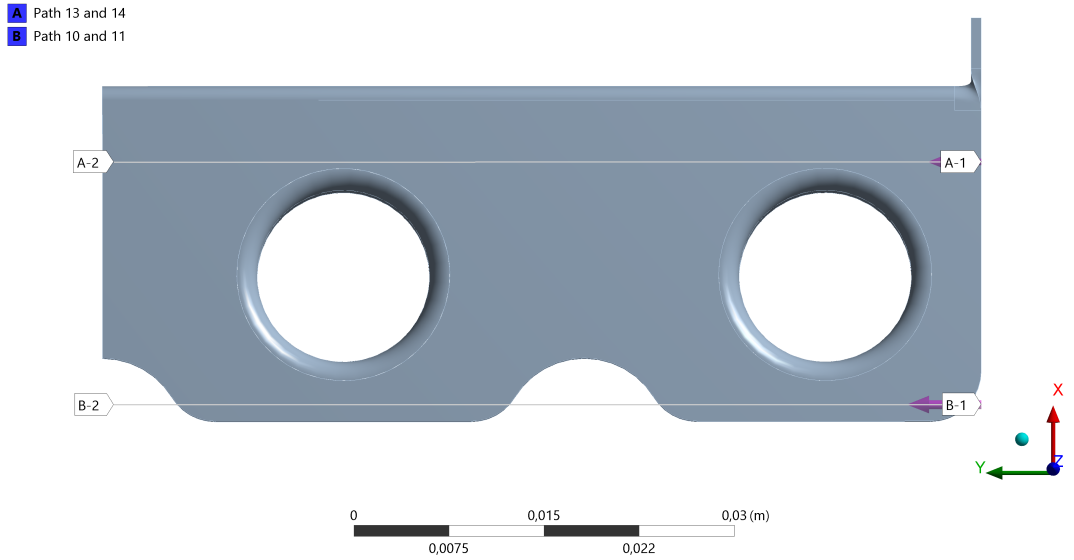

Figure 3.11: Construction line for comparison with experimental points 10, 11, 13 and 14.

In this case, since the maximum temperature is at point 9, the optimization goal consisted on finding h_c that minimize the difference between the experimental and numerical point 9:

$$f_1(T) = |T_9^{\text{Exp}} - T_9^{\text{Num}}| = 0,$$

and simultaneously to minimize

$$f_2(T) = \sum_{i=1} \left(T_9^{\text{Exp}} - T_9^{\text{Exp}}\right)^2,$$

subjected to $h_c > 0$, where the T_i are the temperatures at points $i = \{9, 10, 11, 13, 14\}$. The optimization process in ANSYS is shown in figure 3.13.

Figure 3.14 shows the results of the convection coefficient and the temperature difference at point 9 for the all iterations. The convection coefficient found through this process was 115,79 W/m^2 K with a temperature of 15°C, allowing the temperature differences shown in table 3.8.

The final values can be observed in figure 3.15, where the dots correspond to the experimental measurements and the lines to the temperature profile along the surface length for points 10,11,12 and 13 and along the width for point 9.

The difference between the obtained values of temperature show a good agreement with the experimental data, except for the points with lower temperature (10 and 11), which have, respectivelly, a difference of 89 and 77% compared to the experimental measurements (see table 3.8). However, since the highest temperatures can have a larger

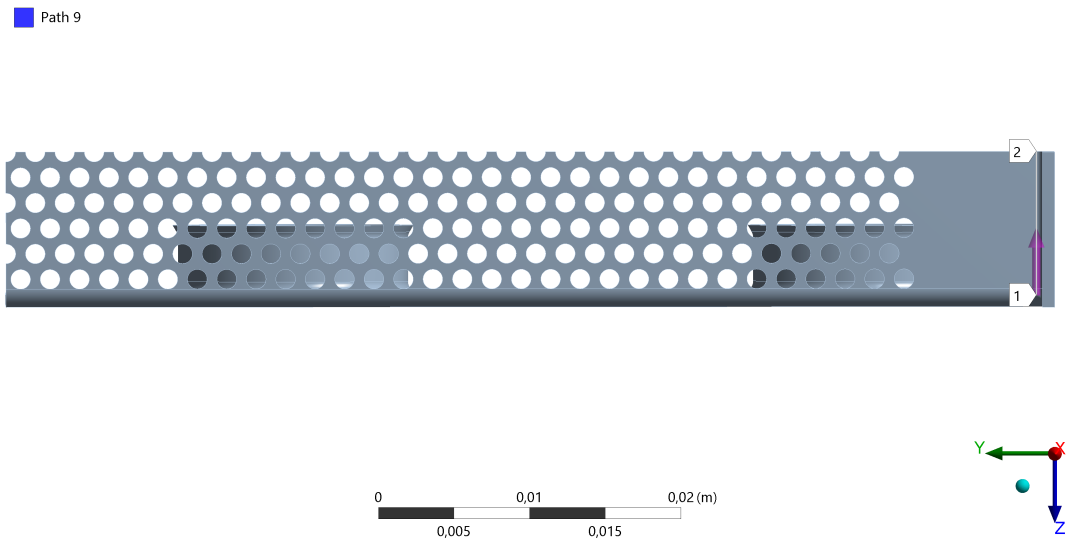

Figure 3.12: Construction line for comparison with experimental point 9.

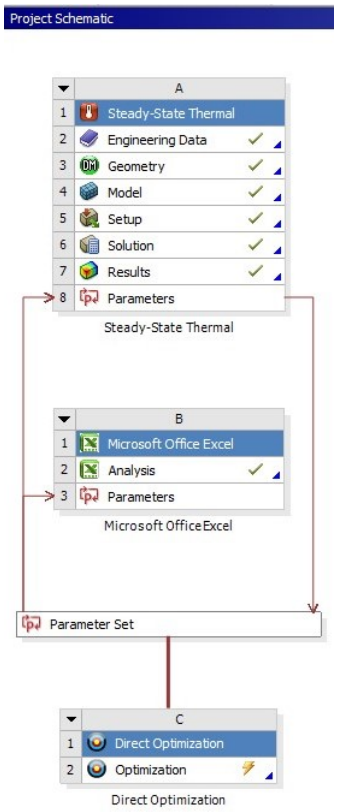

Figure 3.13: Scheme of the optimization process for convection coefficient determination.

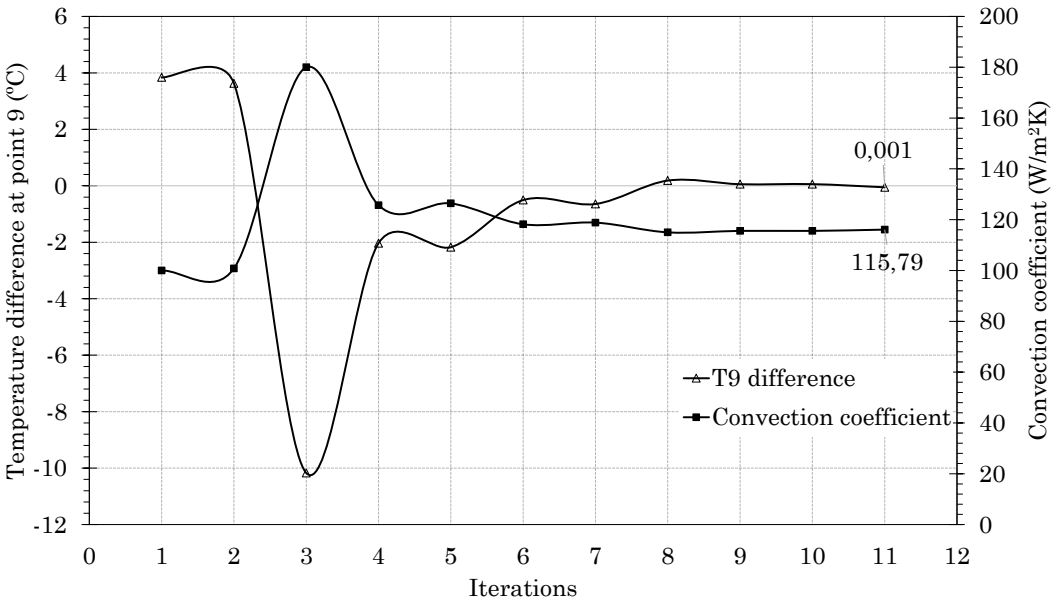

Figure 3.14: Optimization process for thermal calibration.

impact on the mechanical behavior of the surface, this approach focuses on the worst case scenario. The thermal boundary conditions are shown in figure 3.16.

3.4.2 Structural analysis

In the structural analysis, additionally to the thermal loads applied to the body, it was considered that the surface is completely constrained in the tube zones as represented in figure 3.17.

3.5 Mesh and mesh sensitivity analysis

In the Finite Element model of the burner surface, tetrahedral elements were used, specifically, the SOLID187. This element has 10 nodes and full integration, guaranteeing good simulation results (see figure 3.18).

To determine the ideal number of elements, a mesh sensitivity study was made. For 5 different meshes, the number of nodes and elements progressively increased and the exact values used are represented in the table 3.9. For each mesh, the results of temperature, equivalent stress, normal stress at X and Y axis and the shear stress at XY were taken for 3 different points (see figure 3.19):

- Point 1: point of maximum temperature;
- Point 2: point of maximum equivalent stress (Von Mises);

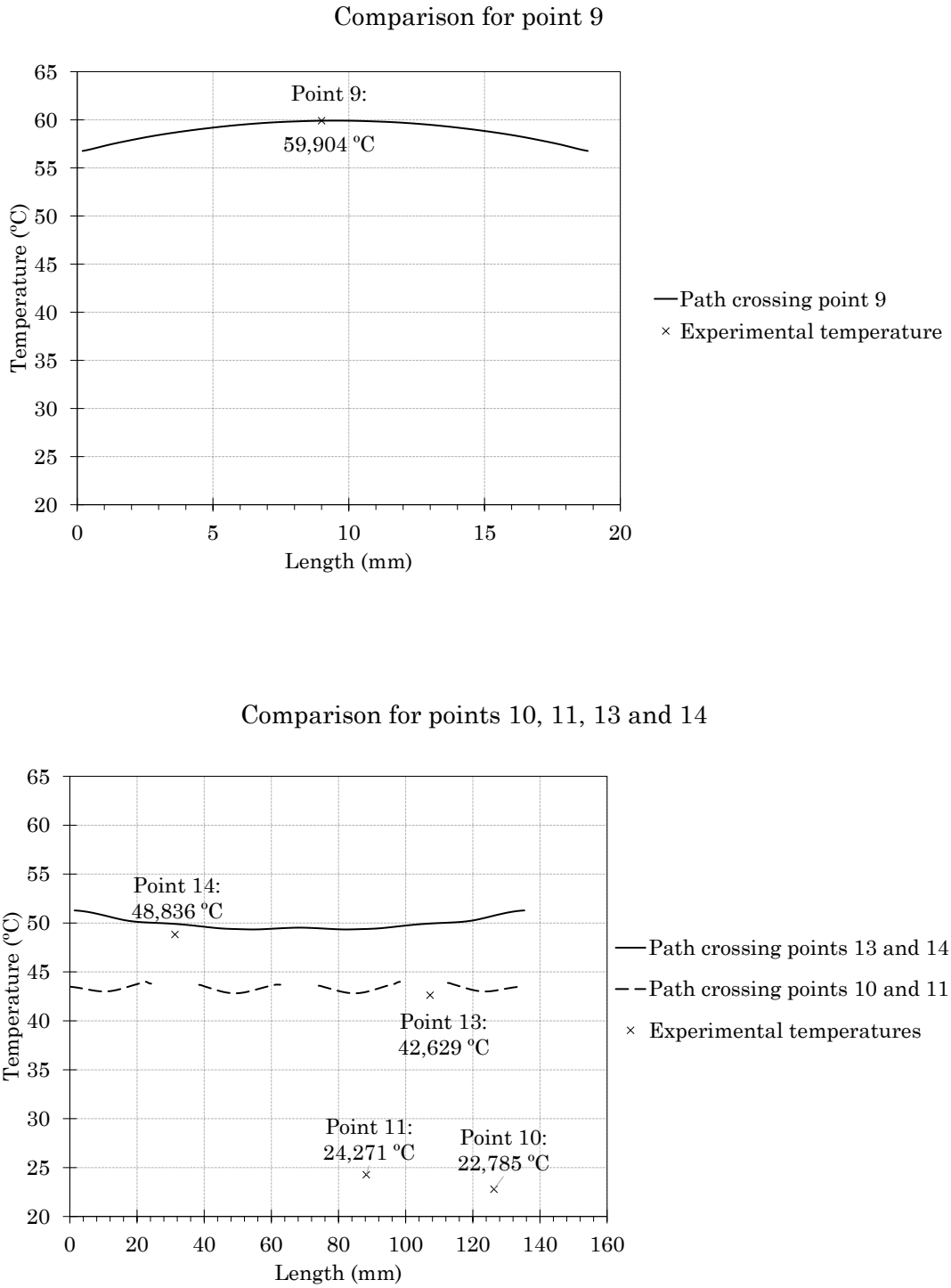

Figure 3.15: Difference between thermal simulation temperatures and experimental values.

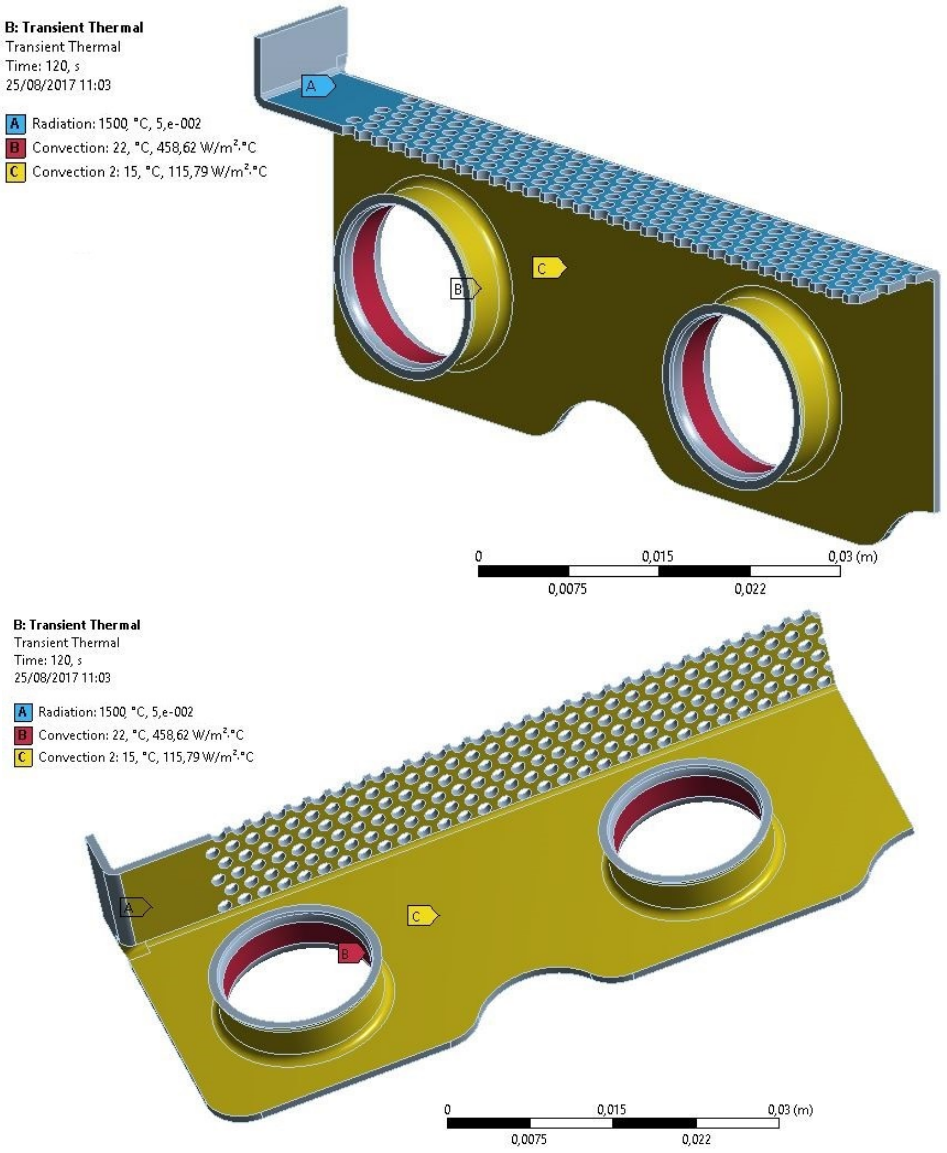

Figure 3.16: Thermal boundary conditions.

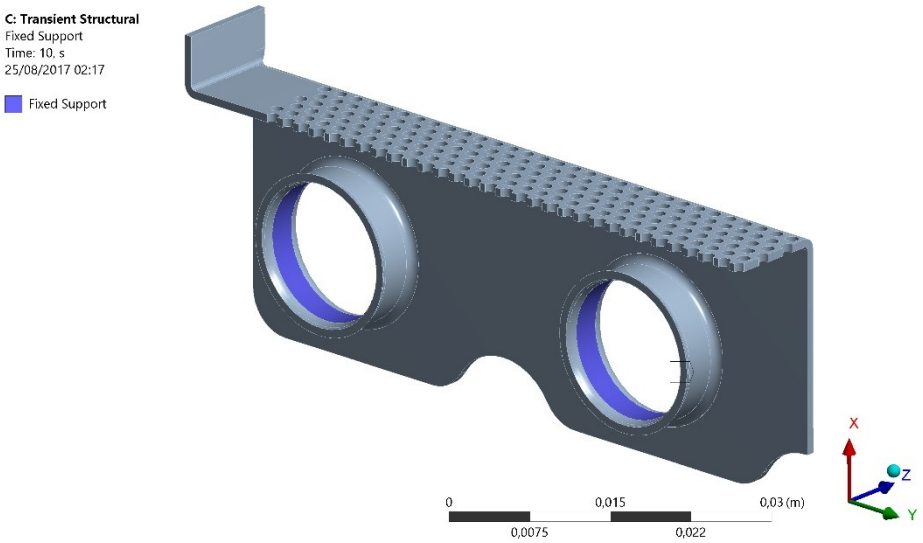

Figure 3.17: Fixed support on the copper tubes zone.

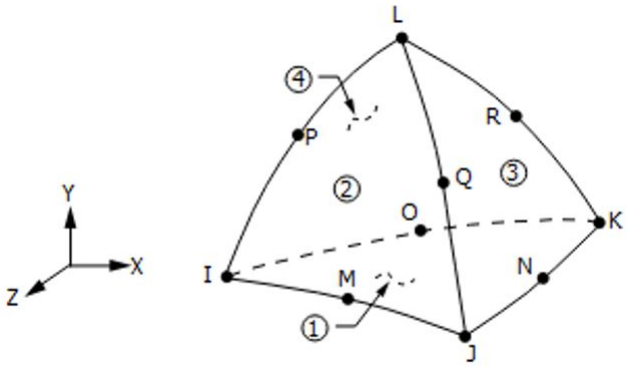

Figure 3.18: Element SOLID187 used in the thermomechanical simulation [12].

Table 3.9: Number of nodes and elements for each mesh and its analysis time.

	Mesh 1	Mesh 2	Mesh 3	Mesh 4	Mesh 5
Nodes	46603	81103	152981	184291	348308
Elements	24263	45331	77462	93903	203986
Analysis time (min)	7	18	46	305	1560

- Point 3: point 9 of experimental measurements.

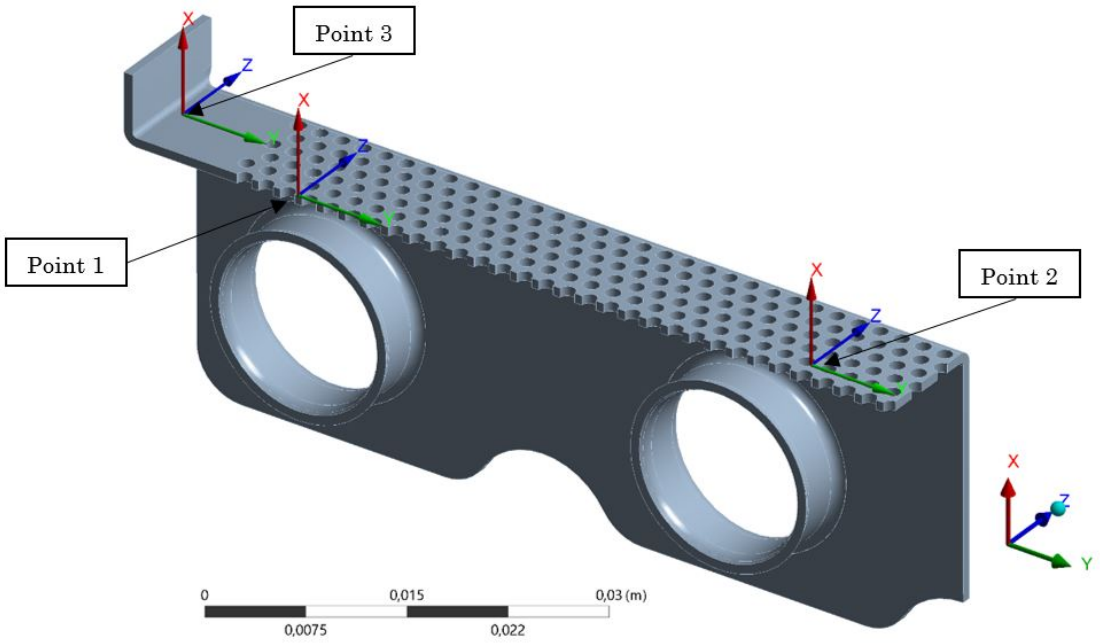

Figure 3.19: Location of the points under analysis (1, 2 and 3) in the geometry.

The results presented in figures 3.20 to 3.23 show that the convergence is not reached since stability is not achieved in figures 3.21 to 3.23. The temperature (see figure 3.20) seems to be the parameter less sensitive to the mesh since for each point its value remained the same from the first mesh to the last. Conversely, the equivalent stress (see figure 3.21) at point 2 has a higher dependence on the mesh, mostly due to the stresses at X and Y (see figures 3.22 and 3.23). The shear stress (figure 3.24) behaves the same way, in which the point 2 is more inconsistent. The different behaviors observed for the 3 points can be explained by the mesh refinement. Since the points coordinates remained the same for all the meshes, the location of the nodes may not coincide with the points. Therefore, as the results of each point are given by the result at the nearest node, the meshes with less refinement can give the result in a node farthest from the points coordinates.

Since the simulation with mesh 5 lasted 26 h (or 1560 min, see table 3.9) and taking into account the computational limit that is given by the software, it was not possible to conclude the mesh sensitivity study. Therefore, the mesh 3 was selected to proceed with the work (see figure 3.25).

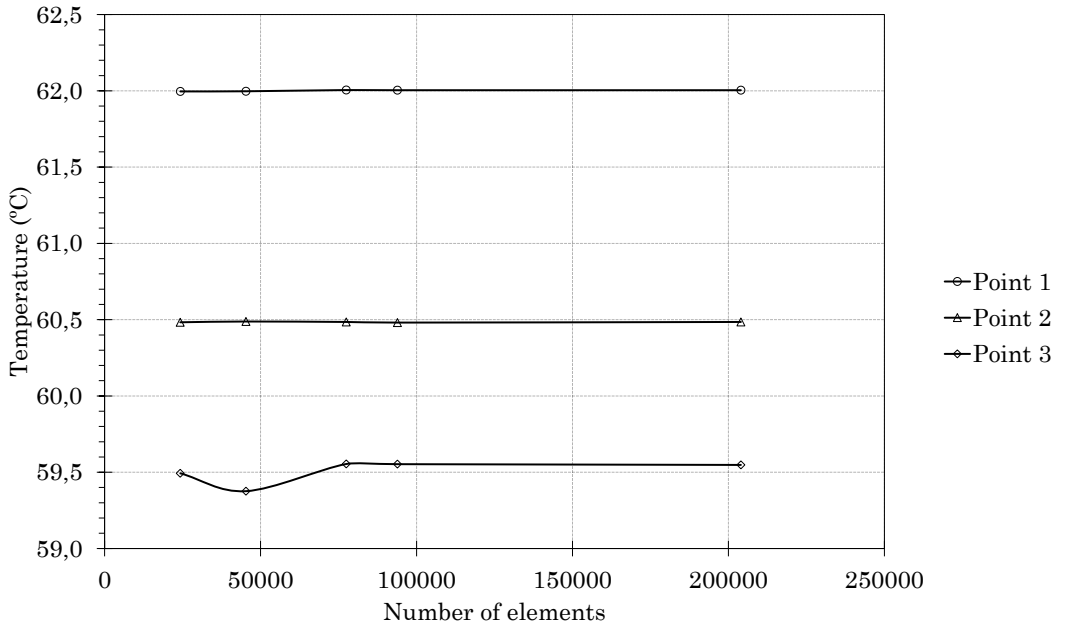

Figure 3.20: Temperature results for each point in the mesh sensitivity study.

3.6 Simulation Settings

The simulation was performed through a transient thermal and quasi-static structural systems, where it was intended to simulate a complete cycle of the burner surface, which basically consists of 1 min heating and 1 min cooling. Thus, the analysis was divided into several steps, as indicated in table 3.10, where the only heat source considered is radiation. Therefore, the following steps are considered:

1. The surface is at room temperature for 10 seconds;
2. The body is exposed to a radiation source of 1500°C for 50 seconds;
3. The heat source is removed and the temperature decreases to room temperature for 50 seconds returning to the initial conditions.

For the transient quasi-static structural analysis, the boundary conditions remain the same along the cycle.

3.7 Results

3.7.1 Temperature

The transient thermal results of temperature are shown in figures 3.26 and 3.27. The maximum value obtained is 61°C, being in agreement with the steady-state analysis, for

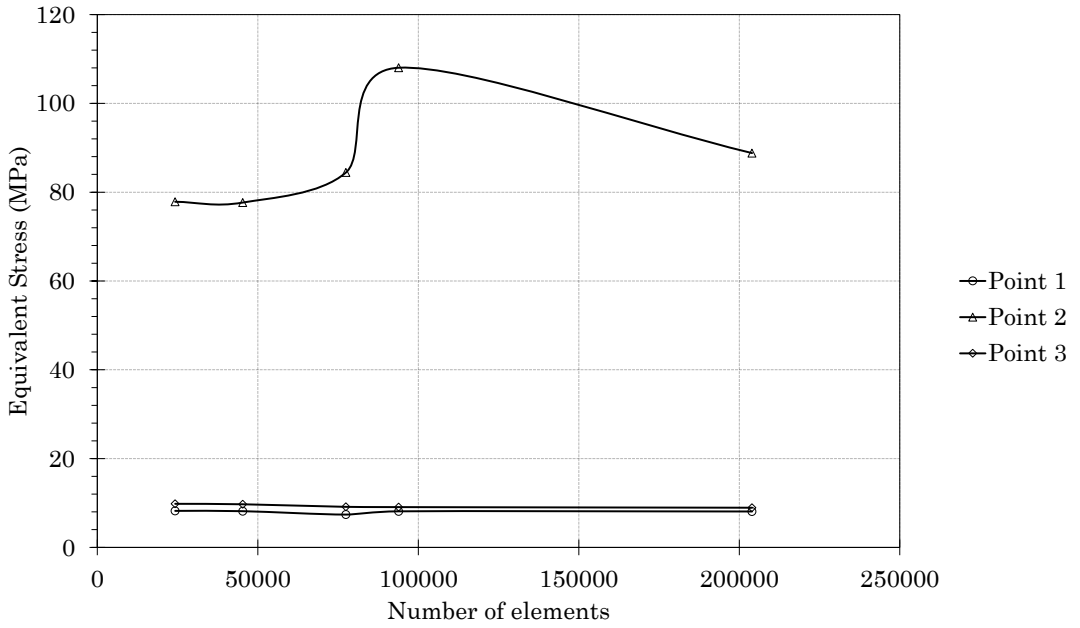

Figure 3.21: Equivalent stress results for each point in the mesh sensitivity study.

Table 3.10: Steps considerer in transient thermal analysis.

Steps	End step time (s)	Radiation temperature (°C)
0	0	22
1	10	1500
2	60	1500
3	70	22
4	120	22

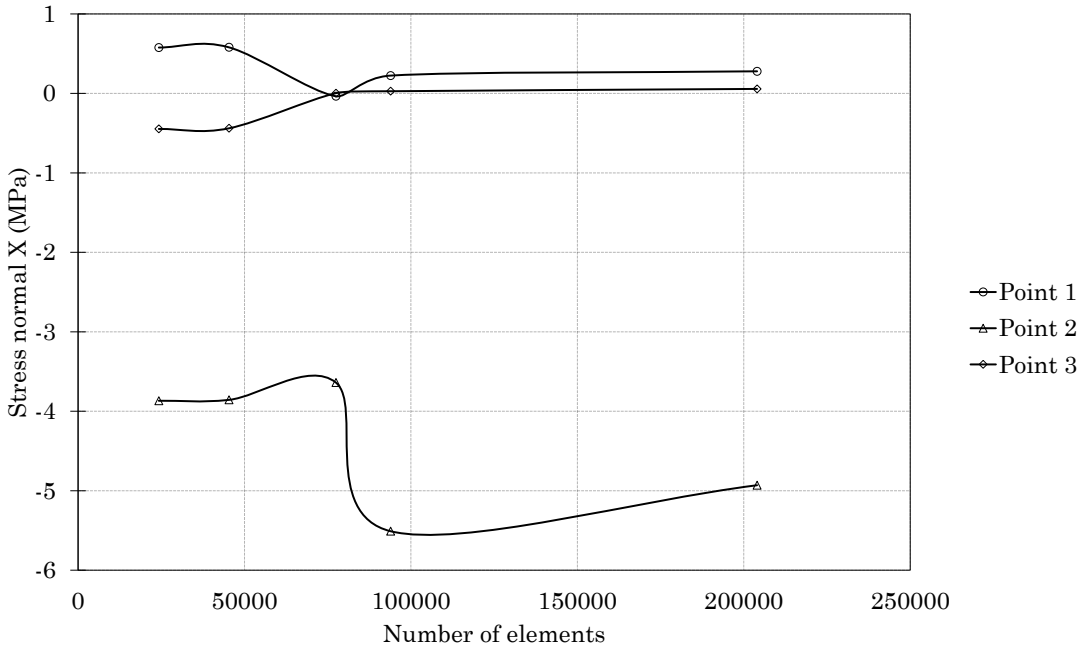

Figure 3.22: Results of stress σ_{xx} for each point in the mesh sensitivity study.

the maximum temperature of the plate (point 9 in figure 3.15).

The temperature distribution corresponds to the expected since the isolines are perpendicular to the heat flux, which mainly goes from the radiation heat source to the tube zones. As also expected, the maximum temperature occurs at the center of the perforated surface since it is directly exposed to the radiation temperature.

3.7.2 Stress

The obtained equivalent stress of Von Mises is represented in figures 3.28 and 3.29. The maximum stress occurs at the tube zones, with a value of 90,3 MPa for a time equal to 60 seconds. Since this zone is constrained, it can not expand thermally and therefore, it is expected to have higher stress levels. It is also a zone where the thermal gradients are high, which in turn causes an increase of the strain and consequently of the stress as well.

3.7.3 Strain and displacement

The maximum strain on the surface is 0,087%. The figure 3.30 shows the strain profile and its behavior over the time cycle.

The maximum displacement occurs at the center of the surface and has a value of 0,045 mm (see figure 3.31) which is not significant considering the general dimensions of the burner's surface.

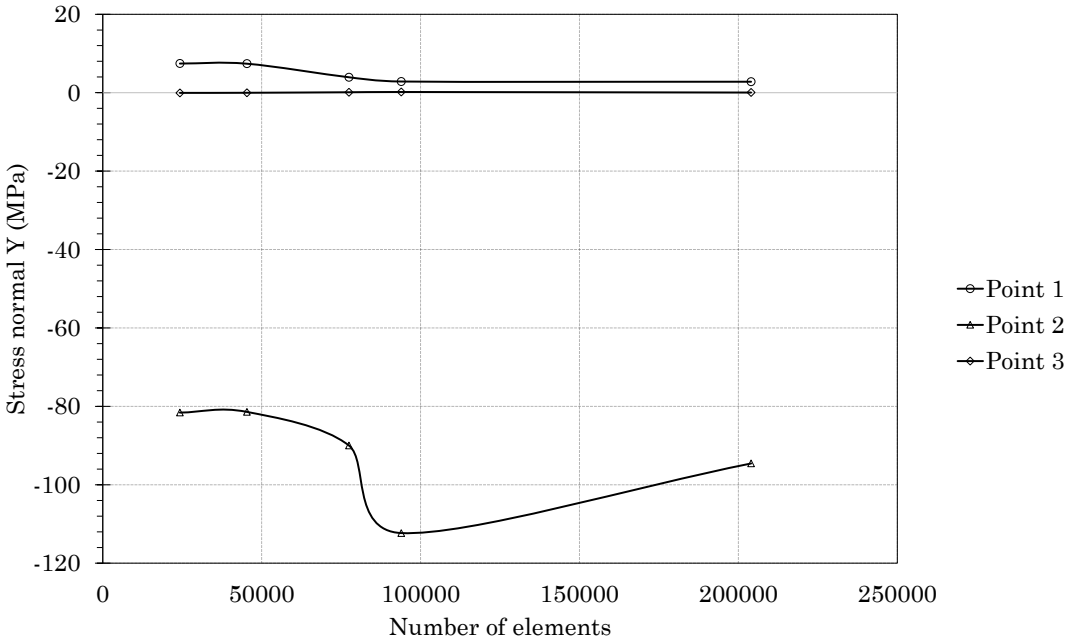

Figure 3.23: Results of stress σ_{yy} for each point in the mesh sensitivity study.

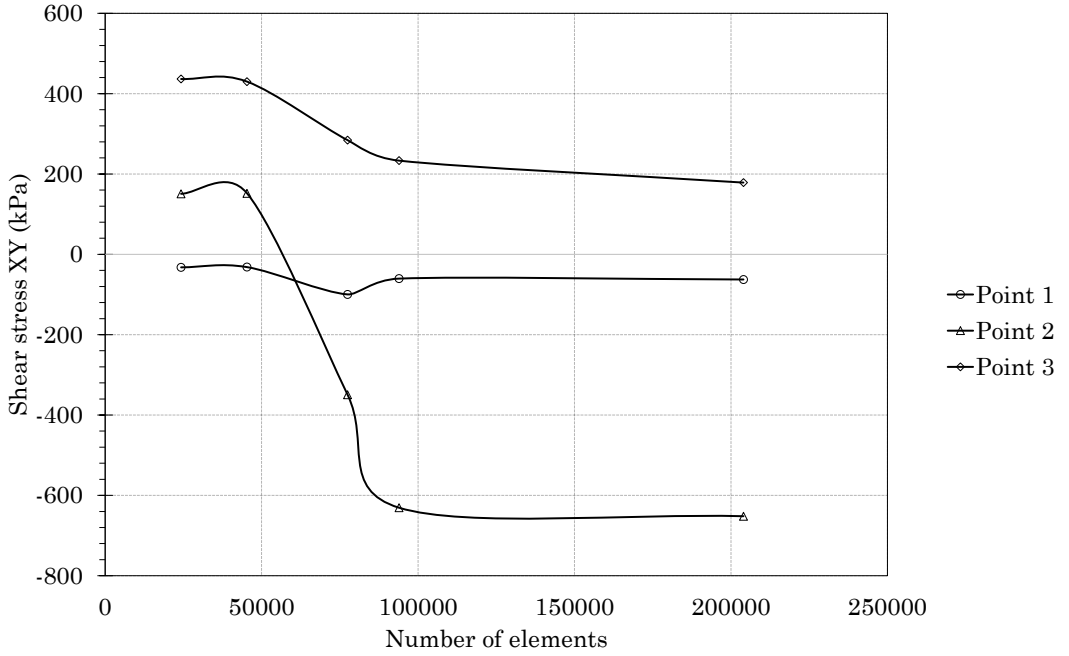

Figure 3.24: Results of shear stress τ_{xy} for each point in the mesh sensitivity study.

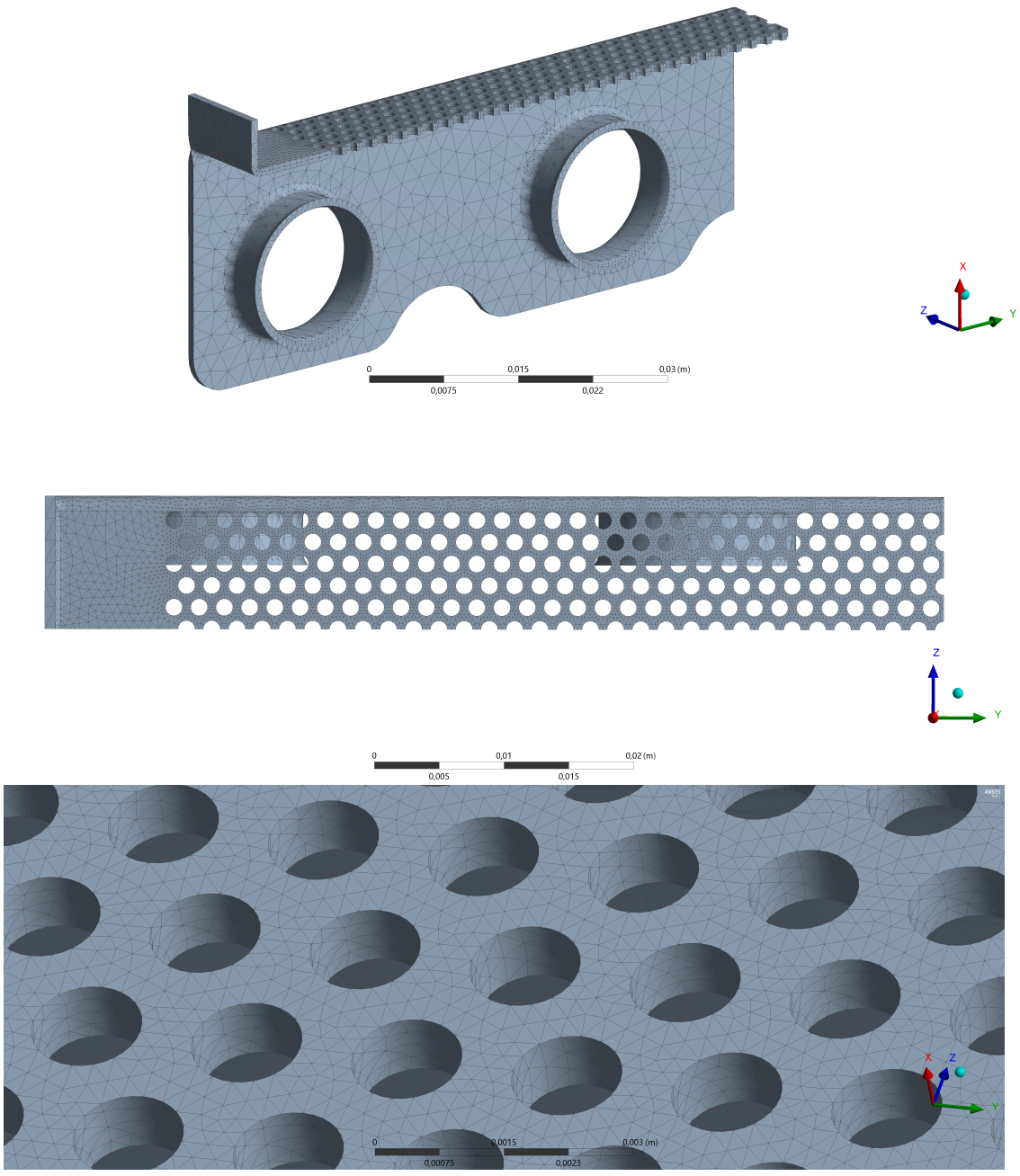

Figure 3.25: Selected mesh for the analysis.

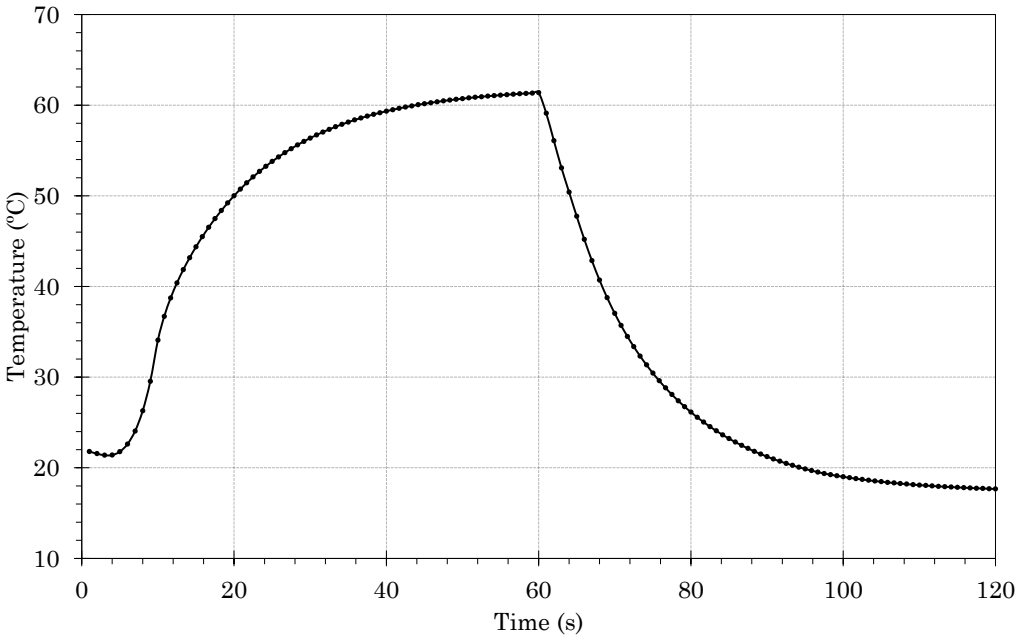

Figure 3.26: Maximum temperature over time at burner surface.

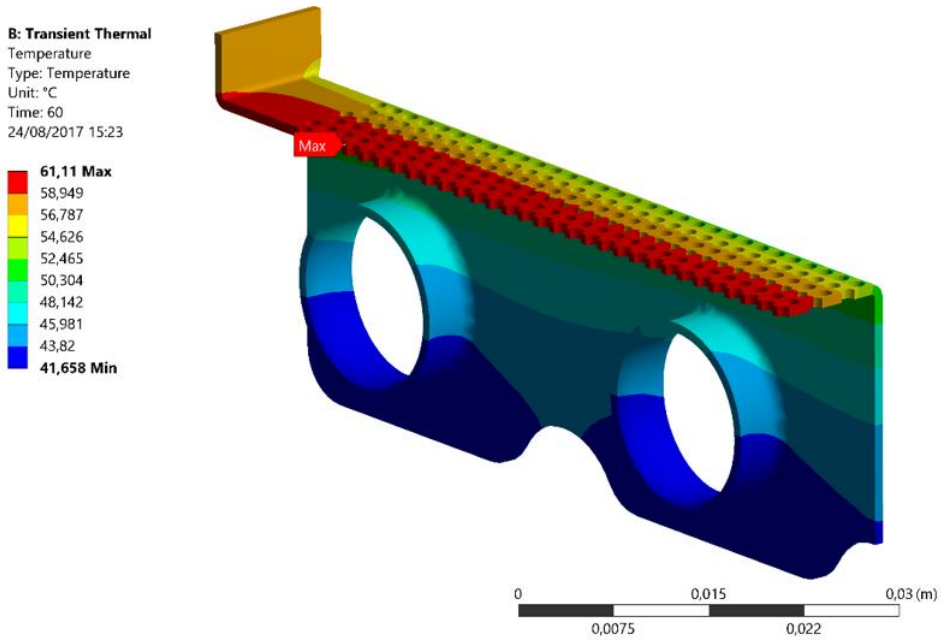

Figure 3.27: Temperature profile of burner's surface.

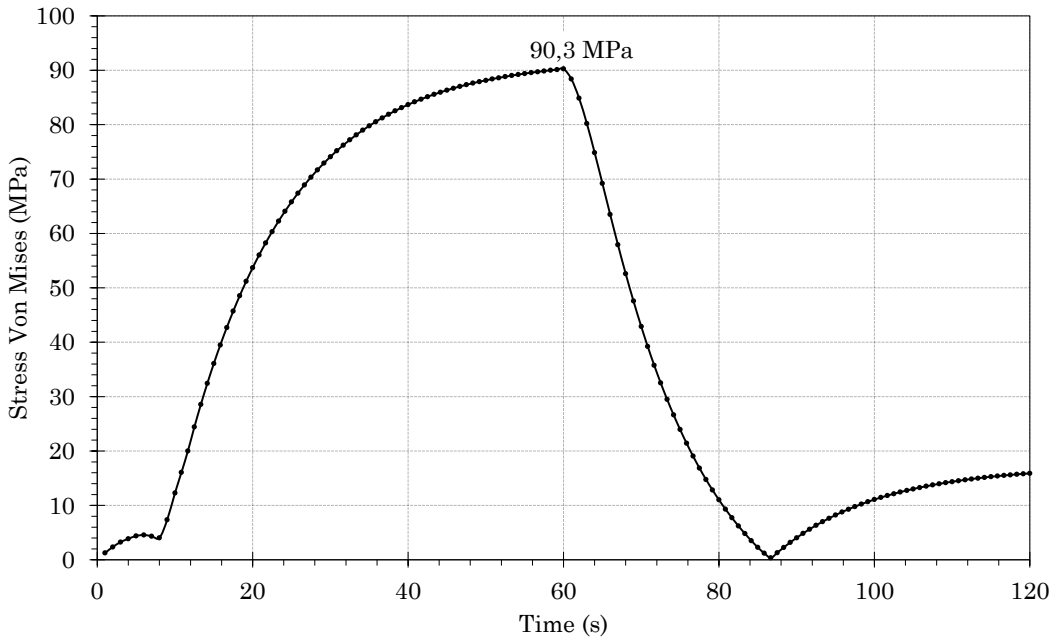

Figure 3.28: Maximum Von Mises stress over time.

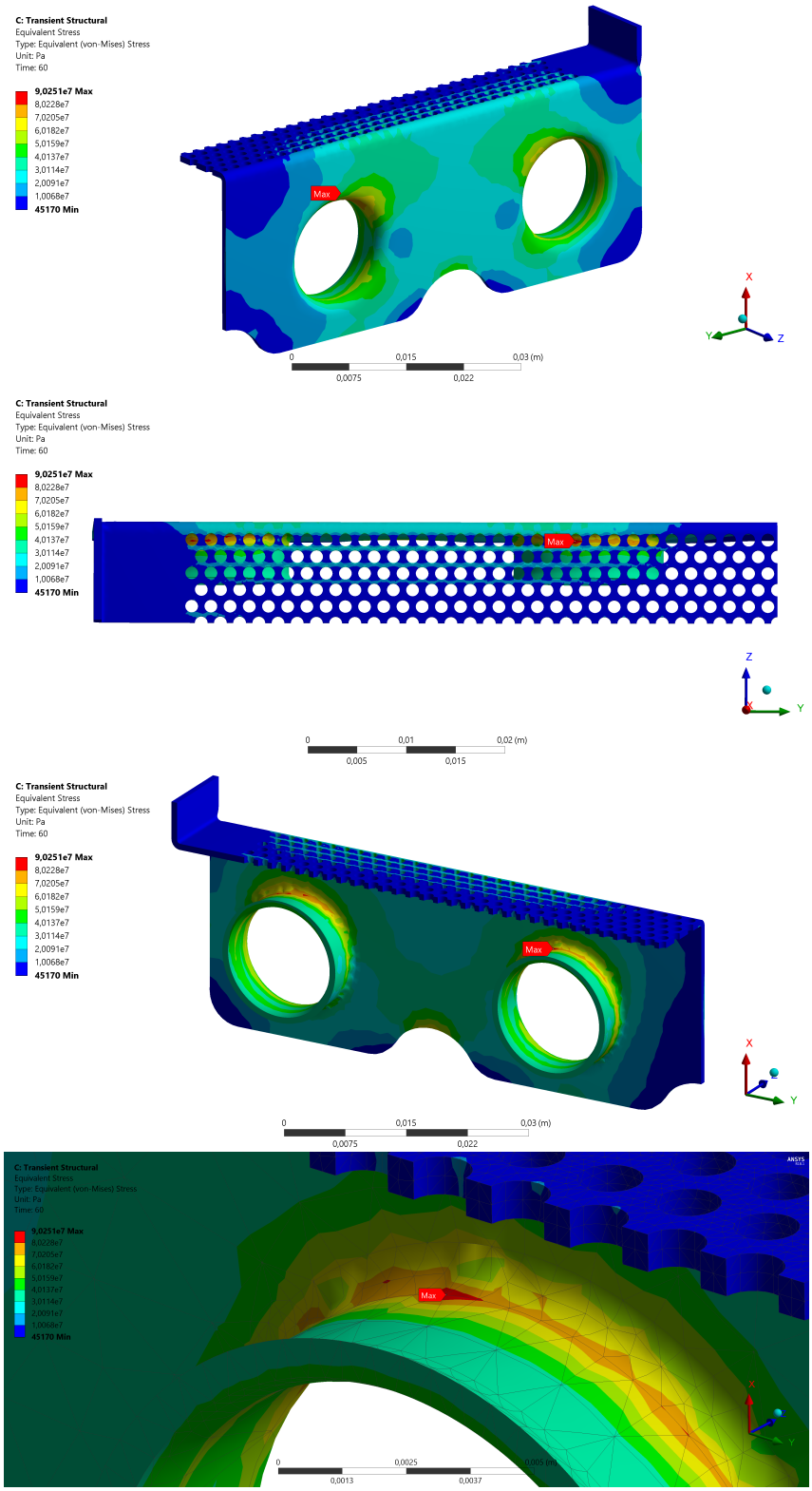

Figure 3.29: Results of equivalent stress (Von Mises) for 4 different views.

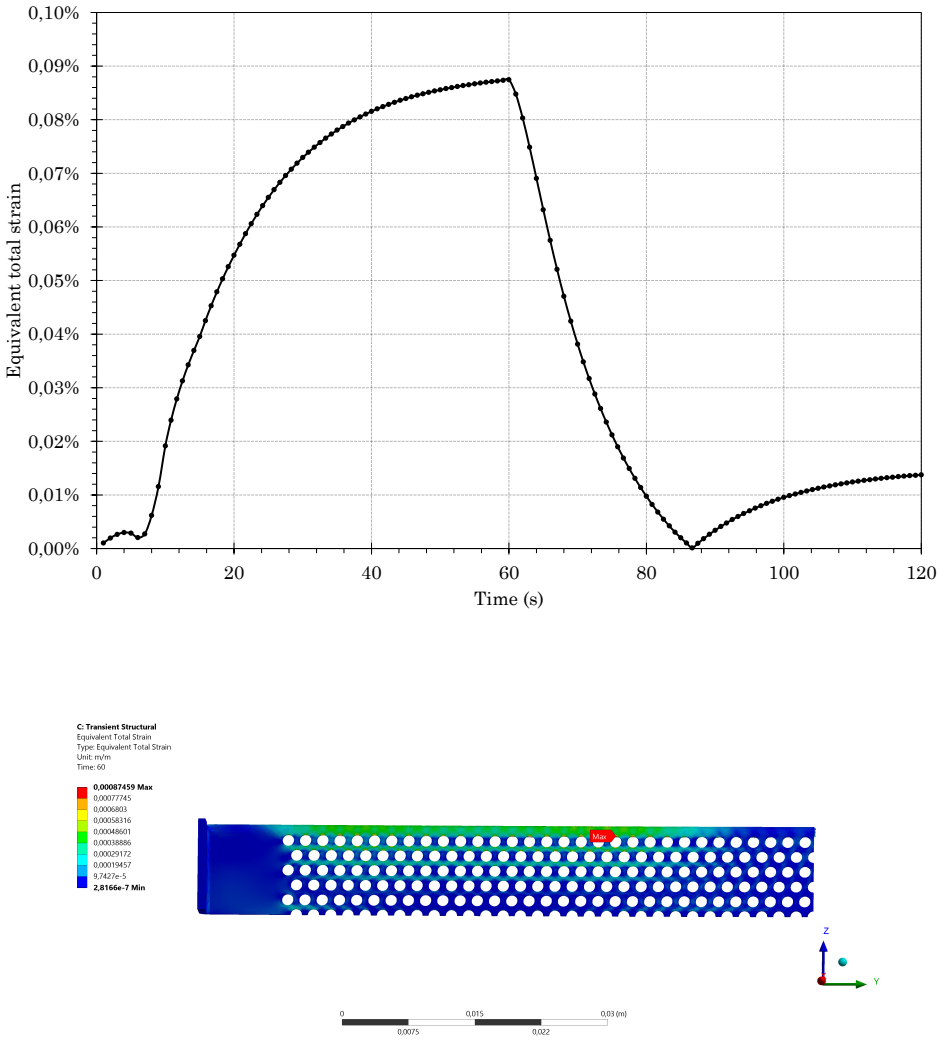

Figure 3.30: Strain results over the time.

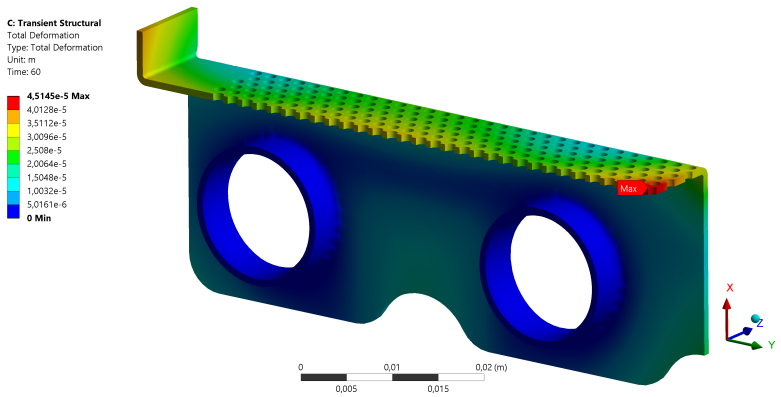

Figure 3.31: Displacement results over time.

Chapter 4

Life Prediction Methods

4.1 Life Prediction Methods

Life prediction methods, as presented in section 1.4, are a set of parametric methods, where the components life can be estimated, knowing the operating conditions such as temperature, stress and strain.

The analyses performed in chapter 3 led to the achievement of the temperature profile, the stresses and strain along the surface. Those results are used as inputs for the life prediction models.

First, the creep behavior is analyzed (section 4.1.1), then the fatigue behavior (section 4.1.2) and lastly the interaction between these two failure mechanisms (section 4.1.3).

4.1.1 Creep Life Prediction

For creep life prediction three different methods were considered. These are:

- the Larson Miller:

$$\mathrm{LMP} = \mathrm{T}(\log t + \mathrm{C}), \tag{4.1}$$

- the Manson and Haferd:

$$\mathrm{MHP} = \frac{\log t - \log t_A}{T - T_A} \text{ and} \tag{4.2}$$

- the Dorn and Sherby:

$$\mathrm{DSP} = t \exp -\frac{A}{T}, \tag{4.3}$$

which are explained in section 1.4.1.

To understand which method is the most appropriate for the material under analysis, a set of experimental creep rupture curves for AA1100-O was found in [2] and their critical values gathered in table 4.1. Since the parameters are time and temperature dependent, they can be calculated for each experimental point becoming associated with the corresponding values of stress. Plotting the parameter versus the stress, a function that directly relates these variables can be given by a trendline. Therefore, the closest correlation to the experimental data determines the parameter to choose.

Table 4.1: Creep rupture experimental data tests [2].

Temperature (°C)	Stress (MPa)	Rupture Time (h)	Elongation (%)	Min. creep rate (s^{-1})
93,33	55,16	50	75	$1,61 \times 10^{-6}$
	48,26	399	67	$1,92 \times 10^{-7}$
	44,82	1748	68	$3,33 \times 10^{-8}$
121,11	48,26	15	90	$5,56 \times 10^{-6}$
	37,92	642	67	$9,72 \times 10^{-8}$
135,00	37,92	144	56	$4,17 \times 10^{-7}$
148,890	48,26	0,9	81	$9,44 \times 10^{-5}$
	31,03	211	84	$3,33 \times 10^{-7}$
	27,58	2346	47	$2,22 \times 10^{-8}$
176,67	24,13	176	86	$1,56 \times 10^{-6}$
	27,58	53	85	$2,64 \times 10^{-7}$
	20,68	1229	65	$1,36 \times 10^{-6}$
190,56	20,68	295	84	$1,78 \times 10^{-8}$
204,44	24,13	23	92	$2,26 \times 10^{-7}$
	20,68	61	79	-
232,22	20,68	6,8	54	$3,67 \times 10^{-8}$
	10,34	2041	66	-
260,00	13,79	18	100	$1,86 \times 10^{-7}$
	10,34	238	80	-
	8,27	1795	81	-
287,78	10,34	30	78	$1,99 \times 10^{-8}$
	8,27	275	70	-
315,56	8,27	55	80	$1,82 \times 10^{-7}$

The plots are represented in figures 4.1, 4.2 and 4.3 which have the corresponding associated trendline.

The constants used for each model were found in [3], which are summarized in table 4.2. This way, the correlations obtained from the trendlines for each method are presented in table 4.3.

Table 4.2: Creep life prediction models and the corresponding constants [3].

Creep life prediction model	Material constants	Value
Larson-Miller	C	20
Manson-Haferd	T_A (°F)	-500
	$\log t_A$	21,66
Dorn-Sherby	A	44100

The R^2 value indicates that the LMP and MHP methods have a better fit with the experimental data. Considering that the LMP is the most used for aluminum alloys, this is the selected method for the creep life prediction analysis. Therefore, the LMP as function of stress becomes:

$$\sigma = 1690,2 \exp -4,23 \times 10^{-4} \times \text{LMP} \Leftrightarrow \text{LMP} = -2361,5 \ln \frac{\sigma}{1690,2}. \tag{4.4}$$

Replacing the LMP expression given by equation 4.1, the time to rupture can be

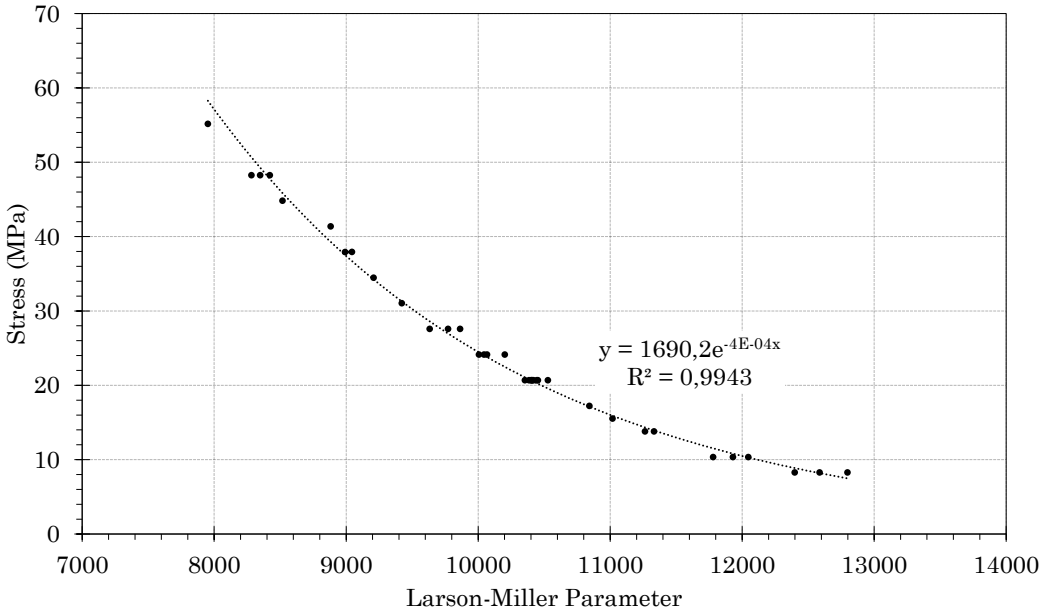

Figure 4.1: Correlation between LMP and the stress.

Table 4.3: Correlations between the stress and the parameters for creep life prediction.

Method	Equation	R^2
LMP	$\sigma = 1690,2\exp(-4 \times 10^{-4}\text{LMP})$	0,9943
DSP	$\sigma = -2,372\ln(\text{DSP}) - 68,824$	0,9836
MHP	$\sigma = 2013,9\exp(-0,101\ \text{MHP})$	0,9946

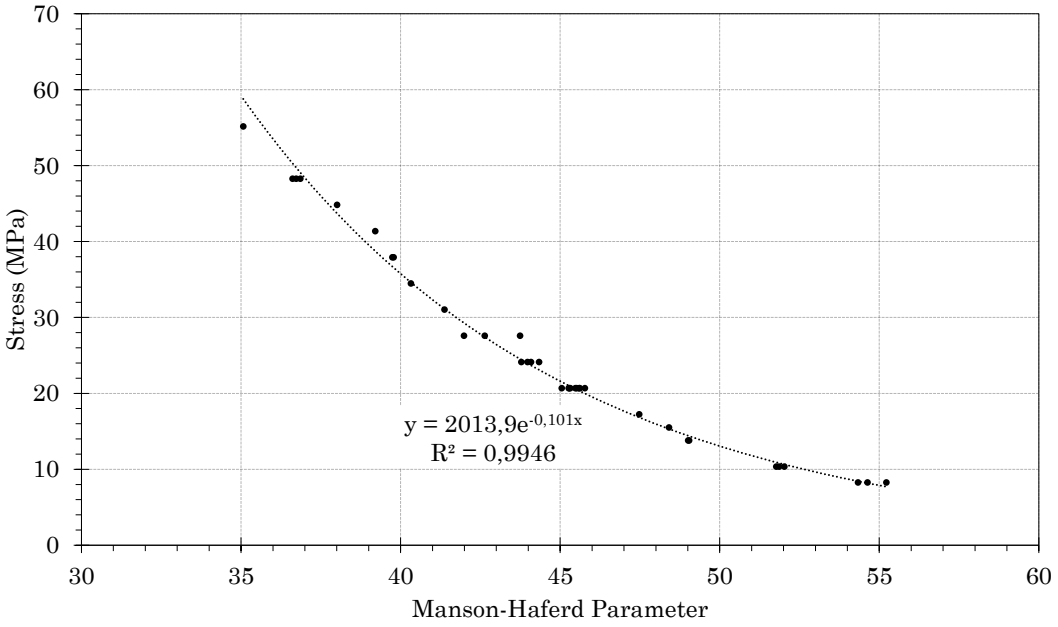

Figure 4.2: Correlation between MHP and the stress.

calculated by:

$$t_R = 10^{\left(\frac{-2361{,}498\ln\sigma+17552{,}08}{T}-20\right)} \tag{4.5}$$

Thus, knowing the stress (in MPa) and temperature (T in °C) at the surface, the time to rupture due to creep can be calculated. This equation is graphically represented in figure 4.4, where the time to rupture can be obtained directly from the temperature and stress values.

4.1.2 Fatigue Life Prediction

Fatigue life prediction consists of an estimation of the burner surface lifetime due only to fatigue behavior. This was achieved by a strain-based approach, explained in section 1.4.2.

In the current problem, in each cycle the stress goes from zero to the maximum value. Thus, the ratio R between the minimum and the maximum stress values is equal to zero. Therefore, since the R value is different than -1, the equation used in this section is

$$\varepsilon_a = \frac{\sigma'_f}{E}\left[2N_f\left(\frac{1-R}{2}\right)^{\frac{1-\gamma}{b}}\right]^b + \varepsilon'_f\left[2N_f\left(\frac{1-R}{2}\right)^{\frac{1-\gamma}{b}}\right]^c \tag{4.6}$$

where the material inputs $\sigma'_f, \varepsilon'_f, b, c$ represented in table 4.4 were obtained through a completely reversed cycle ($R = -1$) from Bosch Matis database. Figure 4.5 represents

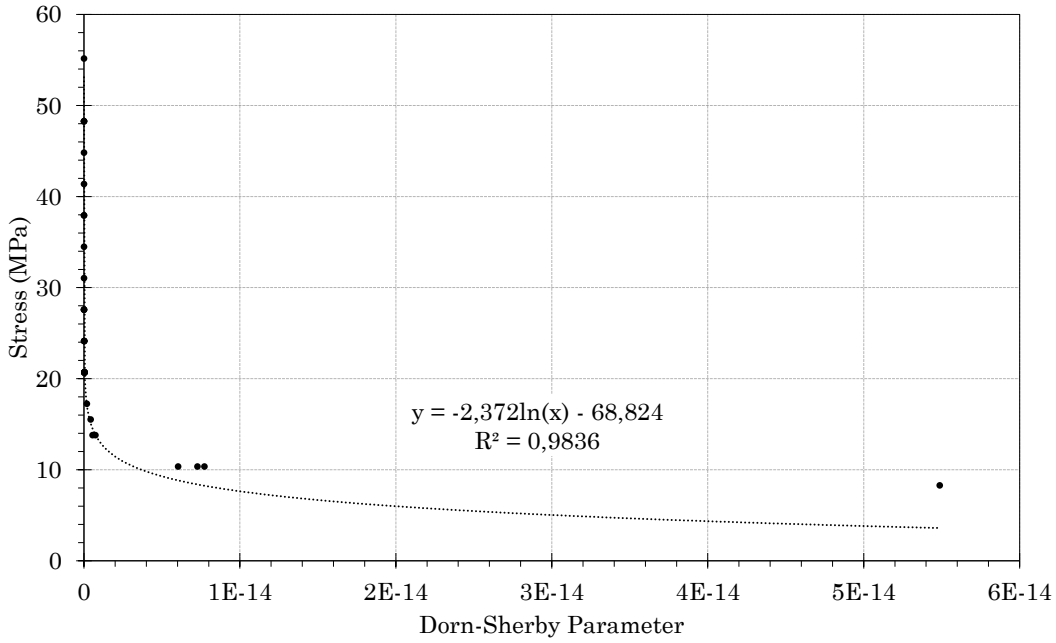

Figure 4.3: Correlation between DSP and the stress.

Table 4.4: Material inputs for fatigue analysis.

Cyclic Ductility Exponent c	Cyclic Ductility Coefficient ε'_f	Cyclic Fatigue Strength Coefficient σ'_f [MPa]	Cyclic Fatigue Strength Exponent b	Cyclic Hardening Exponent n′	Cyclic Hardening Coefficient K′ [MPa]
-0,489	0,193	114	-0,076	0,155	147

the experimental data from which the fatigue input parameters were obtained. It also shows the difference between the curve for $R = -1$ and $R = 0$. The γ value is 0,65 for the low stiffness aluminum alloys [41].

Replacing the value of table 4.4 in equation 4.6, the final equation is given by:

$$\varepsilon_a = 0,001652174\,(48,6802N_f)^{-0,0760} + 0,193\,(48,6802N_f)^{-0,489}\,, \tag{4.7}$$

where the number of cycles to failure is calculated only based on the strain values.

Note that ε represents the amplitude value of strain, the result given by the simulations must be divided by 2 since it represents the maximum value wherein the minimum is zero.

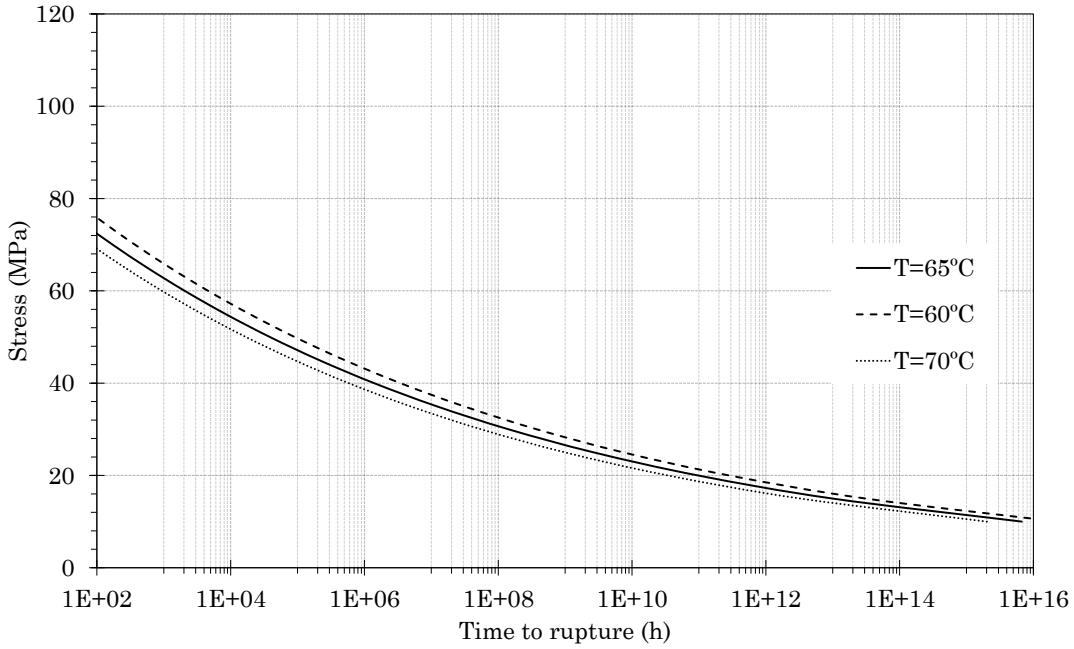

Figure 4.4: Graphic representation of equation 4.5.

4.1.3 Creep and Fatigue Life Prediction

The creep and fatigue behavior are combined by a linear summation of the creep and fatigue damage fractions:

$$D_{\text{total}} = D_{\text{c}} + D_{\text{f}}, \tag{4.8}$$

where both terms are calculated independently.

The creep damage is obtained through the Robinson's Life Fraction rule [28], represented by the quotient between the time spent (t_i) and the time to failure (t_{f_i}) under condition i:

$$D_{\text{creep}} = \sum \frac{t_i}{t_{f_i}}. \tag{4.9}$$

Thus, as creep behavior depends on temperature and stress, these are the conditions of index i. For a combination of these, the time to failure (t_{f_i}) is estimated by the LMP.

On the other hand, fatigue damage is achieved by the Miner's rule characterized by the quotient between the number of operating cycles (N_{cycles}) and the number of cycles to failure (N_f):

$$D_{\text{fatigue}} = \sum \frac{N_{\text{cycles}}}{N_f} \tag{4.10}$$

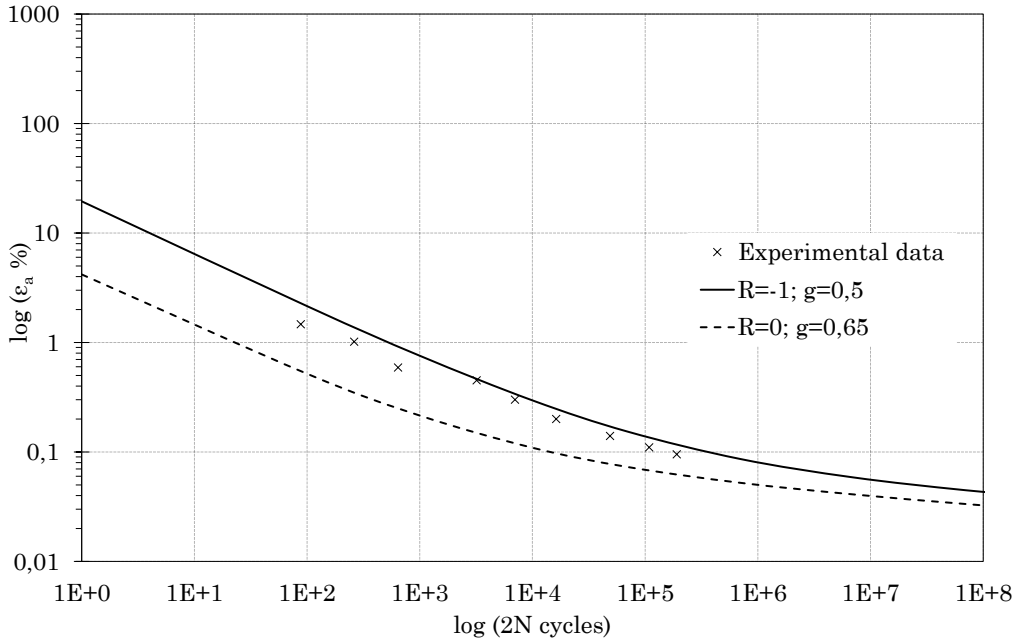

Figure 4.5: Strain life curve and the representation of the experimental data from fatigue tests.

As the current fatigue approach only depends on strain level, the N_f value is estimated using the figure 4.5, not forgetting that the strain amplitude corresponds to half of the maximum strain.

Therefore, the total damage is the sum of the creep and fatigue damages (equation 4.8) and the main objective is the calculation of t and N_{cycles} values for the material failure, that is, when the total damage (D_{total}) reaches the unit.

Through the simulation results (temperature, stress and strain), the values of t_f and N_f can easily be estimated. Thus, the unknowns are the t and N_{cycles}. Since there is only one equation, these values were related considering that 1 cycle is equivalent to 2 min, in which 1 min corresponds to the heating phase (gas combustion on) and the other minute corresponds to the cooling phase (gas combustion off). In this way, only the first minute in each cycle is considered in the creep behavior. Therefore,

$$t = N_{\text{cycles}}[\text{min}] = \frac{N_{\text{cycles}}}{60}[\text{h}]. \tag{4.11}$$

Additionally the calculation of the number of cycles to failure, considering both creep and fatigue behaviors becomes:

$$\frac{N_{\text{cycles}}}{60t_R} + \frac{N_{\text{cycles}}}{N_f} = 1. \tag{4.12}$$

The lifetime of the burner surface is not given by the result of equation 4.11 because the gas water heater isn't used continuously. For that reason, it is estimated by Bosch Thermotechnology that 100,000 cycles correspond to 15 years of operation. So, the burner's surface lifetime is calculated by the following expression:

$$t_{\text{lifetime}}[\text{years}] = N_{\text{cycles}}\frac{15}{100000}. \tag{4.13}$$

4.1.4 Results

The results of chapter 3 to use in this section were gathered in table 4.5. The lifetime calculation was made considering the worst case scenario, that is, using the maximum values of stress, strain and temperature on the perforated region.

Table 4.5: Results used for the life prediction analysis.

Result	Value
Maximum temperature (°C)	61,1
Maximum stress (MPa)	60,3
Maximum strain (m/m)	$8,74 \times 10^{-4}$

Figures 4.6 and 4.7 represent the previous results of stress and strain, which were extracted only for the element located in the perforated region. The maximum value of strain gives a strain amplitude of 0,0437 % which is the value used in the calculations.

The creep time to rupture (t_R) is calculated by replacing the values of stress and temperature in equation 4.5. The value found for t_R is 3546,26h.

For the fatigue, the number of cycles to failure (N_f) is obtained through the equation 4.7. For a strain value of 0,0437 %, the result is 1789978 cycles until material's failure.

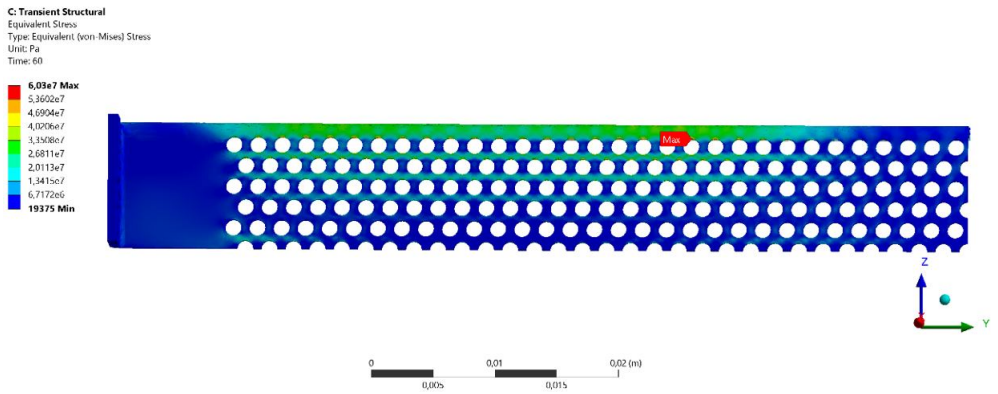

Figure 4.6: Equivalent stress in the perforated region.

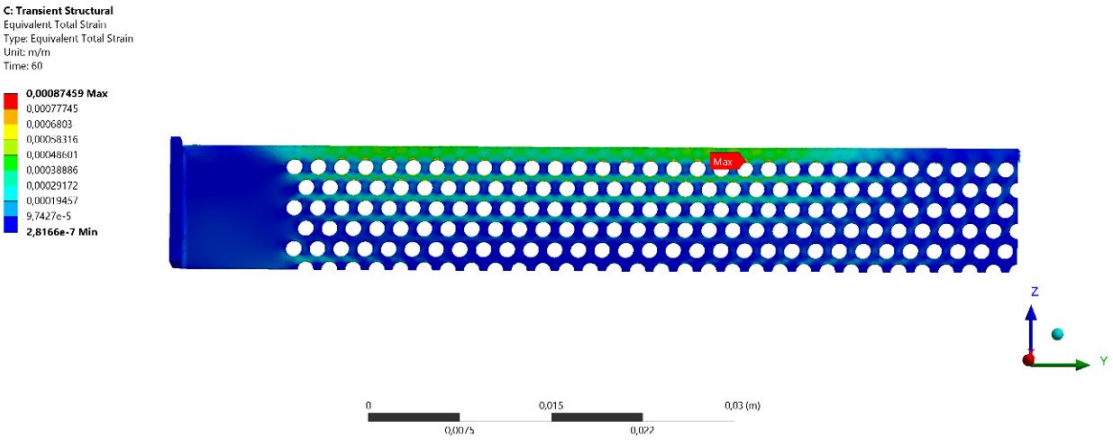

Figure 4.7: Total strain in the perforated region.

The number of cycles to failure due to simultaneously creep and fatigue is achieved through equation 4.12. Based on the previous results, the value of the number of cycles to failure is found to be 190170 cycles which corresponds to 3169,5 h.

Replacing the final value of cycles to failure, the damage fractions of creep and fatigue are, respectively:

$$D_{\text{creep}} = 0,894 \text{ and } D_{\text{fatigue}} = 0,106.$$

Figure 4.8 shows the creep and fatigue damage fractions for the total damage equal to 1 and also shows their location for 15 years of operation (100 000 cycles). For each, creep is the behavior which has more impact.

The lifetime result in years of operation (see equation 4.13) corresponds to approximately 28 years.

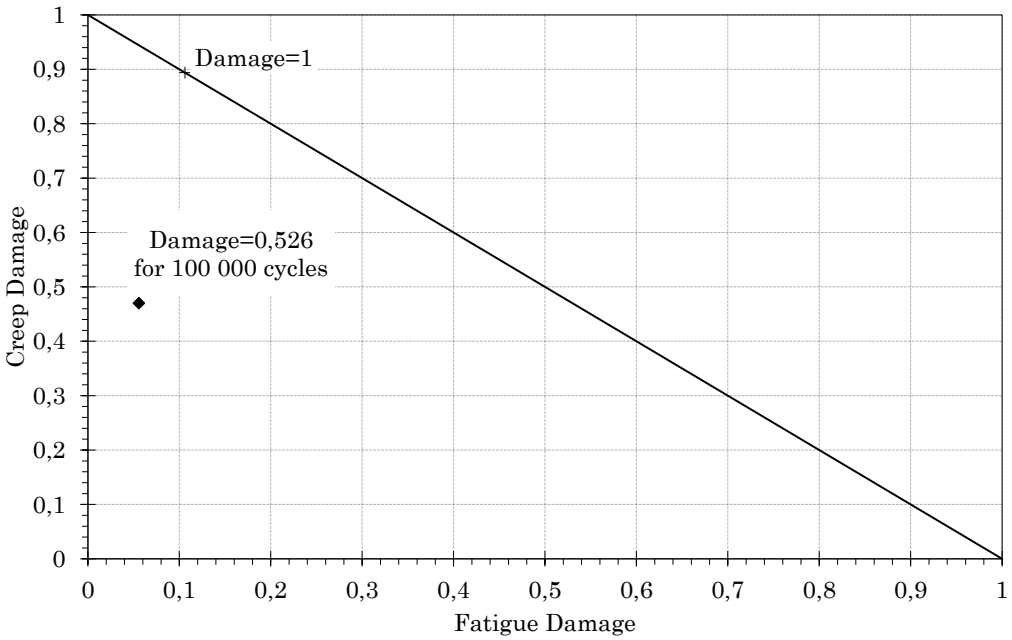

Figure 4.8: Creep and fatigue damage fractions for 100 000 and 190 170 cycles.

Chapter 5

Discussion and conclusions

In this chapter, the primary aim is to discuss and analyze crucial points of the current work, which can compromise all the results. Firtly, there are some aspects that worth highlighting:

- The results were obtained mainly by empirical relations, which always have an associated uncertainty.
- The lifetime results should be presented along with the geometry. But, for reasons of lack of software capabilities, that was not possible. Therefore, the result was obtained for the worst scenario, which corresponds to the point with the highest stress, strain and temperature.
- The operating conditions were considered constant, which in fact does not happen. The calculation process was performed considering a 11 l water heater equipment, continuously working at a flow rate of 5 l/min.
- The heating and cooling cycles also do not have the duration considered here, but the aim was to compare with the experimental results that are made at Bosch Thermotechnology, which consist of 1 min heating and 1 min cooling.

Furthermore, special emphasis is given to:

- the mesh quality,
- the boundary conditions and
- the results analysis, including the temperature and stress results.

5.1 Mesh Quality

The Element Quality criterion provides a quality metric that ranges between 0 and 1. This metric is based on the ratio of the volume to the average of the edge lengths for 3D elements. For tetrahedrons the expression is:

$$\text{Quality} = 124,7 \left[\frac{\text{Volume}}{\sqrt{\left[\sum (\text{Edge length})^2\right]^3}} \right]. \tag{5.1}$$

A value of 1 indicates a perfect cube while a value of 0 indicates that the element has a zero volume [50].

The element quality was analyzed and the results are presented in the figure 5.1. This parameter doesn't have an impact on the results since every mesh has good elements (0,95) and bad elements (<0,15).

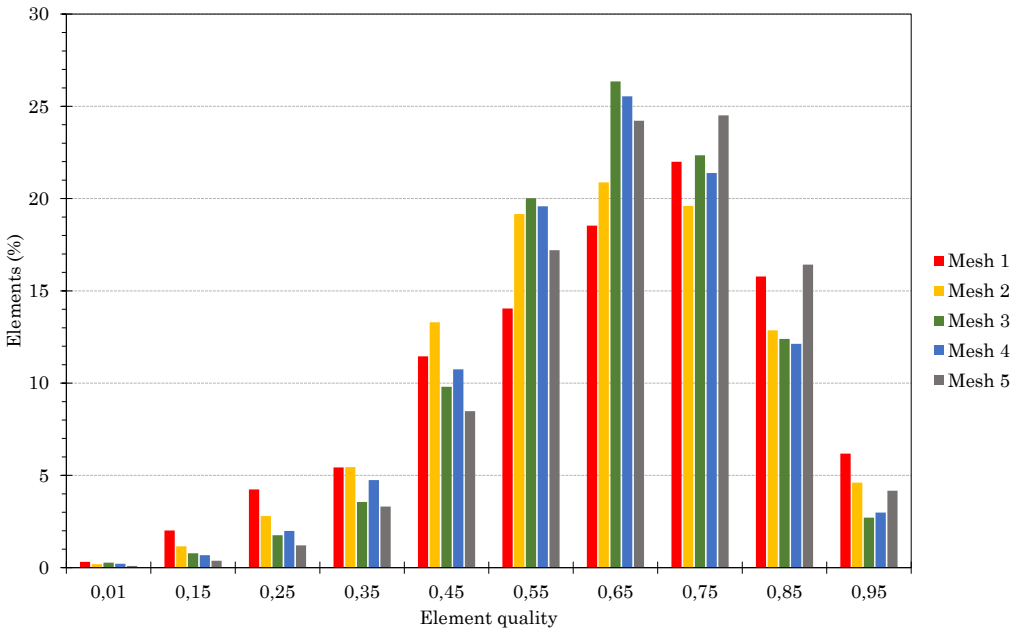

Figure 5.1: Element quality for each mesh.

5.2 Boundary Conditions Study

Although no boundary condition was considered on the lateral faces of the aluminum surface, the increase in temperature causes thermal expansion on that faces. If two adjacent plates are considered, one tends to expand towards to other and vice versa, annulling their expansion. Thus, in this line of thought, the displacement should be zero in the corresponding axis of expansion. Therefore, a boundary condition study was made in order to see the influence of the lateral faces displacement on the final result of stress. Therefore, three different cases were analyzed:

1. the case that consider any restriction on the lateral face (as assumed in section 3.4.2);
2. the case that consider zero displacement on axis Z;
3. consider an additional adjacent plate in the existing geometry, to understand which case (1 or 2) is closer to reality.

Table 5.1: Comparison of the maximum stress on the surface for each case.

Hypothesis	Max Equivalent Stress [MPa]	Error [%]
1	87,4	1
2	95,2	10
3	86,6	-

In each case, the mesh and the simulation settings remained the same.

Table 5.1 represents the maximum equivalent stress on the surface, for each case, and it's found that the hypothesis number 1 is the most closer to the case 3, where two plates are adjacent to one another. Thus, the assumption made in section 3.4.2 has no influence on the result.

5.3 Results analysis

Since the results obtained in chapter 3 can affect the lifetime result, special care about those parameters needs to be taken to avoid possible mistakes and wrong assumptions. Therefore, the results were analyzed as shown in the following sections.

5.3.1 Temperature

The maximum temperature reached at the surface (61°C) is analyzed since it seems to be very low compared to the radiation temperature to which is subject. Neglecting the heat losses, the maximum temperature at the surface ($T_{\max}$) can be estimated assuming that all the heat that comes from the radiation is transferred to the water pre-heating system. Thereby, as the water flow characteristics in the preheating circuit are known (see table 5.2), the heat transferred to the water can be correlated with the heat emitted by radiation.

Table 5.2: Characteristics of the water flow in preheating circuit.

Twater in (°C)	Twater out (°C)	$\dot{m}$ $l/\min$	c_p $\mathrm{Jkg^{-1}K^{-1}}$
14,13	9,820	5	4186

Thus, considering the equations of thermal energy for steady state flow and heat transfer by radiation [46]:

$$\dot{Q}_{\text{water}} = \dot{m} c_p \left(T_{\text{water}_{\text{in}}} - T_{\text{water}_{\text{out}}}\right) \Leftrightarrow$$
$$\Leftrightarrow \dot{Q}_{\text{water}} = \frac{5\text{L}}{\min} \times \frac{\min}{60\text{s}} \times \frac{10^{-3} m^3}{L} \times \frac{10^3 \text{kg}}{m^3} \times 4186 \frac{\text{J}}{\text{kgK}} \times (14,127 - 9,820)^\circ\text{C}$$
$$\Leftrightarrow \dot{Q}_{\text{water}} = 1500 \text{ W}$$

Therefore,

$$\varepsilon \sigma A_{\text{rad}} \left(T_{\text{rad}}^4 - T_{\max}^4\right) = 1500\text{W} \Leftrightarrow$$
$$\Leftrightarrow \varepsilon \times 5,67 \times 10^{-8} \times 0,0157 \left(T_{\text{rad}}^4 - T_{\max}^4\right) = 1500\text{W}$$

where $\sigma = 5,67 \times 10^{-8}$ $Wm^{-2}K^{-4}$ is the Stefan Boltzman's constant and $A_{rad} = 0,0157$ m^2 is the total area directly exposed to radiation (10 plates in parallel, as shown in figure A.3).

Since the most uncertain parameters are the emissivity and the radiation temperature, keeping the maximum temperature of the surface at 61°C, there are two hypotheses:

- The radiation temperature can be different than 1500°C;
- The emissivity can be different than 0,05.

These hypotheses are schematically shown in figure 5.2, which gives the values of emissivity and radiation temperature for several points maintaining the heat transfer value in 1500 W. If the radiation temperature is 1500°C, the emissivity value must be

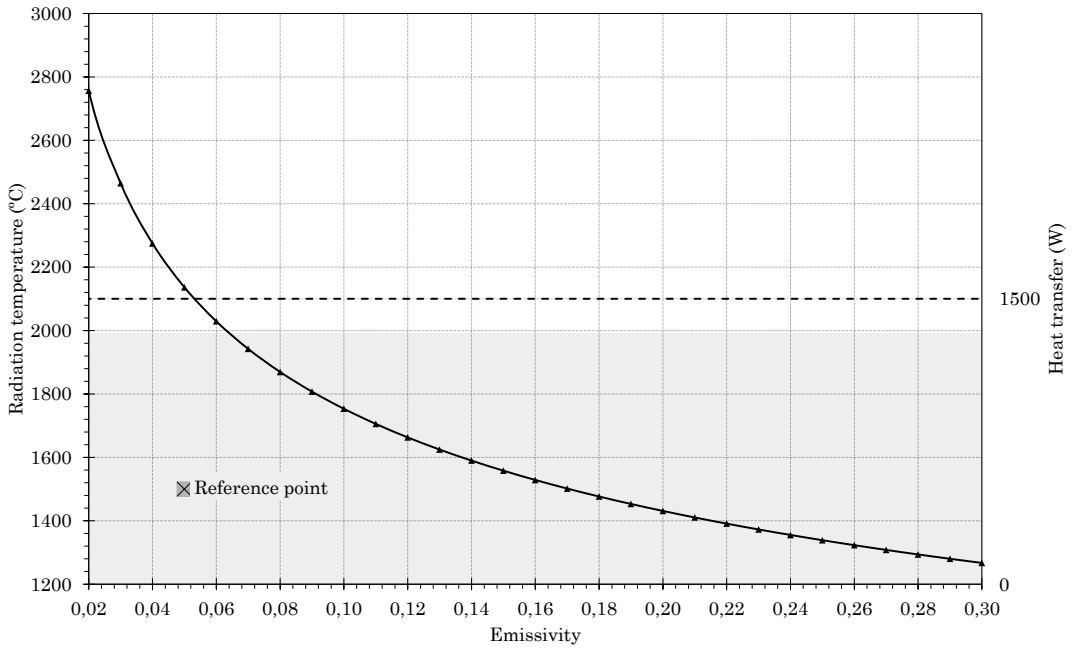

Figure 5.2: Relation between emissivity, radiation temperature and heat transfer.

0,17 to achieve the amount of energy of 1500 W. On the other hand, if the emissivity is 0,05, the radiation temperature must increase to 2136°C.

In order to understand if the range of these values is acceptable, the emissivity was analyzed and, as shown in table 5.3, depends on the material finishing and can range from 0,02 to 0,3.

On the other hand, in section 3.4.1 it was concluded that the radiation temperature should be in the range of 1200°C to 2000°C.

The combined ranges are represented by the shaded region in the figure 5.2. Therefore, as the reference point is within this region, it can be concluded that the maximum temperature in the surface, determined in chapter 3, is acceptable. However, if the

Table 5.3: Thermal emissivity for aluminum 1xxx series. Adapted from [4].

Thermal emissivity	Material
0,02-0,06	Pure aluminum (Al), polished, unoxidized
0,05	(1xxx series) Wrought commercially pure aluminum
0,1-0,3	Pure aluminum (Al), oxidized

maximum temperature on the surface was not measured correctly, the results can be compromised, since they are based on it.

5.3.2 Stress

The stress distribution is an important subject to analyze, since its value, such as temperature, can affect critically the final result. In section 3.7.2 it was concluded that the maximum stress value of 90,3 MPa occurs at the tube zones due to the constraint imposed on the circular faces. However, in the analysis of chapter 4, it was considered the maximum stress on the perforated region since it's where the maximum temperature is achieved. To understand if this assumption compromises the result, a histogram of the stress distribution for both hypothesis was made (see figure 5.3), where above each bar is represented the number of nodes. Note that for the complete geometry the stress results range from 0,01 MPa to 91 MPa and for the perforated region from 0,01 MPa to 60,3 MPa.

Since for the higher stresses, from 65 to 95 MPa, the sum of nodes is equal to 357 or 0,23% of the total nodes, this range is not significant compared to the overall results. Considering the results on the perforated region, in the highest range of stress (60 to 65 MPa), there is only one node. For that reason, the lifetime result, which was performed for the worst case (maximum stress), can be conservative.

5.3.3 Lifetime

The lifetime results are very dependent on the results of temperature, stress and strain. To understand how can this result varies, figure 5.4 shows a 3D plot which relates the temperature, the stress and the lifetime in years of operation for 3 different levels of strain.

5.4 Conclusions

The present work is dedicated to the lifetime prediction for the burner's surface of a gas water heater. The importance of the numerical simulations in applications such as this increases more and more, allowing to prevent future mechanical problems.

To simulate the burner surface behavior, Norton's creep model was used and its constants were fitted by an analytical and a numerical approach, which compared have a difference of 0,2% for the C_1, 3,34% for the C_2 and 9,87% for C_3. The difference between the numerical curves of both approaches and the experimental curves were quantified by a relative error which gives the difference between the areas under each curve. On average, the constants obtained through the numerical approach give better results, with an error of 9% compared to the experimental curves.

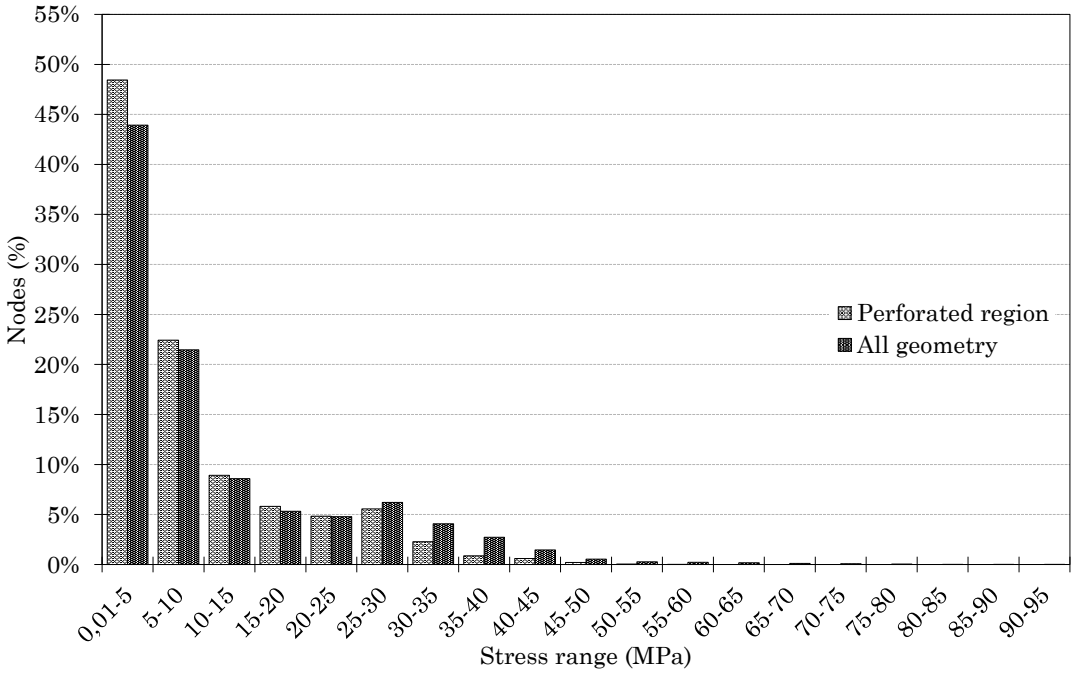

Figure 5.3: Histogram of the stress distribution in the perforated region and in all the geometry.

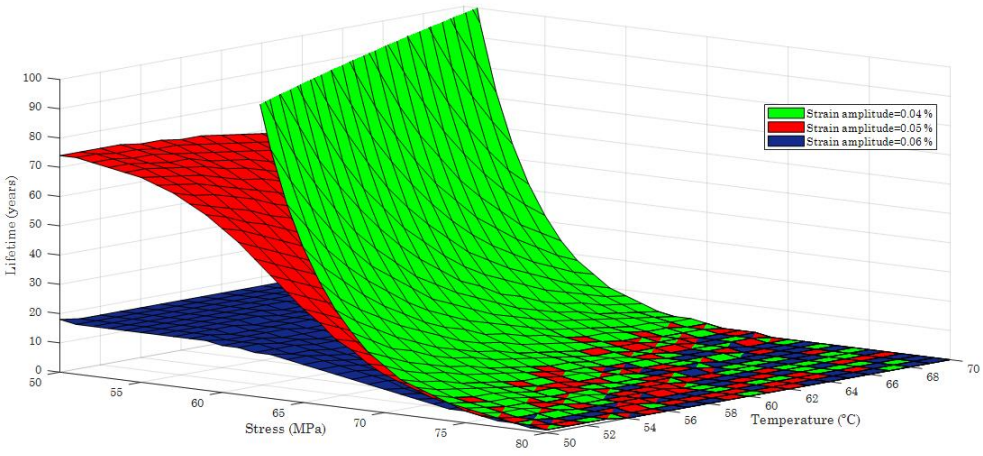

Figure 5.4: Lifetime as function of stress, temperature and strain.

The mesh was analyzed in order to ensure that it had no impact on the results. However, the study was not conclusive since the convergence was not reached due to the computational limit of the software. Therefore, the mesh with 77462 elements and 152981 nodes was selected to proceed with the work, since it required a shorter analysis time.

The maximum temperature of the plate is 61°C which is in agreement with the experimental temperatures. However, near the tube zones, this difference increases to 89% which represents about 20°C above the expected values.

The maximum stress of Von Mises occurs at the tube zones, with a value of 90,3 MPa. Since this zone is constrained, it can not expand thermally and therefore, it is expected to have the highest stress levels. The maximum strain on the surface is 0,087% and the maximum displacement occurs at the center of the surface and has a value of 0,045 mm which is not significant considering the general dimensions of the burner's surface. The lifetime of the burner surface was then estimated, considering the maximum value of temperature and the maximum values of stress and strain on the perforated zone.

To conclude, the estimated lifetime for the burner surface is 28 years, which despite being a conservative result, is quite acceptable considering that the equipment has to be dimensioned for at least 15 years of operation.

As future work, fatigue tests until rupture of the AA1050-H24 alloy should be done in order to obtain the number of cycles until the rupture of the material. Unlike the curves that were used, the tests should be performed for $R = 0$, that is, with the minimum strain equal to zero. Also, creep tests until rupture of the AA1050-H24 alloy should be done, to characterize not only the Larson-Miller curve more rigorously but also to define the parameters in the creep Norton's model. In this way, the lifetime prediction would be much more reliable.

Bibliography

[1] Akj Hasselström and Ue Nilsson. *Thermal Contact Conductance in Bolted Joints.* Diploma work in the master programme product development & applied mechanics, Chalmers University of Technology, 2012.

[2] David J.Wilson, James W. Freeman, and Howard R. Voorhees. Creep-rupture testing of aluminum alloys to 100,000 hours- Part I. Technical report, New York, 1969.

[3] J. Gilbert Kaufman. Theory and Application of Time-Temperature Parameters. In *Parametric Analyses of High-Temperature Data for Aluminum Alloys*, pages 3–21. ASM International, 2008.

[4] F. Cverna and A.S.M.I.M.P.D. Committee. ASM Ready Reference: Thermal properties of metals. In Fran Cverna, editor, *ASM Ready Reference Series*, page 527. ASM International, 2002.

[5] Bosch Thermotechnology. Esquentadores Vulcano, 2015.

[6] Marc André Meyers and Krishan Kumar Chawla. *Mechanical Behavior of Materials.* Prentice Hall, second edition, 2009.

[7] H. Altenbach and Jacek J. Skrzypek. *Creep and damage in materials and structures.* Springer- Verlag Wien, 1 edition, 1999.

[8] Run Zi Wang, Xian Cheng Zhang, Jian Guo Gong, Xu Min Zhu, Shan Tung Tu, and Cheng Cheng Zhang. Creep-fatigue life prediction and interaction diagram in nickel-based GH4169 superalloy at 650 Â°C based on cycle-by-cycle concept. *International Journal of Fatigue*, 97:114–123, 2017.

[9] Yukio Takahashi, Hiroshi Shibamoto, and Kazuhiko Inoue. Study on creep-fatigue life prediction methods for low-carbon nitrogen-controlled 316 stainless steel (316FR). *Nuclear Engineering and Design*, 238(2):322–335, 2008.

[10] Norman E. Dowling. *Mechanical Behavior of Materials.* Prentice Hall, New Jersey, second edition, 1999.

[11] Jr. Charles E. Baukal. *Heat Transfer in Industrial Combustion.* CRC Press, 2000.

[12] ANSYS. ANSYS Mechanical APDL Theory Reference. *ANSYS Inc*, Release15(November):1 – 909, 2013.

[13] Andre Almeida TT-DW ENG1.1. BlueOcean OF Low NOx burner. Technical report, 2016.

[14] Josef Betten. *Creep Mechanics*. Springer, 2 edition, 2005.

[15] Ernesto (Rensselaer) Gutierrez-Miravete. Chapter 9 Creep, 2005.

[16] Konstantin Naumenko and H. Altenbach. Modeling of Creep for Structural Analysis. In *Foundations of Engineering Mechanics*. Springer, 2014.

[17] R.L. Coble. J.Appl.Phys. 34:1679, 1963.

[18] F.R Nabarro. Deformation of Crystals by the Motion of Single Ions. In *Report of a Conference on Strength of Solids*, page 75, London, 1948. Physical Society.

[19] J. Harper and J.E. Dorn. Acta Met. *Acta Met*, 5:654, 1957.

[20] J. Lemaitre and R. Desmorat. *Engineering Damage Mechanics*. Springer, 2005.

[21] A. S. Krausz and K. Krausz. *Unified constitutive laws of plastic deformation*. Academic Press, 1996.

[22] PP Benham, RJ Crawford, and CG Armstrong. *Mechanics of Engineering Materials*. Longman, 2nd edition, 1996.

[23] Robert Minichmayr, Martin Riedler, Gerhard Winter, Heinz Leitner, and Wilfried Eichlseder. Thermo-mechanical fatigue life assessment of aluminium components using the damage rate model of Sehitogl. *International Journal of Fatigue 30*, 2008.

[24] Zakaria Abdallah, Veronica Gray, Mark Whittaker, and Karen Perkins. A Critical Analysis of the Conventionally Employed Creep Lifing Methods. pages 3371–3398, 2014.

[25] Calvin M Stewart. *A hybrid constitutive model for creep, fatigue, and creep-fatigue damage*. PhD thesis, University of Central Florida, 2013.

[26] Tarun Goswami. Development of generic creep fatigue life prediction models. *Materials & Design*, 25(4):277–288, 2004.

[27] Fujio Abe, Torsten-Ulf Kern, and R. Viswanathan. *Creep-resistant steels*. Woodhead Publishing Limited, Cambridge, 1st edition, 2008.

[28] Knowles, D. M., and MacLachlan. The effect of material behaviour on the analysis of single crystal turbine blades: material model development. *Current Applied Physics*, 4:300–303, 2004.

[29] De Guang Shang, Guo Qin Sun, Chu Liang Yan, Jian Hua Chen, and Neng Cai. Creep-fatigue life prediction under fully-reversed multiaxial loading at high temperatures. *International Journal of Fatigue*, 29(4):705–712, 2007.

[30] Samir Eshati. An evaluation of operation and creep life of stationary gas turbine engine. pages 2011–2012, 2012.

[31] E Kandare, S Feih, B Y Lattimer, and A P Mouritz. Larson Miller Failure Modeling of Aluminum in Fire. 41(December):3091–3099, 2010.

[32] S.S. Manson and A.M. Haferd. A Linear Time-Temperature Relation for Extrapolation of Creep and Stress-Rupture Data, 1943.

[33] F.R. Larson and J. Miller. A time-Temperature Relationship for Rupture and Creep Stresses. *Trans. ASME*, 74:765–771, 1952.

[34] S.S. Manson. Design Considerations for Long Life at Elevated Temperatures. Technical report, NASA, 1963.

[35] O.D. Sherby and J.E. Dorn. Creep Correlations in Alpha Solid Solutions of Aluminum. *Trans. AIME*, 194, 1952.

[36] Veselin Tsonev and Nikolay Nikolov. Defining the larson-miler parameter for a new alloy steel. 11(1):50–53, 2010.

[37] Levi De Oliveira Bueno. Hot Tensile and Creep Rupture Data Extrapolation on 2.25Cr-1Mo Steel Using the CDM Penny-kachanov Methodology. 17(2):518–526, 2014.

[38] L.F. Coffin. Fatigue at High Temperature, 1973.

[39] Norman E Dowling. Mean Stress Effects in Stress-Life and Strain-Life Fatigue. *2nd SAE Brasil International Conference on Fatigue*, 2004.

[40] A. Ince and G. Glinka. A modification of Morrow and Smith-Watson-Topper mean stress correction models. *Fatigue and Fracture of Engineering Materials and Structures*, 34(11):854–867, 2011.

[41] N. E. Dowling, C. A. Calhoun, and A. Arcari. Mean stress effects in stress-life fatigue and the Walker equation. *Fatigue and Fracture of Engineering Materials and Structures*, 32(3):163–179, 2009.

[42] Stuart B. Brown, Kwon H. Kim, and Lallit Anand. *An Internal Variable Constitutive Model For Hot Working of Metals*. PhD thesis, Massachusetts Institute of Technology, 1987.

[43] Yu Qiang Jiang, Y. C. Lin, C. Phaniraj, Yu Chi Xia, and Hua Min Zhou. Creep and creep-rupture behavior of 2124-T851 aluminum alloy. *High Temperature Materials and Processes*, 32(6):533–540, 2013.

[44] Donghuan Liu, Haisheng Li, and Yinghua Liu. Numerical simulation of creep damage and life prediction of superalloy turbine blade. *Mathematical Problems in Engineering*, 2015(Article ID 732502):10, 2015.

[45] A Andrade-Campos, L F Menezes, and F Teixeira-Dias. Large deformation processes on AA1050-O aluminium at elevated temperatures. *Advanced Materials Forum II: proceedings of the II International Materials Symposium: Materials 2003 and XI Encontro Sociedade Portugesa de Materials, 2003 Materiais*, 455-456(Generic):723–727, 2004.

[46] Frank P Incropera, David P DeWitt, Theodore L Bergman, and Adrienne S Lavine. *Fundamentals of Heat and Mass Transfer*, volume 6th of *Dekker Mechanical Engineering*. John Wiley & Sons, 2007.

[47] Rolf Sandström and Josefin Hallgren. Stress strain flow curves for Cu-OFP. Technical Report April, Royal Institute of Technology (KTH), 2009.

[48] S Song and M M Yovanovich. Explicit Relative Contact Pressure Expression: Dependence upon Surface Roughness Parameters and Vickers Mcirohardness Coefficients. Technical report, Department of Mechanical Engineering, University of Waterloo, Waterloo, Ontario, 1987.

[49] M. R. Sridhar and M.M. Yovanovich. Review of elastic and plastic contact conductance models - Comparison with experiment. *Journal of Thermophysics and Heat Transfer*, 8(4):633–640, 1994.

[50] ANSYS. Meshing User's Guide, 2017.

Appendix A

A.1 Confidential information

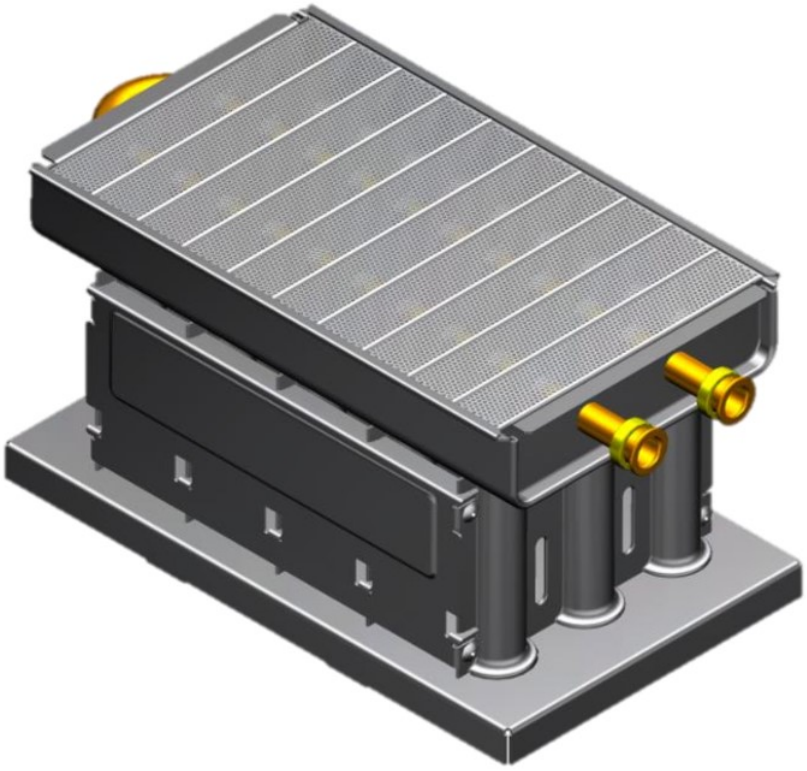

Figure A.1: BlueOcean burner OF Low NOx (extracted from [13]).

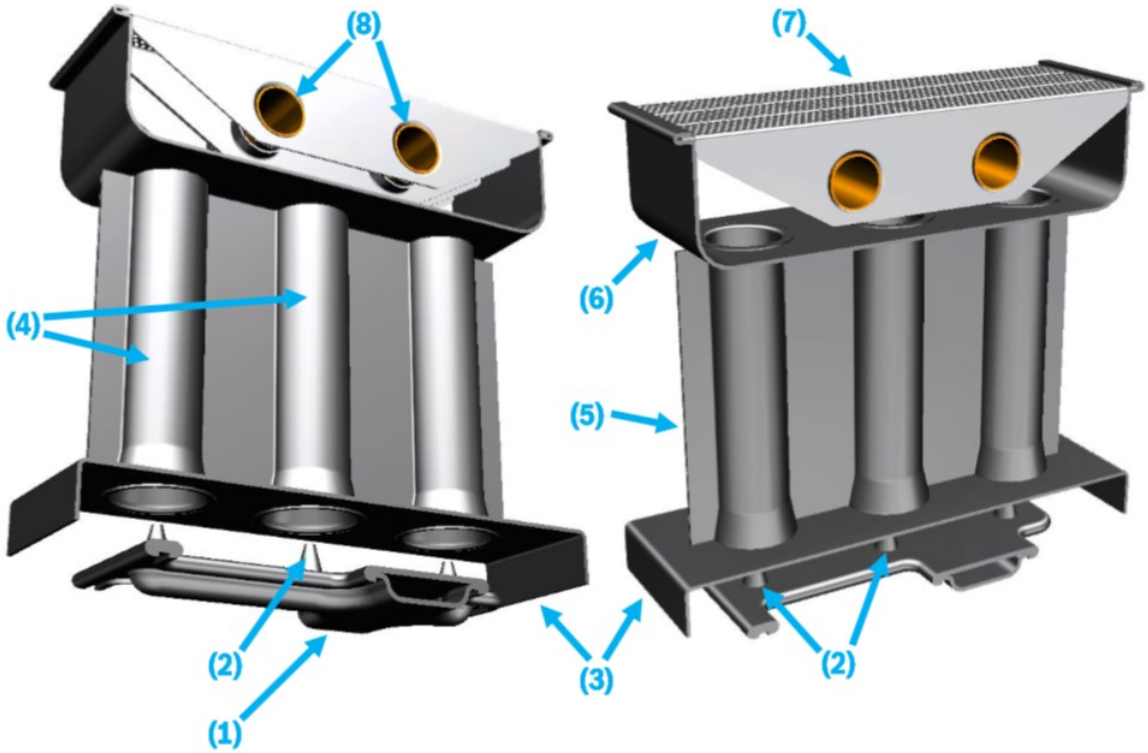

Figure A.2: Burner components: (1) gas manifold, where (2) the injectors are connected; (3) bottom plate; (4) mixing tubes, arranged in (5) blades of three; (6) plenum chamber; (7) burner surface blades with (8) the water-cooling circuit connected to it (extracted from [13]).

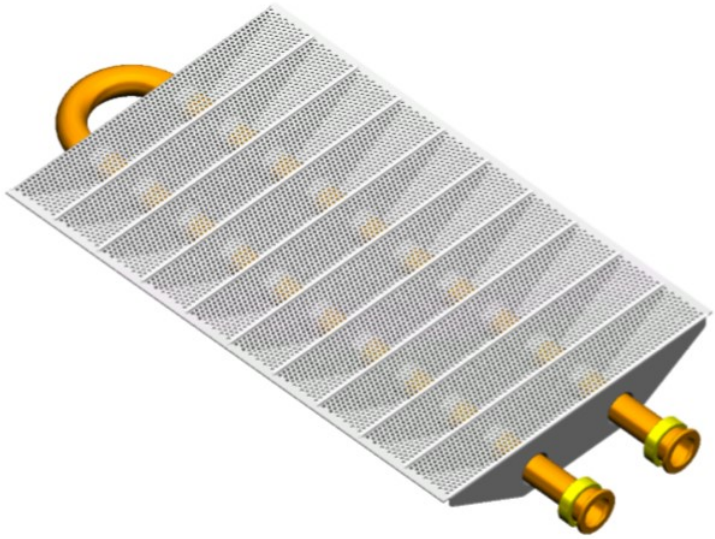

Figure A.3: Burner surface with the water cooling circuit (extracted from [13]).

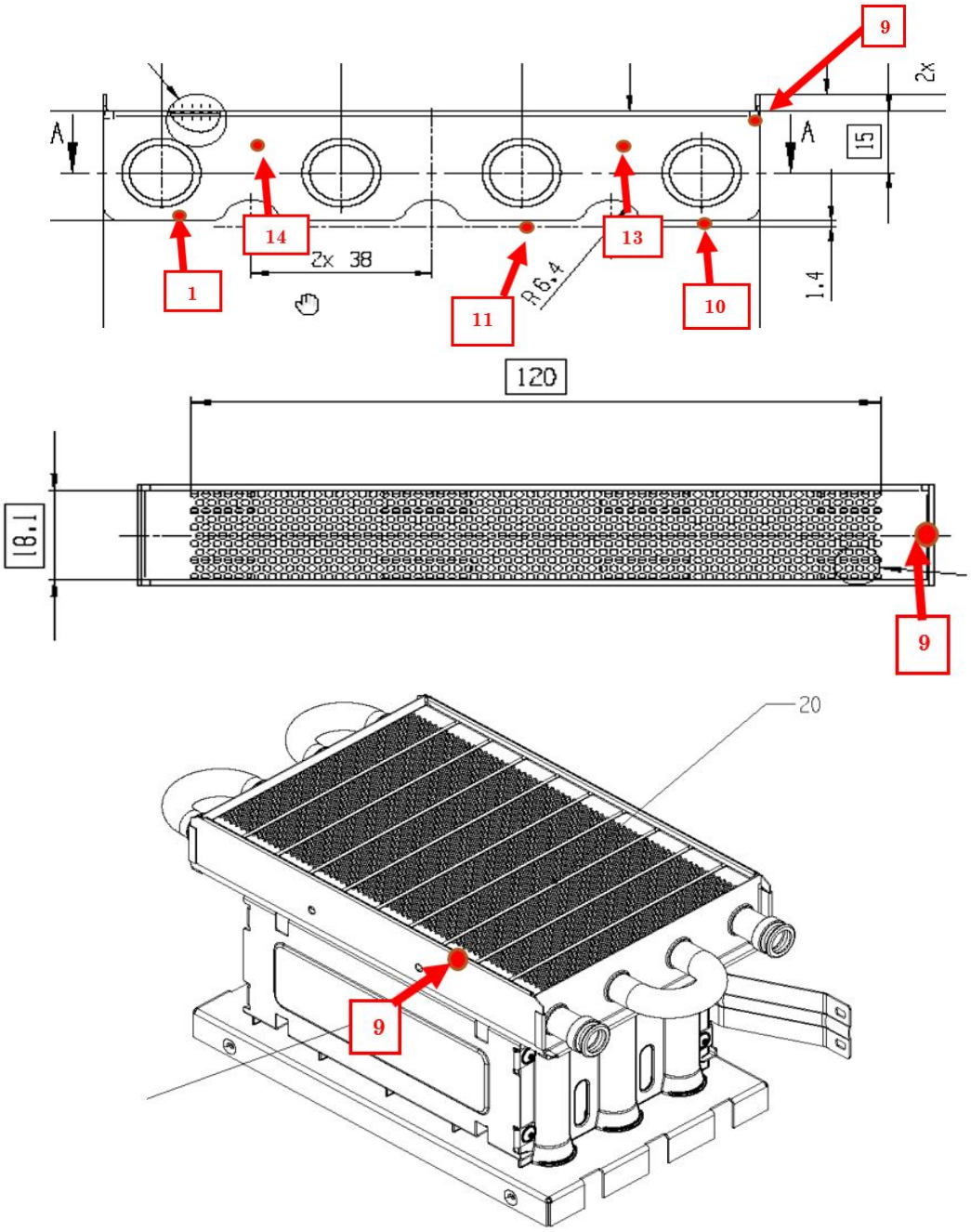

Figure A.4: Representation of the experimental temperature measurements points.